

## ABSTRACT

Title of dissertation: MAGNETIC REVERSAL OF  
ARTIFICIAL KAGOME ICE

Stephen Allen Daunheimer

Doctor of Philosophy, 2013

Advised by: Professor John Cumings  
Depart. of Materials Science & Engineering

Geometric frustration is a phenomenon where a crystalline material cannot satisfy all of its competing interactions, which can drastically change the behavior of a material. When water freezes into solid ice, the hydrogen atom positions are geometrically frustrated due to different interactions among neighboring oxygen atoms. Frustration is not limited to electrostatic interactions, though. Magnetic spin ice mimics the crystal structure and, therefore, the frustration of water ice. However, a problem with the spin ices is that the details of the magnetic state cannot be imaged which makes the dynamics difficult to probe.

In 2006, a model system known as “artificial” spin ice was created to alleviate these problems. The artificial spin ices are also geometrically frustrated, but they

are easier to fabricate, and the interactions in the system can be tailored to suit the experiment. They are made of lithographically defined arrays of interacting ferromagnetic elements, and the entire sample may be imaged to view the details of the magnetic state through a dynamic process.

The research presented here focuses on artificial spin ices with a honeycomb shape known as artificial kagome ice. Low disorder samples are created to study the dynamics of the magnetic reversal process to better understand the statistics and kinetics of the reversal process of frustrated materials. Results indicate reversals are defined by a complex avalanche process with a randomness that can be tuned by crystal geometry and reversal angle.

Magnetically reversing samples at field angles of  $180^\circ$ ,  $100^\circ$ , and  $120^\circ$  allows us to directly measure the disorder in our samples. Many  $180^\circ$  reversals were performed to allow us to measure the randomness of the reversals. Reversals at  $180^\circ$  are highly random, whereas at  $100^\circ$  and  $120^\circ$  they are much less so. There appears to be a change in the nature of the reversals at an angle of  $\theta \approx 130^\circ$  where avalanches start appearing in the reversals. As the angle is increased, large avalanches spanning the entire crystal start to dominate the reversal process.

The detailed image sequences of an artificial spin kagome ice sample allow us to simply model the behavior of the crystal as the motion of magnetic monopoles. Also, we make connections to the well-studied science of Barkhausen noise in magnetic materials noting that our samples exhibit the power law behavior typical of Barkhausen experiments.

# MAGNETIC REVERSAL OF ARTIFICIAL KAGOME ICE

by

Stephen Allen Daunheimer

Dissertation submitted to the Faculty of the Graduate School of the  
University of Maryland, College Park in partial fulfillment  
of the requirements for the degree of  
Doctor of Philosophy  
2013

Advisory Committee:

Professor John Cumings, Chair/Advisor

Professor Ichiro Takeuchi

Professor Lourdes Salamanca-Riba

Professor H. Dennis Drew, Dean's Representative

Dr. Julie Borchers

© Copyright by  
Stephen Allen Daunheimer  
2013

## Acknowledgements

The culmination of my graduate studies is a high point in a journey I have never been taking alone. Many people have helped me both professionally and personally throughout my life. First, I would like to thank my mother and father. Their love and support throughout the years shaped me into the person I am today, and without them I never would have made it to graduate school. I love you both.

I would also like to thank my advisor, Dr. John Cumings. His breadth of scientific knowledge, constant creative thinking, and incredible passion for research are a constant source of inspiration, and his support and confidence in me has been a source of encouragement. It has been a pleasure to work with him throughout my graduate studies. He is a great scientist, teacher, and mentor, and because of John, I have grown both professionally and personally.

While pursuing my studies at the University of Maryland, I have had the pleasure of working with numerous collaborators. Oleg Tchernyshyov, along with his students Paula Mellado and Olga Petrova developed a theoretical model of our artificial kagome ice samples that simply describes the samples. Their curiosity and knowledge has proved most helpful. Also, our neutron scattering experiments would not have been possible without the expertise of both Julie Borchers and Brian Maranville from NIST. I have enjoyed interacting with talented scientists from all over the world while working on my research.

I want to thank my fellow research group members past and present for their help and discussions. Todd Brintlinger, a postdoc in our group when I joined five years

ago, taught me everything about electron-beam lithography, and he was very helpful in teaching me the programming skills I would need throughout graduate school. Yi Qi helped acquaint me with the artificial spin ice project and was extremely helpful in getting me started. Kamal Baloch was always willing to provide whatever assistance I needed, and his work on the Hall sensor holder made my work possible. I look forward to future conversations about politics, both domestic and foreign. I had the pleasure of sharing an office with Kai He, our extremely capable postdoc. We became friends through our conversations and while traveling to conferences together. A new graduate student, Jasper Drisko, has started taking the artificial spin ice project in a new direction, and it has been exciting working with him and seeing his progress. Group members Khim Karki, Paris Alexander, Norvik Voskanian, John Bavier, Jeremy Ticey, and Hanna Nilsson all work on projects other than my own, but they have all enlightened me to new science, and working alongside them in our group has been an experience I treasure.

I would like to thank my friends that have proved to be crucial supports while I have been in graduate school. Aaron Lasher has been a friend of mine since elementary school, and our continued friendship is a pleasure whose importance I cannot overstate. You are the brother I never had. Elizabeth Lasher and I became friends while I was in graduate school, and her caring and genuine nature continues to inspire. Steven Souryal's humor and warmth made us quick friends. I look forward to embarking upon another chapter in both of our lives.

I would like to thank all of the professors at the University of Maryland and previous institutions I have attended. Notably, Marco Fornari, David Current, and

Robert Briber.

I would like to thank the technicians and laboratory staff in the FabLab and NISP Lab, especially Dr. Wen-An Chiou, Larry Lai, John Hummel and Tom Loughran. My reliance upon your work wasn't always noted, but it was absolutely critical to my experiments.

## Dedication

For my family and friends. Thank you.



# Table of Contents

List of Tables	vii
List of Figures	viii
1 Introduction	1
2 Geometric Frustration & the Ices	5
2.1 Geometric Frustration in Magnetic Materials . . . . .	5
2.2 Water Ice & a Residual Entropy . . . . .	8
2.3 Pyrochlore Spin Ice . . . . .	11
3 Artificial Kagome Ice	16
3.1 The case for artificial spin ice . . . . .	16
3.2 Artificial Kagome Ice . . . . .	23
3.3 Sample Fabrication . . . . .	26
3.4 Lorentz-Force Transmission Electron Microscopy . . . . .	30
3.5 <i>In situ</i> Application of External Magnetic Fields . . . . .	32
4 <i>In situ</i> Magnetic Reversal	43
4.1 Magnetic Monopoles in Spin Ice . . . . .	43
4.2 Testing the Monopole Model in Artificial Spin Ice . . . . .	45
4.3 Disorder in Artificial Kagome Ice . . . . .	53
4.4 Power-law Behavior of Chain Lengths During Reversal . . . . .	64
4.5 Removing the Avalanches From Reversals . . . . .	77
5 Investigations of Long-Range Order	80
5.1 Dipolar Interactions in Pyrochlore Spin Ice . . . . .	80
5.2 Off-specular Neutron Reflectometry . . . . .	82
6 Conclusions & Future Work	91
6.1 Conclusions . . . . .	91
6.2 Future Work . . . . .	94
A Computer & Microscope Control Programs	96
A.1 Schematics of LabView Programs . . . . .	98
B Lithography Techniques	101
B.1 Sample Patterning . . . . .	101
B.2 Metal Deposition . . . . .	103
Bibliography	107

## List of Tables

4.1	<b>Calculated static and stochastic disorder parameters . . . . .</b>	57
4.2	<b>Experimentally measured disorder parameters . . . . .</b>	63
4.3	<b>Power law fit parameters . . . . .</b>	72

## List of Figures

2.1 Frustration on a triangular lattice . . . . .	6
2.2 Two-dimensional geometrically frustrated lattices . . . . .	7
2.3 Three dimensional frustrated lattices . . . . .	9
2.4 Tetrahedral crystal structure of water . . . . .	11
2.5 Tetragonal crystal structure of pyrochlore spin ice . . . . .	12
2.6 Residual entropy of pyrochlore spin ice . . . . .	13
3.1 Shape anisotropy in magnetic elements . . . . .	16
3.2 Frustration by limiting degrees of freedom . . . . .	17
3.3 Artificial square ice . . . . .	18
3.4 Square ice vertex configurations . . . . .	19
3.5 Artificial square ice statistics . . . . .	21
3.6 Artificial kagome ice . . . . .	24
3.7 Spin-spin correlations in the kagome lattice . . . . .	26
3.8 Rigid ice rules in artificial kagome ice . . . . .	27
3.9 Artificial kagome crystal geometries . . . . .	28
3.10 Ferromagnetic resonance data of an artificial kagome ice sample	30
3.11 Lorentz TEM beam shift . . . . .	31
3.12 Objective lens as a magnetic field source . . . . .	34
3.13 Double-tilt TEM holder . . . . .	36
3.14 Getting an in-plane field component . . . . .	37
3.15 Measuring the direction of the magnetic field . . . . .	38
3.16 Armchair edge reversal images . . . . .	40
3.17 Zigzag edge reversal images . . . . .	41
3.18 Magnetization data from an image sequence . . . . .	42
4.1 Magnetic monopoles in pyrochlore spin ice . . . . .	44
4.2 Evidence of monopoles in artificial kagome ice . . . . .	46
4.3 Dumbbell model in artificial kagome ice . . . . .	48
4.4 Kagome element reversal through monopole motion . . . . .	49
4.5 Initiating a reversal on even edge crystals . . . . .	51
4.6 Testing for metastable ice-rule violations . . . . .	52
4.7 Measuring static disorder . . . . .	55
4.8 Measuring stochastic disorder . . . . .	56
4.9 Zoomed in avalanche at 180° . . . . .	58
4.10 Experimental data compared to theoretical predictions from monopole model . . . . .	61
4.11 Barkhausen experiment and the resulting power law behavior	65
4.12 M(H) plot showing the Barkhausen effect . . . . .	66
4.13 Experimental M(H) plot showing large jumps in M . . . . .	67
4.14 Stochastic reversal through avalanches . . . . .	70
4.15 Power law behavior of the reversal avalanches . . . . .	71
4.16 Bounding area of reversal chains . . . . .	74

4.17	Fractal dimension of kagome avalanches . . . . .	76
4.18	Odd edge crystal reversals . . . . .	78
5.1	Dipolar interactions in pyrochlore spin ices. . . . .	81
5.2	Schematic of off-specular reflectometry geometry . . . . .	82
5.3	Fast Fourier transforms of artificial kagome ice . . . . .	84
5.4	Neutron scattering sample . . . . .	85
5.5	Simulated neutron scattering intensity . . . . .	86
5.6	Experimental and theoretical data . . . . .	87
A.1	Global Degauss (GlobalDegauss.vi) . . . . .	98
A.2	Local Degauss (LocalDegauss.vi) . . . . .	98
A.3	Set Field (SetField.vi) . . . . .	98
A.4	Angle Interpolation (AngleInterp.vi) . . . . .	99
A.5	Set Goniometer Angles (SetGonioAngles.vi) . . . . .	99
A.6	Execute Digital Micrograph Script (ExecuteGatanScript.vi) . . . . .	99
A.7	Open Digital Micrograph network connection (StartDM.vi) . . . . .	100
A.8	Close Digital Micrograph network connection (ExitDM.vi) . . . . .	100
A.9	Open JEOL network connection (StartJEOL.vi) . . . . .	100
A.10	Close JEOL network connection (ExitJEOL.vi) . . . . .	100
B.1	Bare silicon nitride TEM window . . . . .	102
B.2	Metal lift-off failure . . . . .	105
B.3	Sample fabrication process . . . . .	106

# Chapter 1

## Introduction

In 1933, it was realized that water exhibits an interesting property: upon freezing the oxygen atoms create a crystal structure, but the hydrogen atoms do not [1–3]. Instead, they remain mobile down to approximately 70 Kelvin where they freeze without ordering, giving rise to the “residual entropy” of water. A non-zero entropy at zero Kelvin would seem to violate the third law of thermodynamics, and was one reason for the initial interest in studying water and other so-called “frustrated” materials.

In the field of magnetism, the pyrochlore ( $\text{Ho}_2\text{Ti}_2\text{O}_7$  and  $\text{Dy}_2\text{Ti}_2\text{O}_7$ ) compounds are among the most well-known frustrated materials. The pyrochlore crystal structure limits the degrees of freedom of the rare-earth magnetic spins surrounding the transition metal atoms in the crystal structure. The spins are forced to either point into or out of the tetrahedra where the rare earth ions reside, and the lowest energy state is when two are pointing in and two are pointing out. This is similar to the frustration in water ice discovered by Bernal and Fowler, and thus the two-in, two-out “ice rules” are remain same [2], and the form of the residual entropy is also unchanged [3].

Artificial spin ice was developed in 2006 as an easier to fabricate analogue to the bulk spin ice materials [4]. They are condensed matter meta-materials that

can be fabricated using standard nano-lithography techniques, and their dimensions, symmetry, and composition can be readily altered to tune the interactions in the system. Artificial spin ice also provides a system to study geometric frustration on small scales without relying upon complicated trial-and-error crystal growth to create single crystal pyrochlore samples. The dimensions of the individual magnetic elements require them to be single magnetic domains. Furthermore, the small dimensions impose a strong shape anisotropy, and this has the effect of forcing the magnetic spins of the individual elements to point along the elements longitudinal axis so that they can be considered two-state Ising spins [4, 5].

My research focuses on the effect of the geometric frustration on the dynamics of artificial kagome ice. The bulk of the results are from *in situ* magnetic reversals imaged in a transmission electron microscope (TEM) which are discussed in Chap. 4. Using custom programs and electronics designed to interface with the JEOL 2100 LaB6 transmission electron microscope, an external magnetic field can be applied in-plane at any desired angle. By gradually stepping the magnitude of the magnetic field, a complete, high resolution magnetic reversal can be completed of an entire artificial spin ice sample. This process is discussed in Sec. 3.5.

Lorentz-force microscopy is used to characterize the samples and observe them through the magnetic reversal process. This technique provides detailed spin maps of each element throughout the reversal which can be analyzed to provide details of the system throughout the reversal. We will show that our samples are very uniform with significantly less disorder when compared to artificial spin ices made by others [6]. Not only does this make these artificial spin ices some of the best

yet fabricated, it also allows us to see behaviors not seen by others. Of particular interest are the long, highly-branched chains of elements that reverse as an ensemble throughout the reversal process. These avalanches appear similar to self-organized critical behavior in other materials ranging from earthquakes to neurons in our brains. Through analysis our of avalanches, we will show that the avalanche events we see do, indeed, exhibit both the power law behavior typical of critical phenomenon, and have a fractal dimension between 1.0 and 2.0.

Branched chains of this length would not be expected unless the geometry of the system induces the chains to continue throughout the length of the sample. Ideas such as an inertia associated with the mobile domain walls have been offered as a potential explanation. These suggestions are the result a monopole model discussed in Sec. 4.1, and we show the validity of such a model by testing the model's predictions in Sec. 4.2.

Using a custom LabView program that automates the reversal process, many reversals have been collected and can be compared to one another. This large sample size (over 300 million element counts for reversals at  $\theta = 180^\circ$ ) allows us to perform our analysis on statistically relevant data sets. Evidence of a power law can already be seen when plotting chain counts of a given length.

Lastly, in Chap. 5, I will discuss some initial neutron scattering studies performed on my artificial kagome ice samples to search for evidence of dipolar interactions among the elements. This basic, magnetic interaction should be present, and its presence is suggested by the dipolar energies calculated on similar artificial kagome ices [5] as well as the demonstration of the dipolar interaction in the pyrochlore spin

ice compounds [7].

My research helps us understand what happens when the dimensions of a magnetic material are drastically altered from bulk, and a better understanding of how the magnetic properties of materials can be engineered and controlled may prove fruitful for a number of fields of study in the future. Patterned films have already been proposed as a replacement for the magnetic hard disks prevalent in computers [8]. Additionally, researchers such as Cowburn, *et al.* have been studying the potential for magnetic logic (or “spintronic”) devices fabricated from a series of interacting magnetic nanowires [9]. These devices represent information in the direction of the magnetization of a ferromagnetic element, and they remove the low-temperature requirement of similar devices based upon semiconductor materials. These devices are likely to be the basis of magnetic random-access-memory (MRAM) devices in the near future. They promise to be nonvolatile, high-density, and high-speed devices for storing information.



## Chapter 2

### Geometric Frustration & the Ices

#### 2.1 Geometric Frustration in Magnetic Materials

Geometric frustration occurs when there is a conflict between the preferred interactions of a system and the degrees of freedom available to it. The restrictions will prevent the system from ordering and thus satisfying all of the competing interactions in the system. Typically, geometric frustration results from the lattice geometry preventing the system from settling into a single, ordered, low-energy state. The system remains trapped in a higher entropy state, unable to further relax, and this also usually leads to multiple, degenerate ground states. This is unlike something like NaCl which has a perfect, cubic crystal structure, and the sodium and chlorine ions will always freeze into the same crystal structure.

Geometric frustration in magnetic materials was first demonstrated in a fairly complex system known as “spin glasses”: materials with magnetic impurities embedded in non-magnetic host materials [10]. These alloys are structurally ordered in that their atoms have an ordered crystal structure, but ferromagnetic or anti-ferromagnetic interactions in the system are not able to align the spins into their preferred configuration because of the geometry of the lattice. At temperatures above some critical temperature, the magnetic behavior will be typical of a non-magnetic material with an uncoordinated arrangement of the magnetic spins leading to zero net magnetic

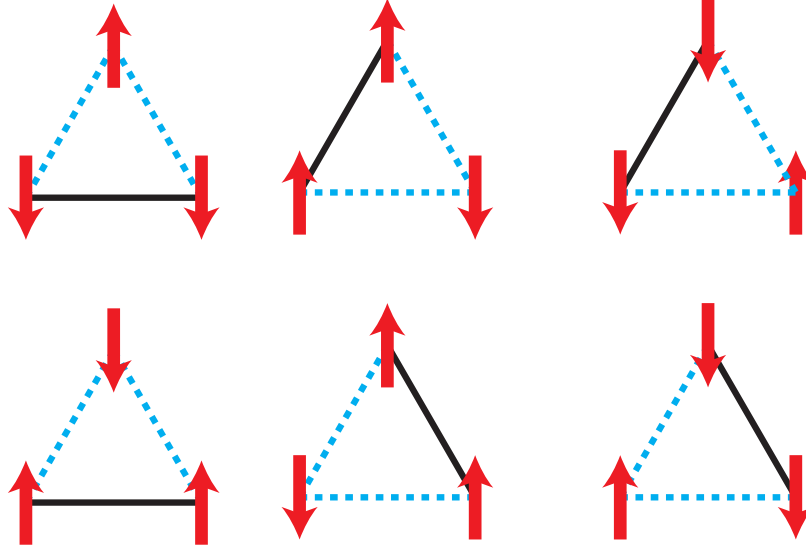


Figure 2.1: **Frustration on a triangular lattice** Possible lowest-energy configurations for three anti-ferromagnetic spin on a triangular lattice. Regardless of the configurations the spin take, there are always two anti-ferromagnetic (blue dotted) and one ferromagnetic (solid black) arrangements. These 6 states are equivalent in energy and the lowest energy states available to these three spin.

moment. This spin arrangement is not permanent; if an external field is applied and the system is allowed to cool, the magnetization will quickly approach a remanent state with a net positive magnetization. In essence, the spins have overcome their geometric constraints to align themselves in a more favorable, low-energy state. This state is only metastable though, and there is a period of slow decay of the magnetization resulting from the disorder in the system. This structural disorder forces the system into a higher entropy state, and it takes an appreciable amount of time to relax back to its initial state. Toulouse named the occurrence of limited degrees of freedom as a result of crystal structure “geometrical frustration” [10].

A simple, theoretical demonstration of this phenomenon is the case of three spins aligned on a triangular lattice with anti-ferromagnetic interactions as seen in Fig. 2.1. The system cannot align the magnetic moments to satisfy all three anti-ferromagnetic

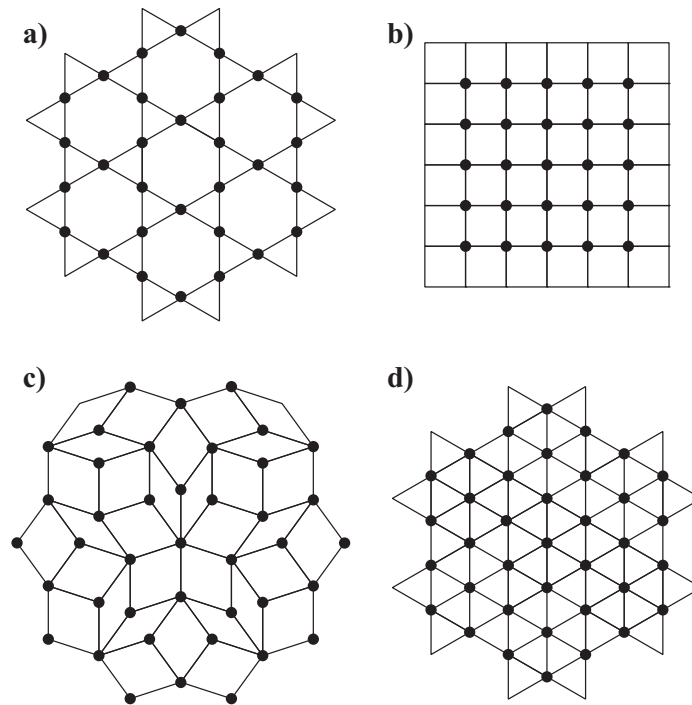


Figure 2.2: **Two-dimensional geometrically frustrated lattices** The (a) kagome lattice, (b) square, (c) penrose, and (d) triangular lattice are all examples of geometrically frustrated crystal structures in two dimensions. Filled dots are included at the vertices. In addition, the kagome and triangular lattices are crystal planes in a larger, three-dimensional frustrated crystal structure.

interactions. Furthermore, there are six possible configurations that exist with one ferromagnetic alignment and two anti-ferromagnetic alignments; the lowest energy state is 6-fold degenerate. There are, of course, more complicated lattices that result in geometric frustration of magnetic spins, and schematics of their geometries are shown in Fig. 2.2. The square and kagome lattices are the most important for this work. However, other researchers have looked into more complicated symmetries [11]. There are also other crystal lattices that result in geometrically frustrated magnetic moments. Again, the crystal structure prevents the moments from relaxing (typically due to a large crystalline anisotropy forcing the spins along specific crystal axes). In the case of geometrically frustrated magnetic materials, the positions of the atoms' magnetic moments cannot rearrange themselves into a ferromagnetic (all spins aligned parallel) or anti-ferromagnetic (all spins aligned anti-parallel) state.

More complicated, three-dimensional structures are shown in Fig. 2.3. These structures are examples of real, bulk geometrically frustrated materials [12–14].

## 2.2 Water Ice & a Residual Entropy

Since the phenomenon of geometrical frustration was laid out by Toulouse *et al.*, it has been a subject of intense interest. The behavior is seen in common, everyday materials and not limited to more esoteric materials like spin glasses. The most well-known geometrically frustrated system is simple water ice, and the frustration in the system is responsible for water's most interesting properties: solid water is less dense than liquid water, and therefore, solid water floats on top of liquid water.

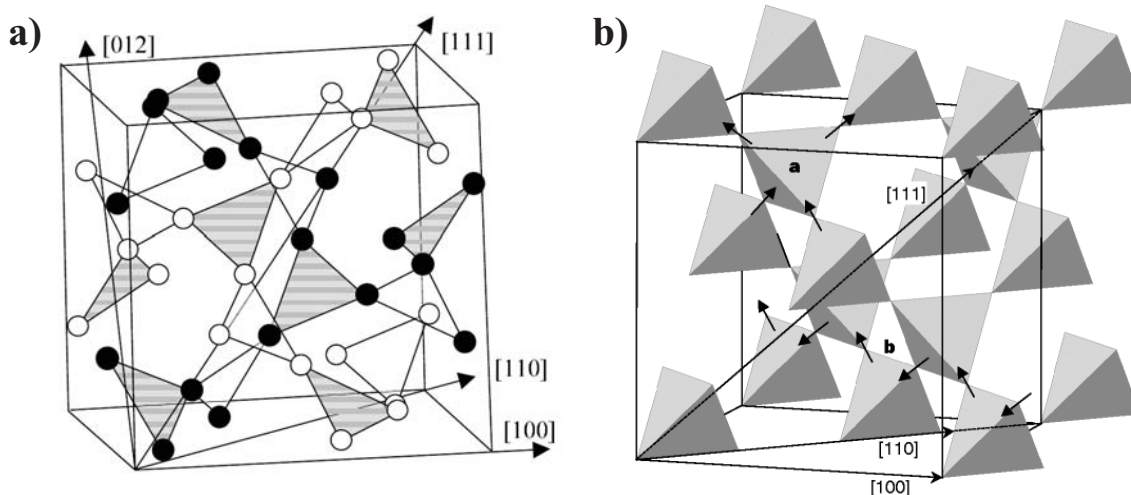


Figure 2.3: **Three dimensional frustrated lattices** Examples of two different bulk frustrated lattices. (a) The garnet lattice [14] and (b) the pyrochlore lattice [12]. Both have geometrically frustrated magnetic spins.

This phenomenon can be explained entirely as a result of the crystal structure of solid water. Water ice is made of  $\text{H}_2\text{O}$  molecules, and upon freezing, each oxygen atom is at the center of a tetrahedron with four hydrogen atoms at the corners as can be seen in Fig. 2.4. Importantly, the O-H distance is not the same among all four hydrogen atoms forming the tetrahedra. Two of the hydrogen atoms are covalently bonded to each oxygen (forming one of many  $\text{H}_2\text{O}$  molecules), and the other two are hydrogen bonded (from separate  $\text{H}_2\text{O}$  molecules); the lengths of these bonds are  $0.95 \text{ \AA}$  and  $1.81 \text{ \AA}$  respectively [2]. This leads to what are known as the Bernal-Fowler, or “two-in, two-out” ice rules: each oxygen has two hydrogen atoms are close to it (covalent bonds) and two are farther away from it (hydrogen bond) [2]. Bernal *et al.* explained that because there are many ways for a group of  $\text{H}_2\text{O}$  molecules to form a structure that obeys these ice rules, water ice must have a degenerate ground state. In apparent contrast to the third law of thermodynamics, it was theorized that the

hydrogen atoms in water ice remain disordered down to zero Kelvin, and therefore there was no unique ground state for water ice; the entropy would not go to zero.

In 1935, theoretical calculations by Linus Pauling were able to give an initial estimation of this residual entropy by counting the number of possible ground states of ice [3]. There are  $N$   $\text{H}_2\text{O}$  molecules in one mole of ice, and there are  $2N$  possible states placing a hydrogen “in” or “out” in relation to the neighboring oxygen atoms, and therefore, there are  $2^{2N}$  possible configurations for the hydrogen atoms. Next, for each oxygen atom, there are 4 hydrogen atoms surrounding it creating  $2^4 = 16$  possible states for each tetrahedron. However, only 6 of those configurations obey the ice rules. Ultimately, the number of configurations for one mole of water ice is

$$\Omega_0 = \left[ 2^2 \left( \frac{6}{16} \right) \right]^N = \left( \frac{3}{2} \right)^N \quad (2.1)$$

which results in a residual entropy of

$$S_0 = k \ln \Omega_0 = R \ln \left( \frac{3}{2} \right) \quad (2.2)$$

per mole, where  $R = Nk = 1.987 \text{ cal} \cdot \text{mol}^{-1} \cdot \text{K}^{-1}$  is the gas constant [3]. Or, alternatively,

$$S_0 = 0.805 \text{ cal} \cdot \text{mol}^{-1} \cdot \text{K}^{-1} \quad (2.3)$$

Pauling’s calculations attempt to explain earlier heat capacity measurements performed on water by Giauque *et al.* [1,15]. Via careful calorimetry measurements, they found that water has a non-zero entropy at zero Kelvin. They did not have a solid understanding for this, but the measured residual entropy of water ice was found to be  $0.82 \text{ cal mol}^{-1} \text{ K}^{-1}$ . This agrees well with Pauling’s value of  $0.805 \text{ cal}$

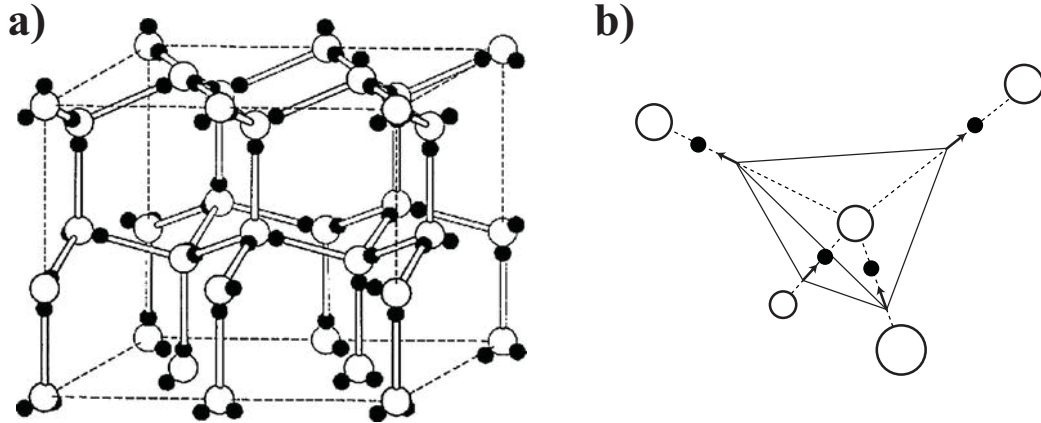


Figure 2.4: **Tetrahedral crystal structure of water** (a) The crystal structure of water. Oxygen atoms (white circles) are in a hexagonal structure while the hydrogen atoms (black circles) remain in a disordered configuration. (b) One tetrahedron in the water ice crystal structure. Oxygen atoms are surrounded by four hydrogen atoms [13].

$\text{mol}^{-1} \text{K}^{-1}$ , and it confirmed that the disorder in the crystal structure of hydrogen atoms was a simple explanation of the source of water’s residual entropy. Later, a more rigorous calculation was performed resulting in a residual entropy of  $S = 0.8145 \text{cal} \cdot \text{mol}^{-1} \cdot \text{K}^{-1}$  [16] in even better agreement with the results of Giauque *et al.*

### 2.3 Pyrochlore Spin Ice

Another class of geometrically frustrated materials was discovered in the pyrochlore spin ice compounds. Pyrochlore is a generic term for materials of the form  $\text{A}_2\text{B}_2\text{O}_6$  and  $\text{A}_2\text{B}_2\text{O}_7$ . In the magnetic pyrochlore compounds, “A” is typically a magnetic rare earth metal, and “B” is a transition metal.  $\text{Ho}_2\text{Ti}_2\text{O}_7$  was the first pyrochlore shown to have geometrically frustrated magnetic interactions. The magnetic, A-site atoms create a tetrahedron around the transition metal B-site atoms; the lattice structure

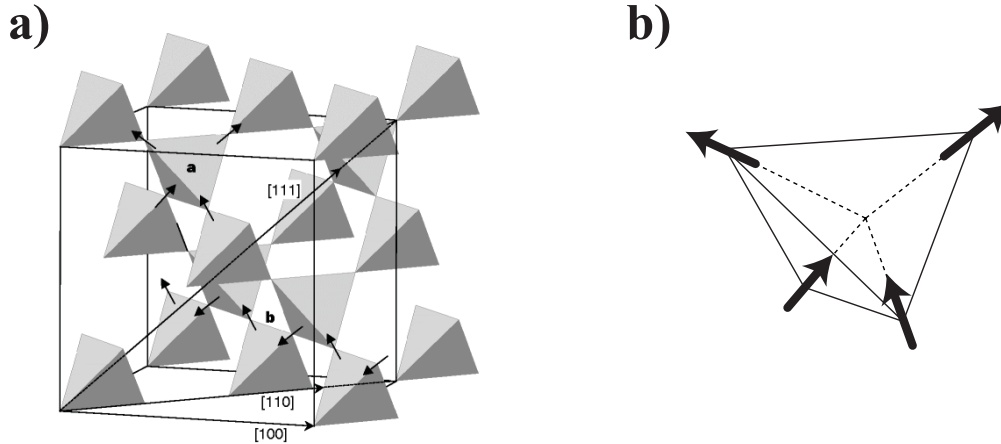


Figure 2.5: **Tetragonal crystal structure of pyrochlore spin ice** (a) The crystal structure of the pyrochlore spin ice compounds shares the same symmetry of water ice [12]. (b) The difference is that here the magnetic spins of rare earth elements define the corners of the tetrahedra instead of hydrogen atoms [13].

can be seen in Fig. 2.4. The rare earth ions have very large magnetic moments of  $10\mu_B$ , and they must point either toward or away from the center of the tetrahedron. In this way, the magnetic moments (spins) of the rare earth metals are frustrated in the same manner as the proton displacement in water ice [17, 18]. The ferromagnetic spins are forced into a higher energy state where two magnetic spins point into the tetrahedron, and two point out. Again, there are 6/16 possible ways for the “two-in, two-out” geometry to be realized, and this results in degenerate ground states and a residual entropy maps onto that calculated for water ice [3, 16].

Originally, it was thought that  $\text{Ho}_2\text{Ti}_2\text{O}_7$  was a geometrically frustrated anti-ferromagnet, but subsequent muon spin-relaxation ( $\mu\text{SR}$ ) combined with other magnetization experiments actually showed ferromagnetic interactions instead [13, 17, 19]. Further testing was performed on other pyrochlore spin ices. It was found that  $\text{Dy}_2\text{Ti}_2\text{O}_7$  was another frustrated pyrochlore, but others, such as  $\text{Yb}_2\text{Ti}_2\text{O}_7$  were



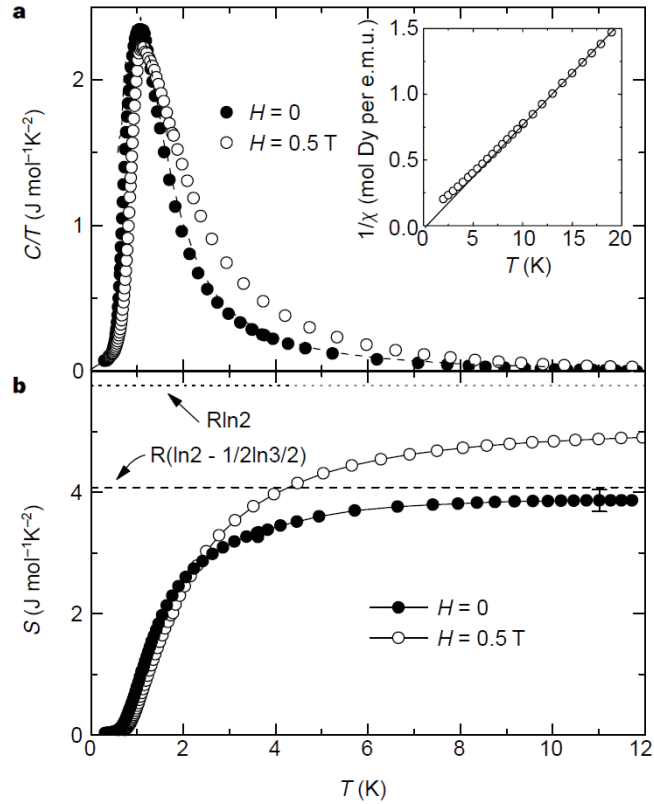


Figure 2.6: **Residual entropy of pyrochlore spin ice** A plot of (a) specific heat divided by temperature,  $C(T)/T$ , and (b) entropy,  $S$ , of  $\text{Dy}_2\text{Ti}_2\text{O}_7$  at  $H = 0\text{T}$  and  $0.5\text{T}$  showing the non-zero entropy at zero Kelvin [12]. The  $H = 0.5\text{T}$  state creates a more ordered state, and recovers some of the missing entropy of the  $H = 0\text{T}$  state. The entropy curve is found by integrating  $C(T)/T$  from 0.2 to 14 K. The measurements agree with the calculations of Pauling [3] for water ice.

not. Magnetic specific heat measurements of  $\text{Dy}_2\text{Ti}_2\text{O}_7$  showed the validity of using the Pauling ice model in the pyrochlores as a model for geometric frustration [12]. Ramirez *et al.* measured the magnetic specific heat and integrated it from  $T_1 = 300\text{mK}$  to  $T_2 = 10\text{K}$  where the system has passes through a paramagnetic transition. Ramirez *et al.* then integrated this measured magnetic heat capacity over the experimental temperature range. By comparing the difference between their measurement, and the expected entropy value for a simple, two-state system ( $S_0 = R \ln 2$ ), they were able to measure the residual entropy which is not recovered when the system is cooled down. As expected from the geometrical considerations results showed a zero-point entropy similar to that for water ice [12] as

$$\Delta S = \int_{T_1}^{T_2} \frac{C(T)}{T} dT = 1.68 \text{ J} \cdot \text{mol}^{-1} \cdot \text{K}^{-1} \quad (2.4)$$

The residual entropy can be counted in a similar way as that used for water ice. Counting using the number of spins,  $N$ , which gives  $N/2$  tetrahedra (as Ramirez *et al.* did) we get

$$\Omega_0 = \left[ 2^2 \left( \frac{6}{16} \right) \right]^{N/2} = \left( \frac{3}{2} \right)^{N/2} \quad (2.5)$$

Their result for the residual entropy in  $\text{Dy}_2\text{Ti}_2\text{O}_7$  was

$$S_0 = k \ln(\Omega_0) = \left( \frac{R}{2} \right) \ln \left( \frac{3}{2} \right) \quad (2.6)$$

where the additional factor of  $1/2$  here is a result of mapping the geometry from water ice to spin ice where  $N$   $\text{H}_2\text{O}$  molecules leads to  $2N$  spins.

The pyrochlores have proven their usefulness in the field of magnetics, but there are a few problems with using them experimentally. Pyrochlore spin ices are

difficult to synthesize. Typically, a single crystal is needed to search for spin-spin correlations, and defects appear over time. Also, their crystal structure cannot be altered by changing the geometry or lattice constant. Most importantly, however, is that the details of the microscopic configuration cannot be probed. The details of a reversal process, for instance, are not possible with neutron scattering on pyrochlore spin ice materials. The physics relating to spin-spin correlations, heat capacity, and the pyrochlore's geometry on these parameters has largely been reported. What is needed now is a system that captures the physics of the spin ices, but that also allows for tailoring the magnetic interactions to their desired experiment. A newer class of magnetic materials known "artificial" spin ice was proposed for this purpose [4].

## Chapter 3

### Artificial Kagome Ice

#### 3.1 The case for artificial spin ice

Nano-patterned films have been studied for a number of years because they have been suggested as candidates for data storage technologies [20, 21] and magnetoresistive random access memory (MRAM) [22], and because they can be successfully fabricated to investigate the microscopic details of magnetism as materials are continually sized down.

Artificial spin ice was developed in 2006 [4] as an-easier-to fabricate analogue to the bulk spin ice materials. Patterned using electron-beam lithography, all artificial spin ices are patterned thin films with an imposed geometry that introduces magnetic frustration similar to their 3D counterparts. The materials are arrays of nanosized

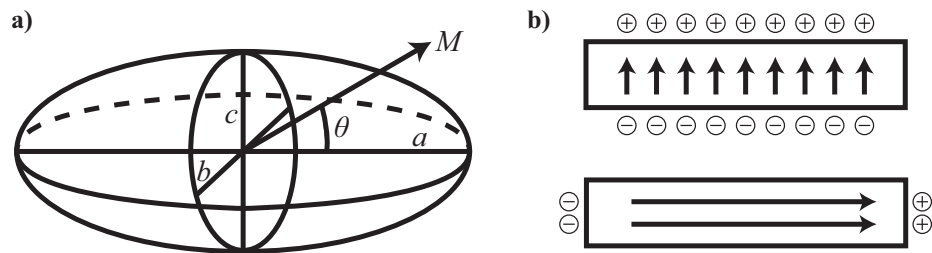


Figure 3.1: **Shape anisotropy in magnetic elements** (a) By considering an ellipsoid and using the kagome element dimensions as the ellipsoid's axes lengths, it is possible to calculate demagnetization factors along the different axes of a magnetic element [23]. (b) The magnetization direction within the element which creates the fewest monopoles along the edge is the direction that will be preferred for the internal magnetization.

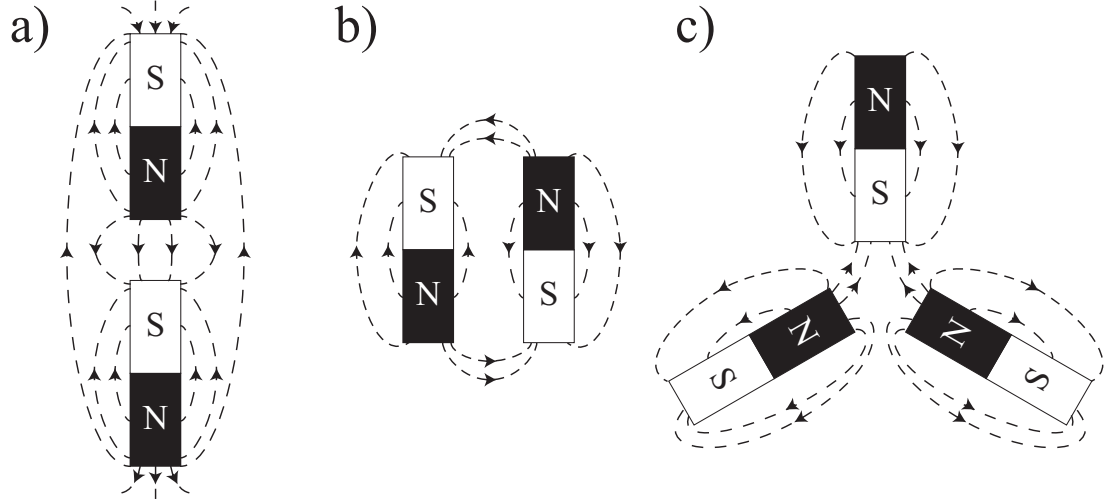


Figure 3.2: **Frustration by limiting degrees of freedom** Simple bars magnets can be arranged to have ferromagnetic (a) and anti-ferromagnetic (b) interactions. If three such bar magnets are placed in the orientation shown in (c) and not allowed to rearrange themselves, a combination of ferromagnetic and anti-ferromagnetic interactions occur. The magnets would like to rearrange themselves but are prohibited from doing so.

ferromagnetic islands of (typically)  $\text{Ni}_{80}\text{Fe}_{20}$ . The dimensions of the elements are fabricated to be smaller than the size of an average  $\text{Ni}_{80}\text{Fe}_{20}$  domain, which ensure that each element is comprised of a single magnetic domain. Furthermore, the aspect ratio of each magnetic element imposes an anisotropy to the internal magnetization of the each element. This can be understood by considering a related, but simpler geometry of an ellipsoid with axes,  $a$ ,  $b$ , and  $c$  as shown in Fig. 3.1.

The prolate spheroid show is similar in shape to the nanowires used in an artificial kagome ice sample, and allow for easy computation of the relative demagnetizing factors along each axis. If we use the dimensions of a typical artificial kagome ice element, then  $a = 500$  nm,  $b = 100$  nm, and  $c = 23$  nm. Calculating the demagnetization factors gives  $N_a = 0.02$ ,  $N_b = 0.18$ , and  $N_c = 0.80$ . The three values add to unity, and the larger the value, the harder it is for the internal magnetization of the

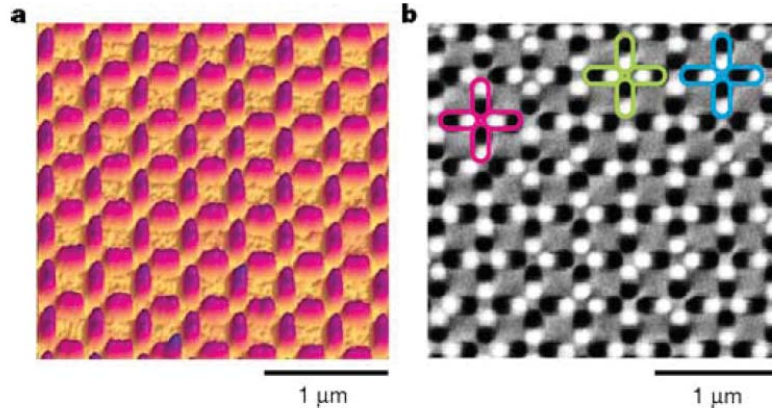


Figure 3.3: **Artificial square ice** (a) atomic force microscopy (AFM) and (b) magnetic force microscopy (MFM) images of an artificial square ice [4]. Elements are disconnected to allow MFM imaging. See [25].

element to point along that semi-axis. Here, it is much easier for the magnetization to point along the  $a$  axis [24].

This calculation illustrates that pointing along the long axis lowers the magnetostatic energy of the element, and this has the effect of forcing the magnetic spins of individual elements to point along the element's longitudinal axis. In this way they can be considered as Ising spins just like those in the spin ice compounds. The dimensions, symmetry, and material can also be altered if so desired to changed the geometry and interactions in the lattice. The first realization of artificial spin ice was made with a square lattice geometry as seen in Fig. 3.3 [4]. This is a more obvious mapping of the of the pyrochlore geometry because the two-in, two-out ice rules remain unchanged as a result of the four-fold symmetry. This also means that the residual entropy calculations are the same as for pyrochlore spin ice as the number of states per vertex is the same. The dimensions of the elements in the array were length  $l = 200$  nm, width  $w = 110$  nm, and thickness  $t = 23$  nm.

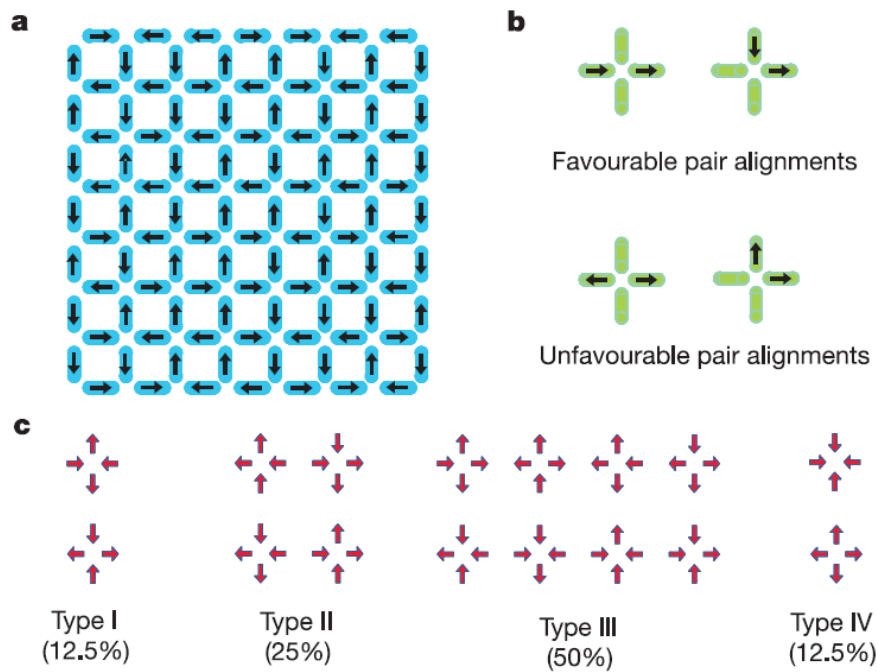


Figure 3.4: **Square ice vertex configurations** A schematic (a) of the square ice geometry. (b) Favorable configurations that lead to ice rule obeying states are shown, but it is important to note that in (c) the library of vertex configurations there are different energies because of the different interaction lengths among the elements at each vertex. See [4].

The crucial difference with artificial spin ices is that instead of dealing with identical magnetic spins, the frustration is now made of macroscopic magnetic dipoles. The elements are very small bar magnets made of a magnetic material (usually  $\text{Ni}_{80}\text{Fe}_{20}$ ). The spin flips in a pyrochlore spin ice compound are thermal in nature, as discussed before. The relationship governing the thermal barrier to spontaneous spin reversal is

$$\Delta E = K_u V \tag{3.1}$$

where  $K_u$  is a term describing magnetic anisotropy of an element, and  $V$  is the volume of a magnetic element. Artificial spin ice elements are comparatively huge when compared to atomic spins, so the energy barrier for spontaneous flipping in artificial spin ices is millions of Kelvin [4]. The spin state is frozen into the crystal at room temperature where all previous experiments have been performed.

To get around this complication and add magnetic dynamics into the system, Wang *et al.* rotated their artificial square ice samples while inside of an external magnetic field [25]. The field strength is gradually reduced and the sample is demagnetized through this process. If successful, the sample has zero net magnetic moment, and the spins are randomly oriented while still obeying their two-in, two-out ice rules. The field is started well above the coercivity of the crystal and ends well below the coercive field. In this way the crystal is able to sample a large number of its available ground states and accommodate the frustration at the vertices.

After demagnetizing samples with different separation lengths the vertices were examined to see if any violated the ice rule. What was found was that the square ice



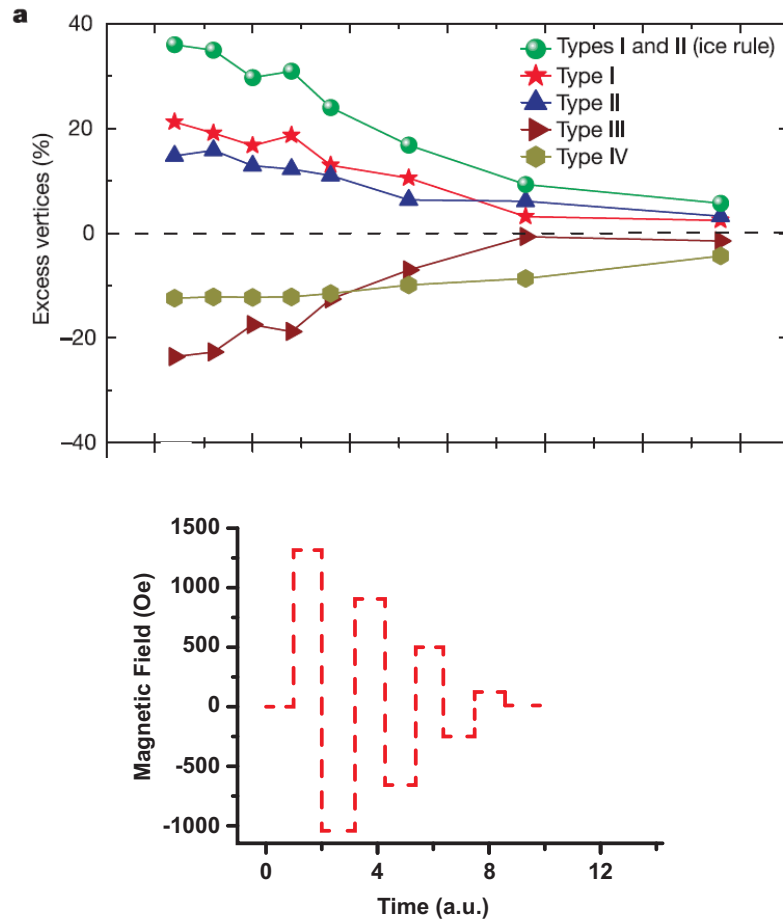


Figure 3.5: **Artificial square ice statistics** After an AC demagnetization of artificial square ice, the samples were found to only statistically obey the ice rule. Even with small separation (and therefore high interaction) there are a significant number of ice rule violations and higher energy vertices. The lower panel is an example plot of the field magnitude and direction as a function of time. Both panels from [4].

samples only “statistically” obey the ice rule even with the smallest element spacing to have strongly interacting elements [4]. A plot of this can be seen in Fig. 3.5b. This is because of the difference in interaction lengths at the vertices. Nearest neighbors are perpendicular to a given element, and next-nearest neighbors are colinear and across an vertex. This is different than the case of the atomic spin in the pyrochlore where the 3D structure allows all four elements to be the same distance from each other. This effect is seen from the high number of type III vertices (“three-in, one-out” or “one-in, three-out”) that are still present after a demagnetization run; type IV (“four-in” or “four-out”) vertices are also present.

So, an AC demagnetization protocol is not entirely successful in artificial square ice, but Morgan *et al.* looked at a different method of approaching the ground state, and it is largely due to how the samples are fabricated [26]. Wang *et al.* create their samples by depositing a magnetic film across the entire substrate. Then, a PMMA resist is spun onto the deposited film. This resist is then patterned using electron-beam lithography (EBL) and etched to create the desired geometry. Instead of this, Morgan *et al.* used a more common method of EBL (our group was also using this method, albeit on a different geometry). They deposit the PMMA film first and then pattern the resist atop the substrate. Then, the magnetic material is deposited onto the patterned film. Lastly, the remaining resist is removed, and a patterned magnetic film in the desired geometry is all that remains. The main benefit of this is that the magnetic film is grown in the patterned state, and, as they showed, this thermalizes the film at small thicknesses while it is being grown [26]. The result was large areas of the crystal that had settled into their lowest energy, two-in, two-out

state while the elements were still small and the thermal energy barrier to flipping was still negligible. There were, however, a relatively large number of vertices that did not obey their corresponding ice rules which create the domains separating differing areas that have reached the ground state.

Work was also done to demagnetize the samples; however, the square ice samples still showed many ice rule violations [27]. As a model for pyrochlore structures it was a problem that ultimately meant the square lattice was not the ideal analogue to the pyrochlores despite providing interesting insight into nanoscale magnetic interactions. To make predictions about the behavior of bulk materials based on a two-dimensional approximation requires the two to be mutually consistent on at least a basic level.

### 3.2 Artificial Kagome Ice

It was suggested that the kagome lattice would be a better candidate for studying geometrical frustration [28] because each vertex has only three elements interacting, and the three-fold symmetry means the interaction lengths are the same among all the sub-lattices. Additionally, the kagome geometry is one of the crystal planes in the pyrochlore structure, and artificial kagome ice has a very high ground state degeneracy [29]. For comparison's sake, the number of possible microstates for the kagome lattice is

$$\Omega_0 = 2^N \left(\frac{3}{2}\right)^{\frac{2N}{3}} \quad (3.2)$$

which results in an entropy of

$$S_0 = k \ln \Omega_0 = \left(\frac{R}{3}\right) \ln \left(\frac{9}{2}\right) \quad (3.3)$$

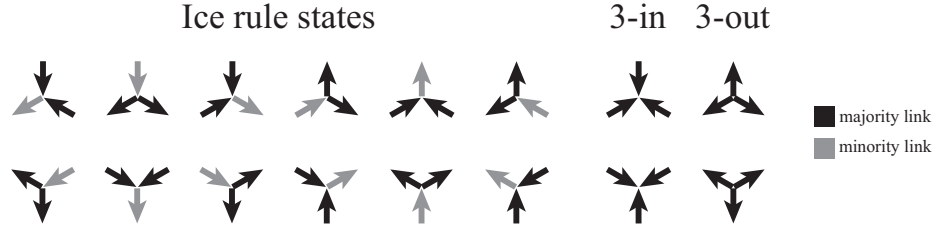
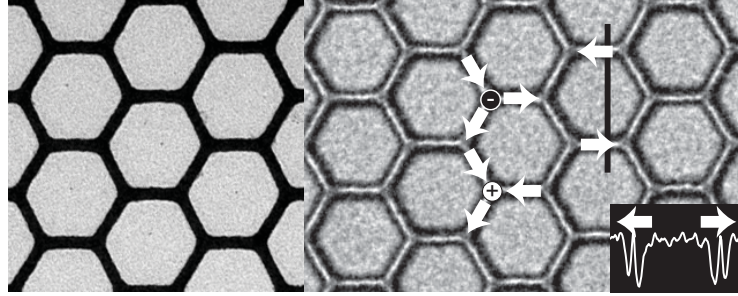


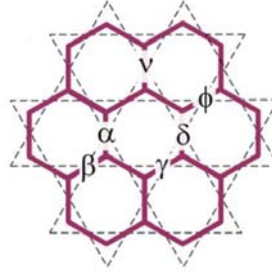
Figure 3.6: **Artificial kagome ice (upper left)** In-focus TEM image of an artificial kagome ice crystal showing the honeycomb structure. **(upper right)** Lorentz TEM image of the kagome crystal showing the magnetic contrast. A  $+q$  and  $-q$  magnetic charge is shown along with the directions of the internal magnetization of the elements. Inset: line profile showing the contrast difference across two elements used to determine the direction of the internal magnetization. **(bottom)** The possible vertex configurations. 3-in or 3-out states have never been seen in our samples, but others have observed them in their crystals [30, 31].

The kagome lattice is made of corner sharing triangles as shown in the white lines of Fig. 3.6. Magnetic elements making up the kagome lattice are placed at the shared corners of the kagome triangles and lengthened until they touch at the centers of the kagome triangles. This increases the magnetostatic interaction between the elements and results in the honeycomb structure of my samples which can be seen in Fig. 3.6. Each element is written twice during the lithography process in opposite directions to remove any shape disorder that would have resulted from the asymmetric vertices.

In 2008, demagnetization studies were performed and compared to results from artificial square ice [5]. The same AC demagnetization technique of [25] was used,

and multiple samples were studied. The goal was to check the theoretical calculations of the spin-spin correlations for the kagome lattice [29]. The correlation between the spins is defined as  $c_{ij} = 1$  when  $\vec{s}_i \cdot \vec{s}_j$  is positive (ferromagnetic); otherwise  $c_{ij} = -1$  (anti-ferromagnetic). The different pairwise correlations that were calculated are shown in Fig. 3.7. The overall value of each correlation is calculated as the average value for each type of spin pair as  $C_{\alpha\beta} = \langle c_{ij} \rangle$  over an entire kagome crystal comprising approximately 10,000 elements [5]. It was shown that experimental spin-spin correlations matched well with theoretical calculations [29]. The value of  $C_{\alpha\beta} = 1/3$  is proof that all vertices obey the ice rule. Additionally, all of the correlations agree with theoretical values in sign and magnitude. Lastly, the dipole energies agree in sign with the correlation values indicating that dipolar interactions are important in the ordering of artificial kagome ice samples [5]. Further evidence of the kagome lattice's rigidity against ice rule violations is supported by the data summarized in Fig. 3.7. After looking through 5,000+ vertices, no ice rule violating vertices were seen, and I have never seen them in the hundreds of *in situ* magnetic reversals I have performed and will present in Ch. 4.

Since this was reported, much of the work in artificial spin ice has focused on crystals in the kagome lattice. Some of the most recent work looks at the topological defects at the vertices resulting from excess magnetic flux. Each vertex has three interacting elements. If the convention of adding  $q$  when an element points into a vertex and subtracting  $q$  when it points out of a vertex, then each vertex will have  $q_{net} = \pm 1$  (or  $\pm 3$  for ice rule violations) where  $q = Mwt$  and  $M$  is the saturation magnetization of the material and  $w$  and  $t$  are the width and thickness of the elements



	Data	Model	$\Delta E_{\text{dipole}}$
$C_{\alpha\beta}$	0.333	0.333	1.0
$C_{\alpha\gamma}$	$-0.158 \pm 0.008$	-0.118	-0.137
$C_{\alpha\nu}$	$0.165 \pm 0.013$	0.101	0.089
$C_{\alpha\delta}$	$-0.130 \pm 0.015$	-0.072	-0.070
$C_{\beta\phi}$	$0.057 \pm 0.007$	0.007	0.082

Figure 3.7: **Spin-spin correlations in the kagome lattice** Experimentally determined spin-spin correlations [5] compared with theoretical calculations [29]. The definitions of the correlations are shown in the schematic above the table. Agreement is quite good, and the value of  $C_{\alpha\beta} = 1/3$  means that all vertices obey the ice rule.

respectively. These topological defects can then be treated as magnetic charges, and reversing the crystal results in the motion of these charges throughout the sample.

### 3.3 Sample Fabrication

Using electron-beam lithography allows one to pattern thin films in a process not too far removed from creating and printing a photograph.

Samples were patterned by myself using a recipe described in detail in Appendix B. Simply, the process involved (1) patterning a resist that was spun onto the substrate followed by (2) depositing a thin film of magnetic material onto the patterned resist, and (3) removing all the excess to leave just the patterned honeycomb lattice.

An image of an entire crystal can be seen in Fig. 3.9.

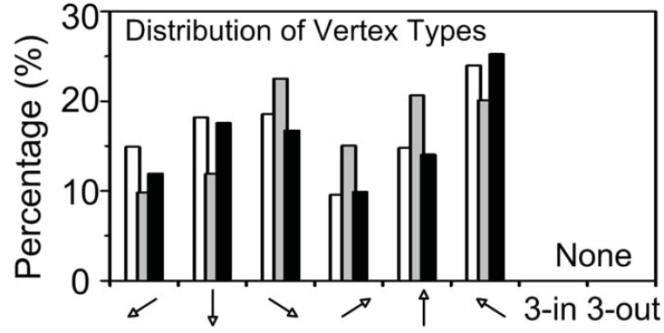


Figure 3.8: **Rigid ice rules in artificial kagome ice** Experimental data showing that our artificial kagome ice samples rigidly obey their corresponding ice rules. No ice rule violations have ever been seen during demagnetization or magnetic reversal experiments.

Additionally, various edge geometries were considered to test the impact on the reversal process. Most crystals were created with “even” edges, meaning that vertices along the edge had only two elements interacting. This allows for easier creation of  $\pm 2$  charges along the edge as these edge vertices are not constrained by frustration as in the bulk of the crystal.

Additionally, crystals with “odd” edges were fabricated. Here, even the edge vertices are frustrated and this makes the crystal a “harder” magnet, requiring higher fields to initiate a reversal process.

I performed ferromagnetic resonance (FMR) experiments at the National Institute Standards & Technology to test how “connected” the elements were. The samples should behave as individual magnetic elements despite being connected to each other in the honeycomb structure.

The sample was placed on a rotating sample holder and placed within two, large electromagnets. Sandwiched on top of the patterned crystals was a wave-guide which was used to guide microwave radiation to the crystals in order to excite the magnetic

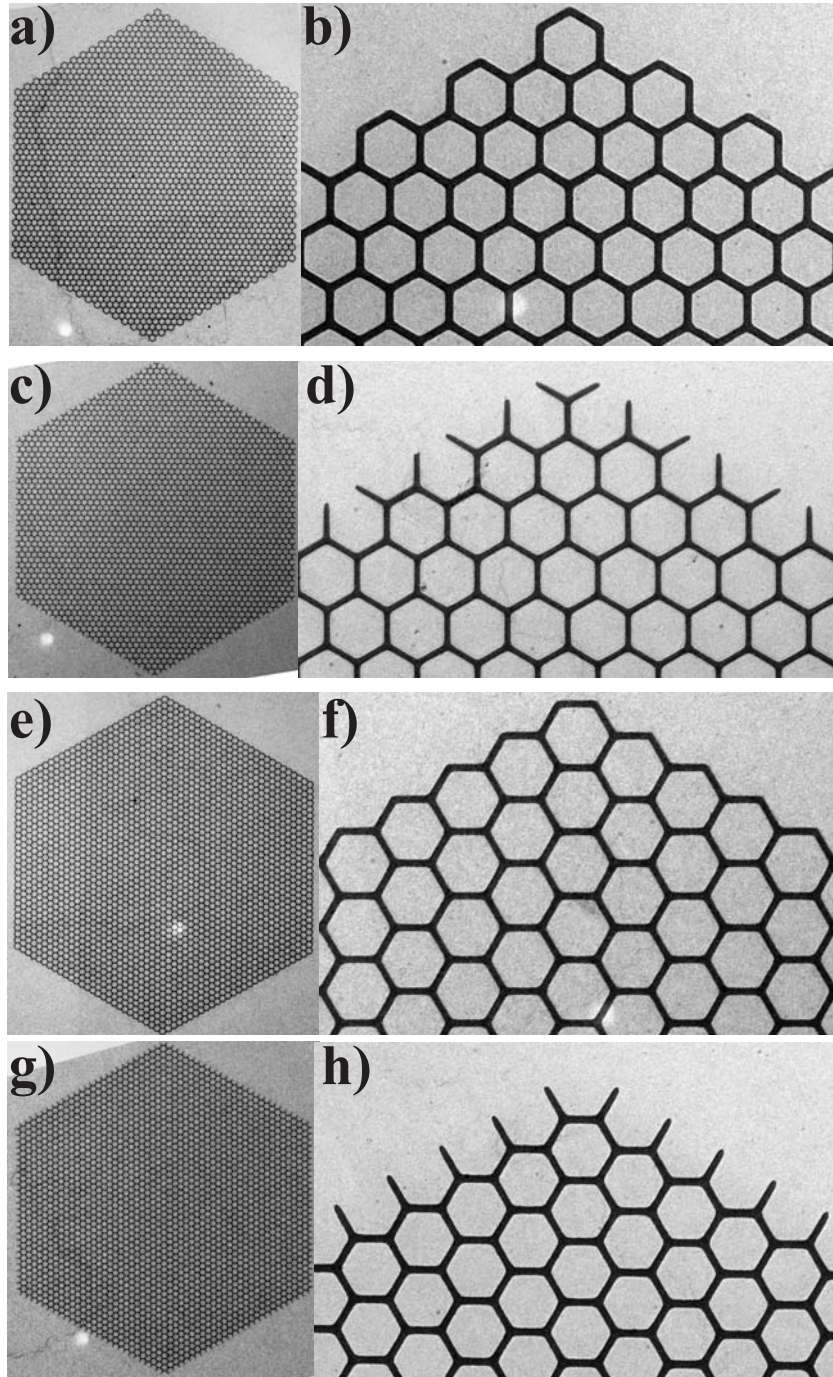


Figure 3.9: **Artificial kagome crystal geometries** TEM images of the edge geometries used in the artificial kagome ice samples. (a–d) The armchair edge geometry was used for most of the following experiments, and even edges were used most often. (e–h) Zigzag edge samples were also created as a check and for the FMR and neutron studies.



moments of the Ni and Fe atoms. The absorption of the incident radiation can be measured as a function of external field, and there is an angular dependence of the absorption. The absorption is greatest when the internal magnetization of the element is aligned with the external field. Due to the shape anisotropy considerations discussed previously, the magnet preferentially places its internal magnetization along its long axis. This means that a larger external field is required to force the magnetization along the short axis. Evidence of this relationship can be seen in Fig. 3.10 where the absorption peaks that define the FMR response vary as a function of both the external field magnitude and the angle between the sample and the external field.

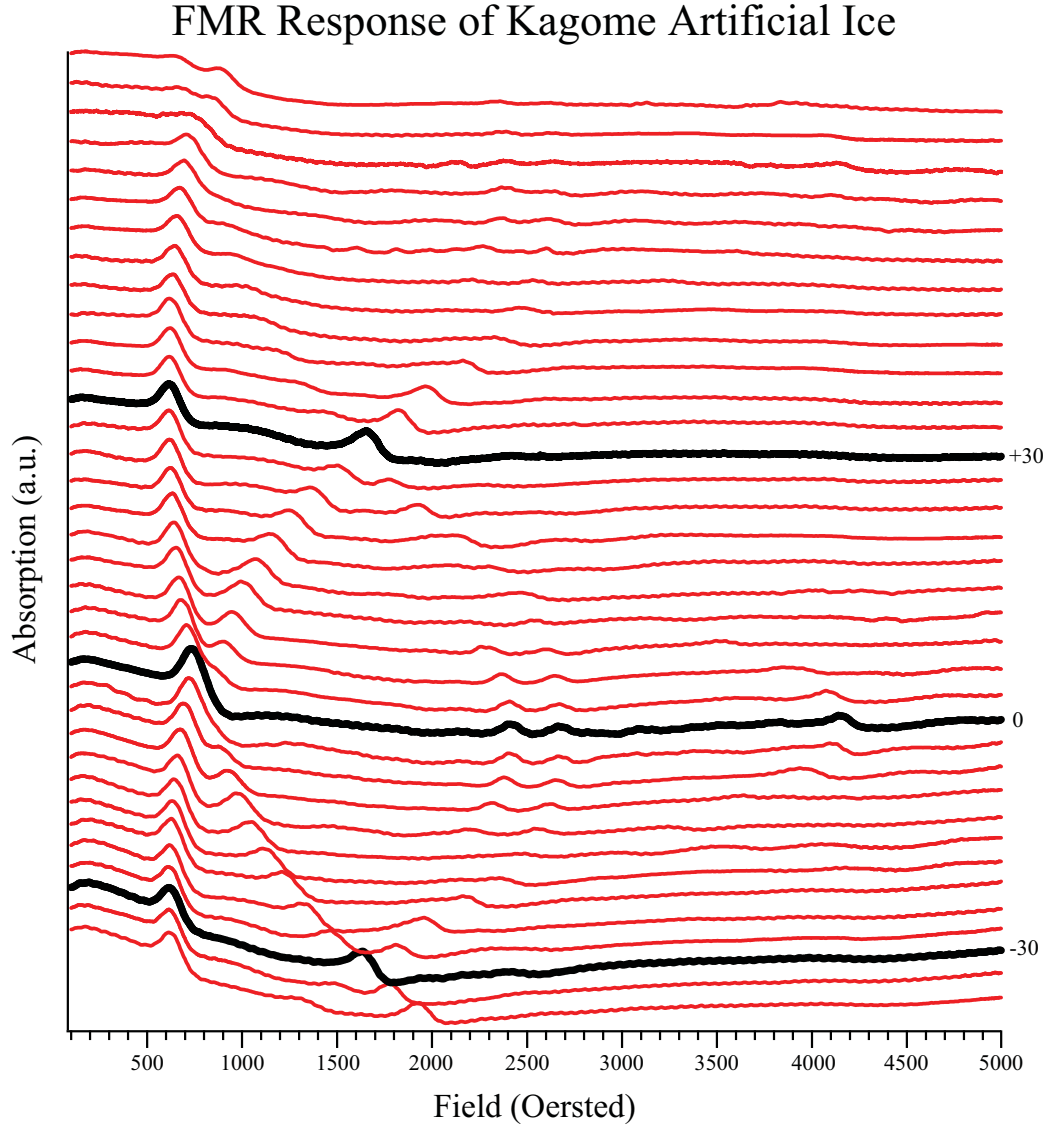


Figure 3.10: **Ferromagnetic resonance data of an artificial kagome ice sample**  
 A cascade plot of the ferromagnetic resonance response of an artificial kagome ice. The different sublattices are indicated by the movement of the resonance peaks as the angle between the sample and the external field is varied.

### 3.4 Lorentz-Force Transmission Electron Microscopy

All experiments were performed using the 2100 LaB6 transmission electron microscope (TEM). As the beam of electrons moves through the magnetic material, the

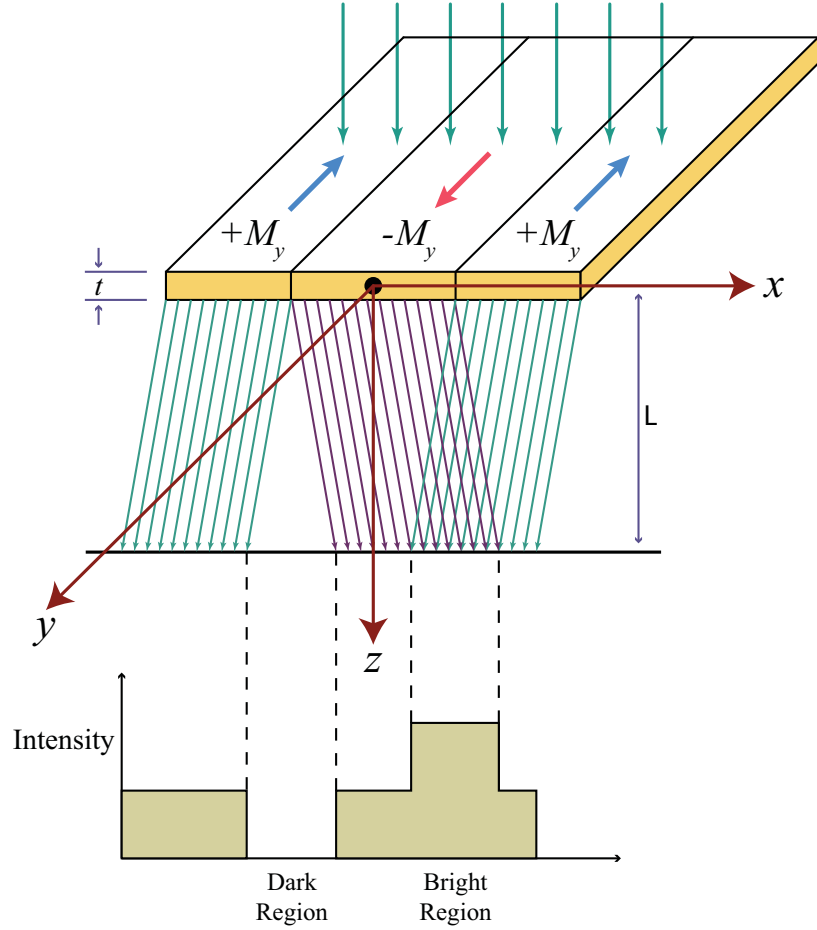


Figure 3.11: **Lorentz TEM beam shift** Illustration of the shift in the electron beam caused by the Lorentz force the electrons feel as they pass through a magnetic material. This shift creates the contrast across the width of our magnetic elements as the beam is shifted away (dark contrast) from one edge toward (bright contrast) another edge.

electrons will be deflected due to a Lorentz force of the form

$$\mathbf{F} = q[\mathbf{E} + (\mathbf{v} \times \mathbf{B})] \quad (3.4)$$

seen schematically in Fig. 3.11. This results in the contrast difference across the width of every element in the crystal as can be seen in Fig. 3.6. This method of characterization grants us the ability to see both the internal magnetization of every element throughout a reversal, and the charge at each vertex as a consequence.

In an electron microscope, the beam is focused in a very similar way to an optical

microscope. The lenses in an electron microscope are solenoids, and the electron beam is created, accelerated, and focused in vacuum. All of our Lorentz imaging is performed at large fields of view to allow us to image as many magnetic elements in the crystal as possible, and this means a low magnification of 400X is all that is required. This leaves the largest electromagnetic lens, the objective lens, unused by the microscope. Using a bipolar power supply and a few LabView programs, we are able to connect to the unused objective lens surrounding the sample and excite it by supplying a small current. In this way, the electromagnetic lens, or solenoid, becomes the source of our external magnetic field. The method allows us to apply fields as high as 1 Tesla, although a typical experiment only requires maximum fields of around 0.2 Tesla. The field is applied along the direction of the microscope column perpendicular to the plane of the specimen. To apply an in-plane field to our sample, we must tilt the samples about the axes  $\hat{x}$  and  $\hat{y}$ , direction perpendicular to the beam axis,  $\hat{z}$ .

### 3.5 *In situ* Application of External Magnetic Fields

All of the following magnetic reversal experiments were performed *in situ* in the transmission electron microscope (TEM). This functionality required the creation of both custom electronics and custom programs to control both the new electronics and interface with the microscope and CCD; details are described in Appendix A. The benefit of performing the reversals in a TEM as opposed to using magnetic force microscopy (MFM) [4, 26, 30] or photo-emission electron microscopy (PEEM) [31] is

the detail that the TEM provides. We are able to capture detailed spin maps of the entire crystal at a constant contrast throughout a reversal process, and the images can be analyzed to determine the spin configuration and the net magnetization of the crystal. I typically choose a field range and step size such that a full reversal is included in 350-450 images. The smaller the step-size, the greater the resolution of the reversal. After comprehensive testing, settled on a step-size of 1 Oersted in-plane which provides a good balance between the dynamics captured and the overall filesize of the image sequences. After analyzing the images, one image corresponds to one data point on an  $M(H)$  plot, and there is a lot of data within each  $(M,H)$  data point.

Our *in situ* setup allows us to control the direction of the external field with respect to the three crystal sublattices as well. I use a double-tilt holder shown in Fig. 3.13. This allows me to tilt the sample along the x- and y-axis to place a component of the field along any arbitrarily chosen direction.

The essential part of the design is to control one of the electromagnetic lenses inside the column of the microscope. The objective lens (OL) is used for two main reasons: (1) the OL surrounds the sample plane in the TEM column, and, as such, the sample is within the region of constant field magnitude throughout the experiments, and (2) the OL is the largest of the lenses within the microscope, and can therefore apply the largest range of field magnitudes. The beam diagram can be seen in Fig. 3.12 where the OL is highlighted. All of the electromagnetic lenses in the microscope are large solenoids which allow the microscope to use magnetic fields to control the beam of electrons moving along the beam path. The physics of the optics is similar to that for photons, x-rays, and neutrons.

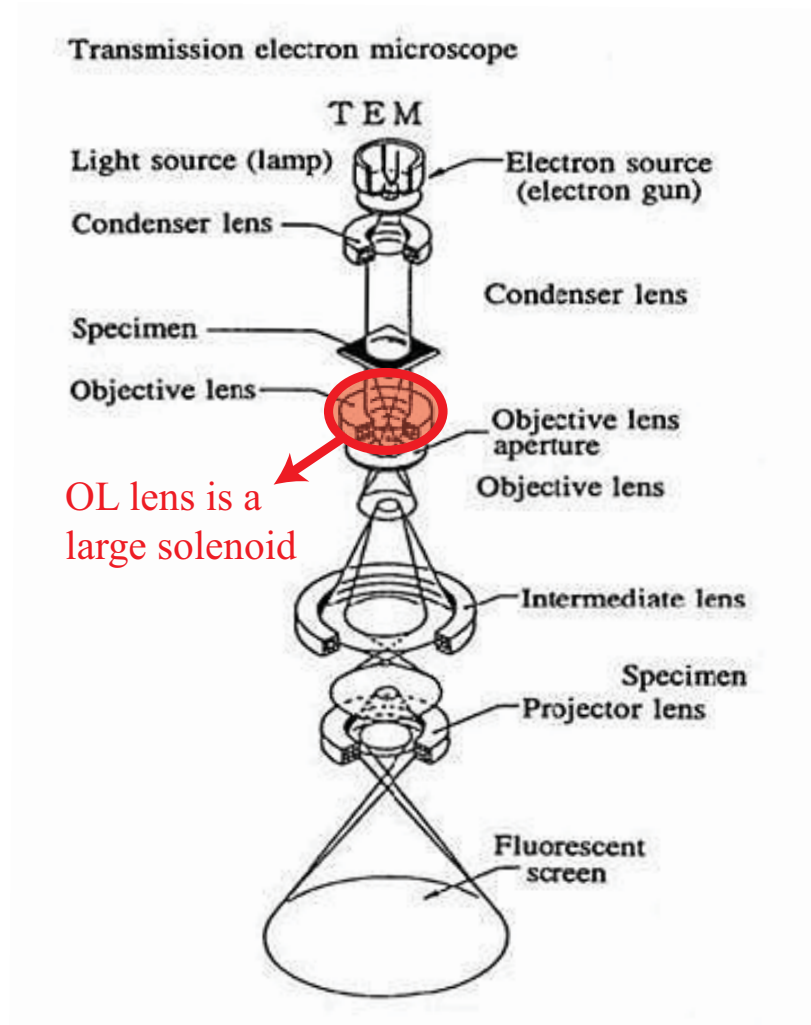


Figure 3.12: **Objective lens as a magnetic field source** The objective lens in the microscope is used as a field source in our experiments. All of the lens in the microscope are solenoids, and thus can be used as a source for an external magnetic field. The objective lens is used because it is the largest lens, it is very close to the specimen plane in the microscope, and it is not used at the low magnifications we image at. Image from [32].

Before we could use the OL as a source for an external magnetic field, the field from the lens needed to be characterized. To do so, we used a custom-made TEM holder with a hall sensor attached to the end [33]. An image of the holder can be seen in Fig. 3.13. Part of the initial testing the manufacturer performs before sending the Hall sensor out is to test the conversion from Hall current to magnetic field. Using this, we can determine a conversion from current applied to the OL and the resulting field. Normally, one could do this using the simple  $B = \mu n l$  relation, but we did not know how many loops are in the OL. Additionally, the Hall sensor can only measure fields in a range  $\pm 400$  Oersted, whereas fields of  $\pm 1500$  Oersted need to be applied for reversal of the kagome crystals. To get this conversion despite it being out of the range of the Hall sensor, we applied a field that would be +2000 Oersted using the manufacturer supplied conversion factor, went back to 0 Oersted, and measured how far from 0 Oersted we were. By doing this for a number of field values, we can get an idea of the hysteresis of the column and approximate it by fitting the data to a parabola instead of the linear polynomial offered by the manufacturer. The deviation from a linear relationship is small, but critical to making connections to our collaborators' modeling.

Since the field is entirely along the direction of the TEM column, and the OL cannot be rotated, a way to manipulate the sample's orientation is needed instead. Tilting the sample creates an in-plane component of the external magnetic field, and allows the field to be aligned with the sample. To do this, I used a double-tilt holder. The sample holder can be rotated about both the x- and y-axis; the z-axis is the column direction, and therefore the direction of the external magnetic field, and by

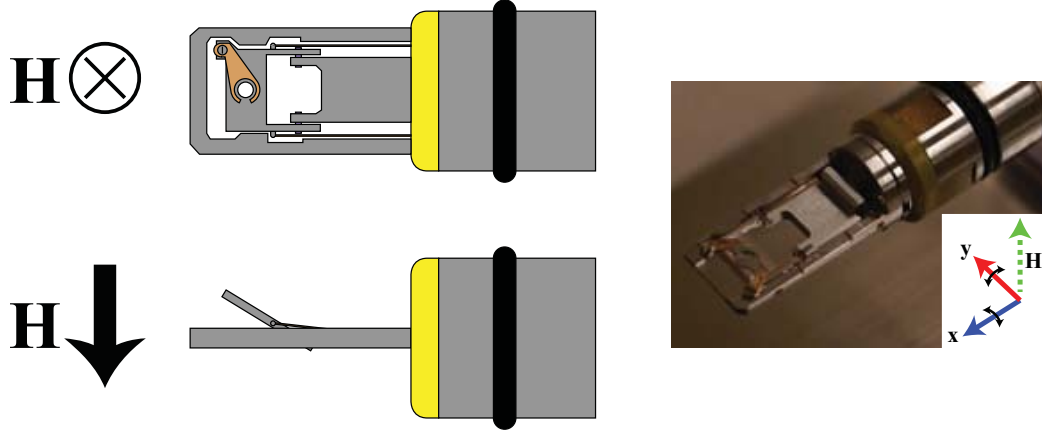


Figure 3.13: **Double-tilt TEM holder** A double-tilt holder such as this was used to “tilt” the sample by rotating it both x- and y-axis to create an in-plane component of the external magnetic field directed along the z-axis. The right panel shows an image of the double tilt holder and the respective  $\hat{x}$ ,  $\hat{y}$ , and  $\hat{z}$  directions.

solving a system of equations, the ‘x’ and ‘y’ tilt can be turned into  $\phi$  and  $\theta$  values, which are the azimuthal and rotation angles respectively. A simple way to understand this is that if  $\phi = 0^\circ$ , there is no in-plane component of the field, but if  $\phi = 90^\circ$ , the entire field is in the plane of the sample. By this reasoning,  $\mathbf{H}_{\text{applied}} = \sin \phi$ . Due to geometric size constraints in the TEM, we cannot actually rotate to  $90^\circ$ , so we use  $\phi = 30^\circ$ , which corresponds to an applied field of  $\mathbf{H}_{\text{applied}} = \mathbf{H}_z \cdot \sin 30^\circ = \mathbf{H}_z/2$

The column of the TEM must also be degaussed before performing any magnetic measurements *in situ*. Under normal operation, there is a field in the range of 1-2 Tesla in the column, which is about 10-20 times the coercivity of my artificial kagome ice samples. Degaussing the column is performed in much the same fashion as demagnetizing an artificial spin ice [5, 25]. The field is reduced through a series of opposite polarity steps starting at 1 Tesla. For this technique, we require a bipolar power supply (we use a Kepco BOP-20-5M) so that both positive and negative field values can be applied. One degauss run takes about 1 minute, and I have found that



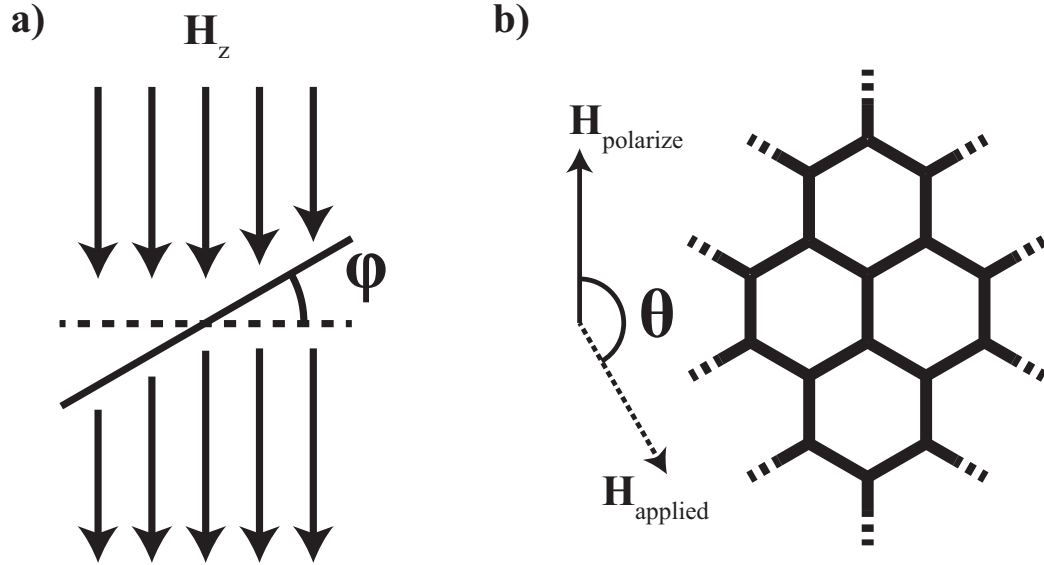


Figure 3.14: **Getting an in-plane field component** (a) By tilting the sample out of the x-y imaging plane, we create an in-plane component of the field,  $H_z$ , which is entirely along the z-direction, and we define the azimuthal angle  $\phi$ . (b) To get a rotation angle,  $\theta$ , we convert the desired  $\phi$  and  $\theta$  angles to x-tilt and y-tilt values which allows us to chose the direction of the in-plane field

after running the degauss protocol 5 times, the field around the sample can be as low as  $0 \pm 2$  Oersted.

Due to image rotation from the TEM column, we must determine the direction of the magnetic field. This is done with a pattern written onto each SiN membrane along with the crystals which can be seen in Fig. 3.15. A series of 13 line doses are written each rotated  $15^\circ$  from each other. After degaussing the column, a 2000 Oe field can be applied and the bars' magnetization will align with the field. The sample is rotated until the magnetization of one of the bars switches upon changing the  $\phi$  angle  $\pm 1^\circ$ . This means that the in-plane component of the magnetic field is perpendicular to the long axis of the magnetic element within  $1^\circ$ . This measurement can then be used to align the sublattices of the crystals written on the same SiN membrane to the external field.

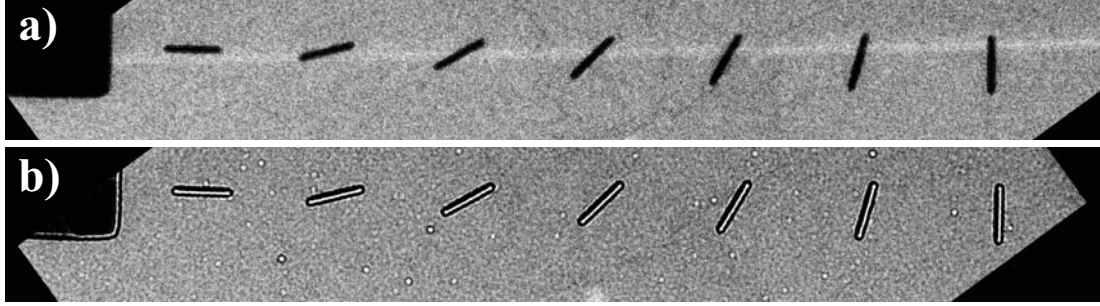


Figure 3.15: **Measuring the direction of the magnetic field** This series of  $\text{Ni}_{80}\text{Fe}_{20}$  bars are written to measure the direction of the in-plane component of the magnetic field. Both in-focus (**a**) and Lorentz contrast (**b**) images are shown.

The field can then be stepped, and images of the entire crystal can be captured throughout the reversal process. The step-size can be chosen arbitrarily, but as I continued to perform reversals it became clear that a small step-size of around 1 Oersted provided the best resolution for the reversals. The reversals provide a crucial insight into the dynamics of the reversal process that are hard to capture using other microscopy techniques. Notably, we see a deviation from the standard model of magnetic objects' reaction to an external field known as the Stoner-Wolfarth reversal [34, 35]. This model predicts that the reversal field for an element will gradually decrease until it reaches a minimum at  $45^\circ$  from its easy axis (or  $45^\circ$  from the long axis of a single-domain element). This is not the case in patterned films with high frustration. In artificial spin ice crystals, the coercive field still depends upon the angle it makes with the external field. However, the minimum is along the easy axis (or the long axis of the elements). This results from the magnetostatic interaction with the nearest-neighbor elements. Certain elements can be pinned in their current state and not able to reverse until neighboring elements reverse as well. This is the case in  $180^\circ$  reversals. The high frustration in the samples prevents elements along

the field direction from flipping because doing so would create an ice rule violation at both vertices it is connected to.

The bulk of the reversals were performed at  $180^\circ$ , but other angles were performed as well. One clear result from the  $180^\circ$  reversals is the appearance of large, connected, highly branched chains of elements reversing as a single event. In each reversal there appear a few very large chains that reverse a significant portion of the crystal at once, followed by smaller chains that complete the full reversal of the crystal. The pinning described above is the cause of this behavior. Elements cannot reverse on their own, so they must wait until a diagonal element flips. The coercivity of the diagonal elements is higher than the vertical elements though. Once a diagonal element flips, the field will be above the coercivity of the vertical elements, and they are free to flip.

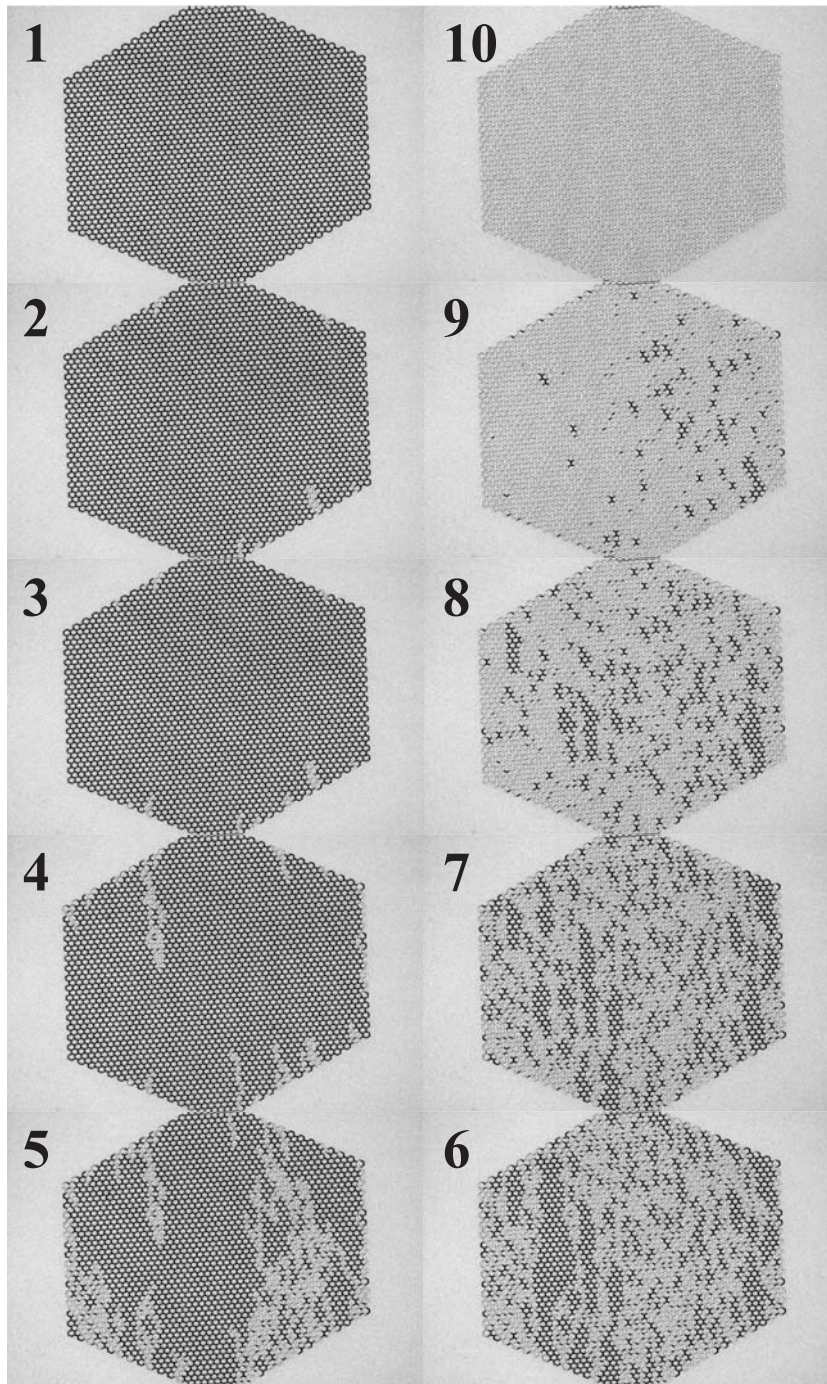


Figure 3.16: **Armchair edge reversal images** A sample of images from an reversal of a crystal with the even edge armchair geometry. Black and white element color indicate unswitched and switched elements respectively. The avalanches can be see here, particularly in the earlier stages.

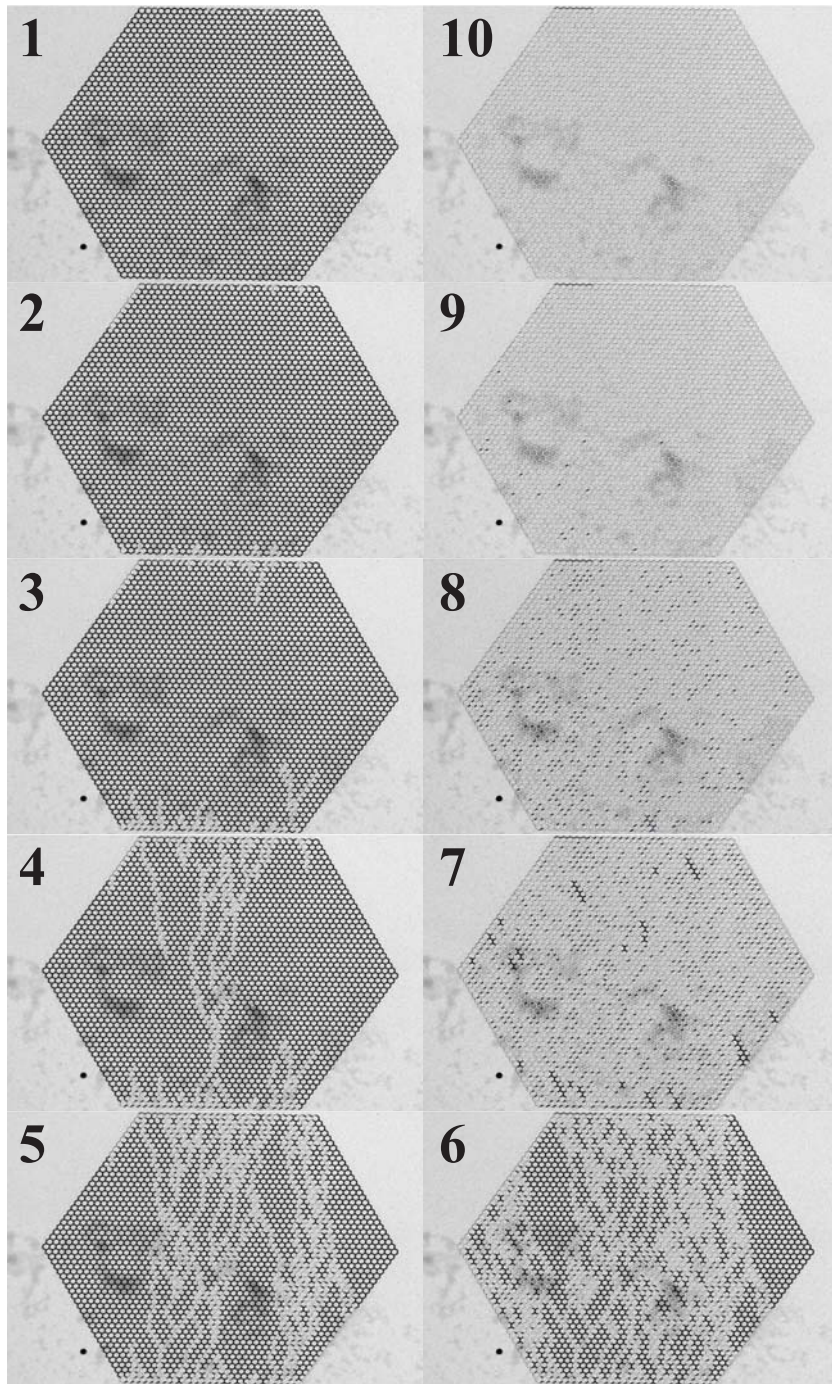


Figure 3.17: **Zigzag edge reversal images** A sample of images from an reversal of a crystal with the even edge zigzag geometry. Black and white element color indicate unswitched and switched elements respectively. The avalanches can be see here, particularly in the earlier stages.

## Magnetization of Artificial Kagome Ice

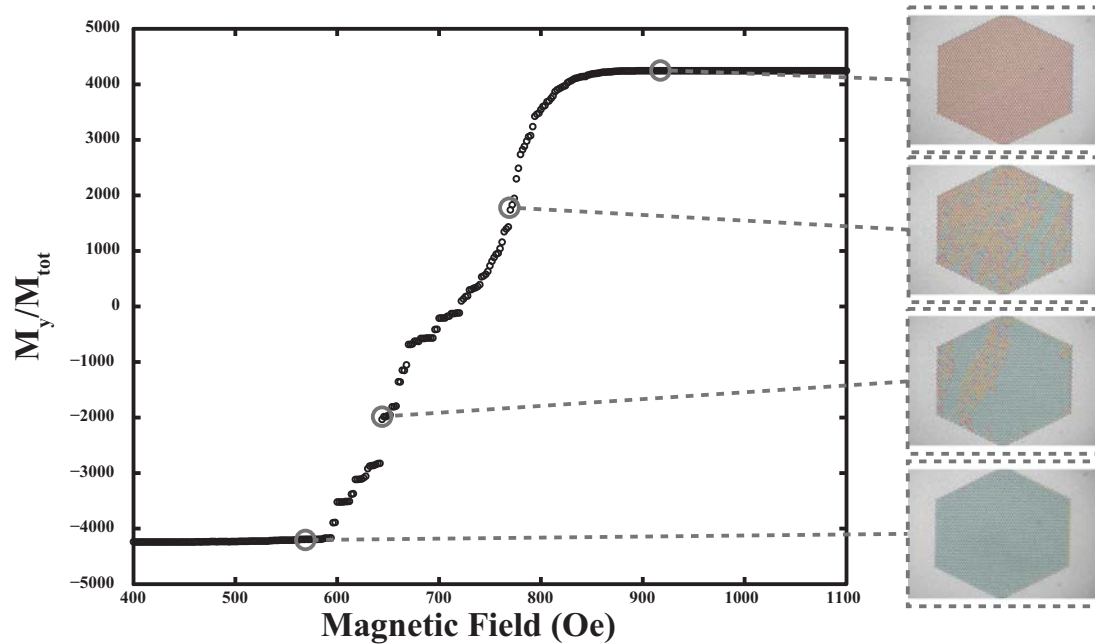


Figure 3.18: **Magnetization data from an image sequence** The image sequence captures a wealth of information about the crystal through a magnetic reversal. Magnetization plots are just one example of the information we can extract from an image sequence. The images along the right edge of the plot are examples of the information stored in one of these data points.

## Chapter 4

### *In situ* Magnetic Reversal

#### 4.1 Magnetic Monopoles in Spin Ice

Once again, bulk pyrochlore compounds lead the way by showing evidence that topological defects in the magnetic ordering are actually magnetic monopoles with a charge defined by the amount of magnetic flux entering or exiting the defect [36–40]. In the pyrochlores, these defects are formed when a magnetic dipole is able to overcome the energy barrier preventing it from flipping. This process is thermal in nature, and has a low, but non-zero, probability of occurring at low temperatures. Fig. 4.1 provides an example of the creation of such a magnetic dipole. Any spin flipping will create an excess flux at both tetrahedra at either end, and these magnetic charges may move freely throughout the material through other spin flipping and “move” the charges through the lattice. It is important to note that because the monopoles are confined to the lattice, and can only move via a thermal spin flip process, they are not actually free particles. Despite this caveat, treating them as pure sources (or sinks) of magnetic charge is perfectly acceptable, and theoretical work has backed up this treatment. They behave like the magnetic monopoles predicted by Dirac in 1931 [41]. These charges can be moved apart from each other without an energy cost. They act like quasi-free magnetic charges able to move through the lattice structure.

Castelnovo *et al.* were the first to formalize the model of mobile magnetic

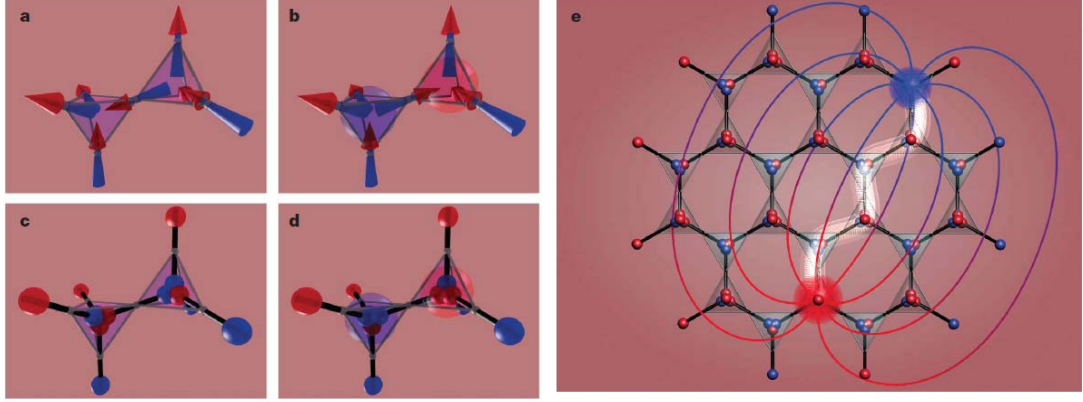


Figure 4.1: **Magnetic monopoles in pyrochlore spin ice (a–b)** It was shown that reversing a single magnetic moment in the pyrochlore spin ices correspond to magnetic monopoles within the lattice. **(c–d)** This can be modeled simply by thinking of the spins as dumbbells instead of moments. **(e)** Once a single moment flips, others are free to flip as well which has the effect of moving the monopoles through the lattice. See [36].

charges in the pyrochlores, and their signature in  $\text{Dy}_2\text{Ti}_2\text{O}_7$  was subsequently measured by Bramwell *et al.* [40]. Instead of treating the interaction of magnetic dipoles in a pyrochlore lattice, they instead modeled the system as an ensemble of interacting dumbbells with equal and opposite charges at the ends of the dumbbells within the tetrahedra [36]. A schematic of the approach can be seen in Fig. 4.1. The energy of this model system is given by the magnetic Coulomb law:

$$V(r_{\alpha\beta}) = \begin{cases} \frac{\mu_0}{4\pi} \frac{Q_\alpha Q_\beta}{r_{\alpha\beta}} & \alpha \neq \beta \\ \frac{1}{2} \nu_0 Q_\alpha^2 & \alpha = \beta \end{cases} \quad (4.1)$$

where  $Q_\alpha$  is the total magnetic charge at site  $\alpha$ , and  $r_{\alpha\beta}$  is the distance between sites  $\alpha$  and  $\beta$ . The term  $\nu_0/2$  is the finite self-energy required to reproduce the net nearest-neighbor interaction correctly.

The charge at each tetrahedron is simply the sum of the charges located there, and the lowest energy state is a configuration where each tetrahedron has zero net



charge. This would require two positive and two negative charges which is simply another way of realizing the Bernal-Fowler ice ordering rules.

Inverting one of the dumbbells creates a monopole at the tetrahedra at either end. Then, the monopoles may “move” through the lattice via subsequent dumbbell inversions. These continuing dumbbell inversions prevent any new ice rule violations from occurring at a lattice site once the monopole arrives; it simply moves through lattice site. These chain of flipping dumbbells are connected to one another in what are known as Dirac strings [36–40]. One dimensional paths connecting a positive and negative magnetic monopole which conserves the magnetic flux between the two monopoles; it is similar to a solenoid.

One problem with the experiment is that only the *signature* of the monopoles can be seen in experiments on real crystals. Neither the monopoles nor the Dirac strings connecting them are directly observable. It is not possible to directly observe the dynamics of the monopoles throughout a reversal process during a neutron scattering experiment. This limitation was one of the reasons why artificial spin ice systems were suggested as the next step to understanding the creation, dynamics, and statistics of magnetic monopoles. The monopoles in artificial spin ice can be seen directly, and their motion through the crystal can be tracked directly depending if the right characterization technique is chosen.

## 4.2 Testing the Monopole Model in Artificial Spin Ice

The first study to look at magnetic monopoles in artificial spin was a simple proof of concept to see if they could actually be seen [30]. Magnetic force microscopy (MFM)

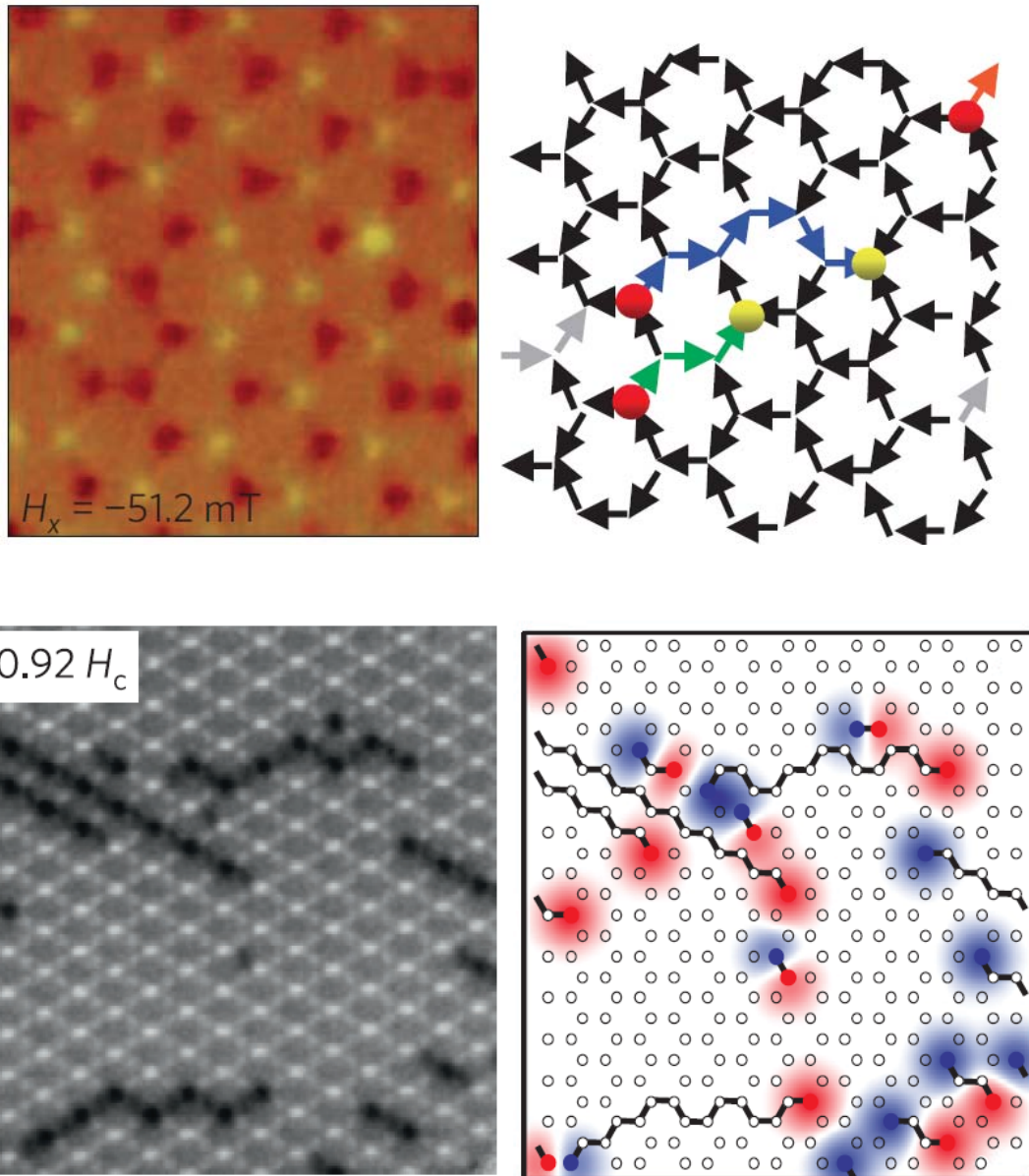


Figure 4.2: **Evidence of monopoles in artificial kagome ice** The two top images are from work by Ladak *et al.* where monopoles were imaged using MFM. See [30]. The charge at the vertex can be seen, but no information about the history of the reversal is present. The bottom two images are subsequent work by Mengotti *et al.* where 1-dimensional strings can actually be seen along with the charges at the vertices. See [31].

was used to image a connected array of cobalt nanowires. The magnetic monopoles appear as bright ( $+q$ ) or dark ( $-q$ ) spots in the MFM image. Only the vertices themselves are visible because MFM requires out of plane magnetization, and the vertices are the only place in the crystal where that occurs. This a result of the high shape anisotropy discussed previously. It costs less energy for the magnetization to be completely in the plane of the patterned film. In a connected lattice, only at the vertices (where domain walls are present) is there any out-of-plane magnetization. By using MFM, all that can be seen during a reversal is the change in sign of the vertices at the endpoints. This means that once again, the avalanche events of the reversal process cannot be directly seen.

Interestingly, in the work of both Ladak *et al.* [30] and Mengotti *et al.* [31],  $\pm 3q$  charges are seen in the reversal. This is in contrast from the rigid adherence to the ice rules we see in our samples [5,6]. Additionally, their choice of Co could potentially create a problem because of its hexagonal structure. The polycrystalline film of their elements will have a larger spread of coercivities than a comparable permalloy film. Furthermore, they chose an element length of  $1\mu\text{m}$ , which may be long enough separate into two domains creating the *appearance* of an ice rule violation; this might be an explanation for their  $\pm 3$  monopoles.

An additional study has looked at the reversal process of artificial kagome ice, and the strings connecting the mobile charges in more detail [31]. Here, photoemission electron microscopy (PEEM) was used to give them information not just about the magnetic charges, but also the path the charges took through the crystal. This allowed them to look at the lengths of the chains during a reversal, and it was found

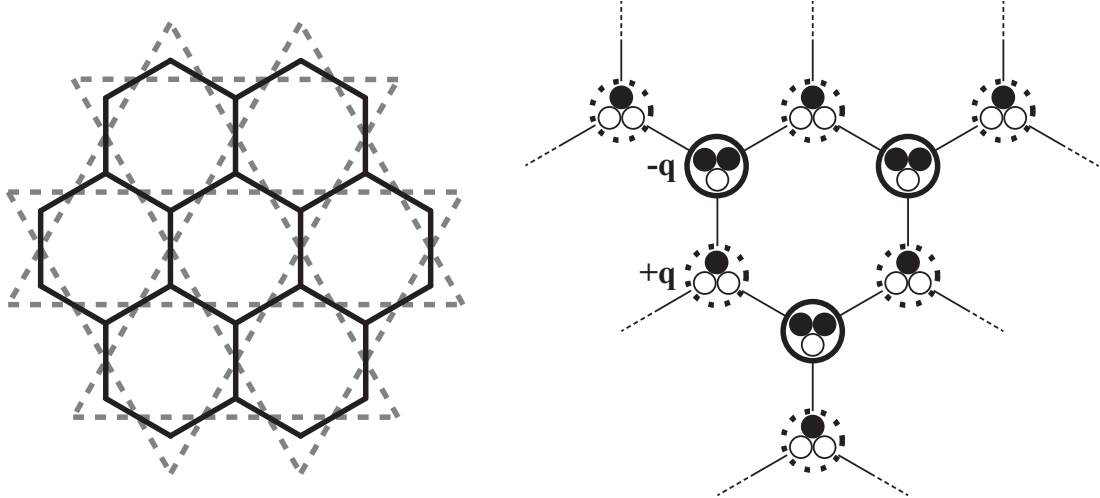


Figure 4.3: **Dumbbell model in artificial kagome ice** (a) Artificial kagome ice can be thought of as a system of (b) interacting dumbbells with the magnetic charge at the ends of the links [42,43] similar to the method used for pyrochlore spin ice [36].

that the chains exhibit power law behavior as can be seen in Fig. 4.2. This is an intriguing result, as it could connect this relatively new system to the well-studied field of self-organized criticality and avalanche phenomena.

With our setup we have a high degree of control over the reversal process and we are able to collect detailed information during the dynamic process of reversing our crystals. This provides us with a unique opportunity to test the theoretical models being developed for artificial spin ices [42,43]. The attempt was to model the behavior in the artificial spin ices as the motion of magnetic monopoles, and the treatment of these monopoles is very similar to that for the pyrochlore spin ices.

The honeycomb geometry of the artificial kagome ice crystals can be thought of as consisting of nodes (vertices),  $i$ , connected through links (elements),  $ij$  to three adjacent nodes. In this way, the Ising spins of the links can be indexed through a variable  $q_{ij}$ . Each node *must* obey the two-in, one-out (or one-in, two-out) ice

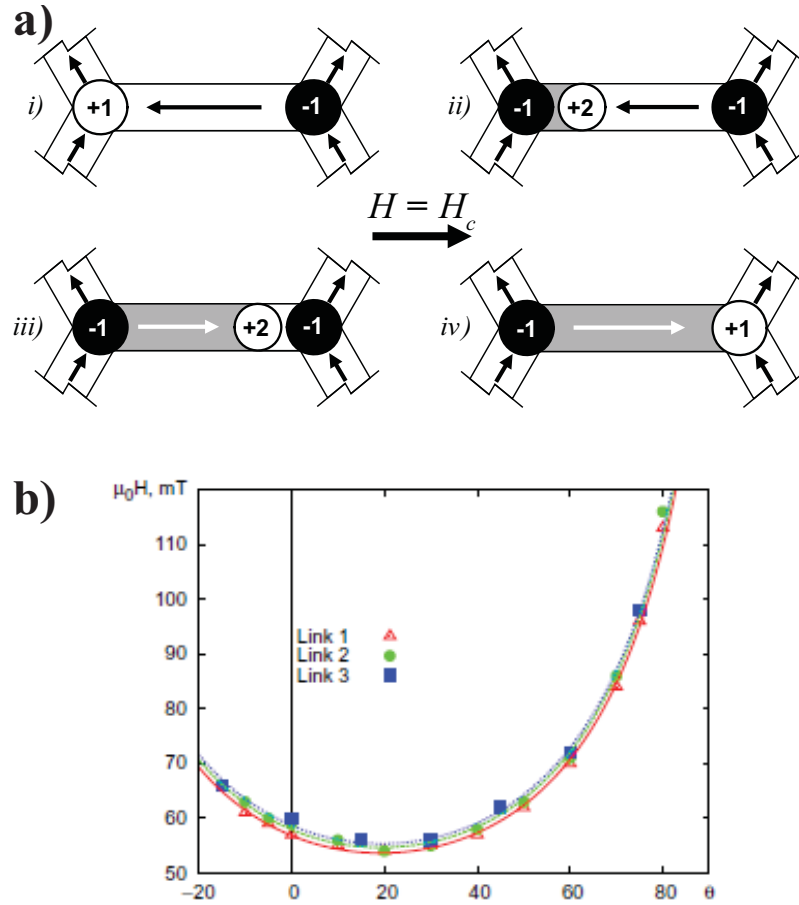


Figure 4.4: **Kagome element reversal through monopole motion** (a) Schematic of the reversal process in artificial kagome ice modeled as magnetic monopoles. Elements are reversed by injected domain walls of  $\pm 2q$  into the element which then propagate along element length. When the element has fully reversed, the charges at each node have changed signs See [6]. (b) The dependence of the critical field  $\mathbf{H}$  on the angle  $\theta$  between the field and the links. This offset is a result of asymmetric field distribution at the vertices. See [43].

rules, and this creates an excess magnetic charge at each node. The charge can be calculated using the convention that when a link,  $ij$ , is pointing into a node,  $i$ , the variable  $q_{ij} = +1$ . If it points out of node  $ij$ , then  $q_{ij} = -1$ . In this way the excess charge at each node,  $Q_i$ , is simply the sum of the three  $q_{ij}$  variable attached to it as

$$Q_i = \sum_j q_{ij} \quad (4.2)$$

where the sum is over the three nearest neighbor sites  $j$ .

The charge,  $Q$ , is a function of the geometry of the patterned elements and the material used. Its value is

$$Q_i = M_s t w \quad (4.3)$$

where  $M_s$  is the saturation magnetization of the material ( for permalloy) and  $t$  and  $w$  are the element thickness and width respectively.

This is helpful because along with Eq. (4.6) for the angle dependence of the coercive field, it is possible to calculate the critical field for these  $\pm 2$  charges (or domain walls) which will initiate a reversal. The best test of that is to look along the edges of our crystals. We create crystals with “even” edges, meaning that the vertices along the edge of the crystals have two elements interacting. This means that when the crystal is polarized, these edge vertices can already have  $\pm 2q$  charges at them; they don’t need to be created as required in the bulk, odd vertices. When we start a reversal, what we see is that these  $\pm 2q$  charges move into the bulk of the crystal and do not stop until they can do so without creating an ice-rule violation. This happens at 20-25 mT which is close to the theoretical estimate of 18 mT [43]. In fact, when we perform reversals on even edge crystals, the reversal is always initiated at the edge,

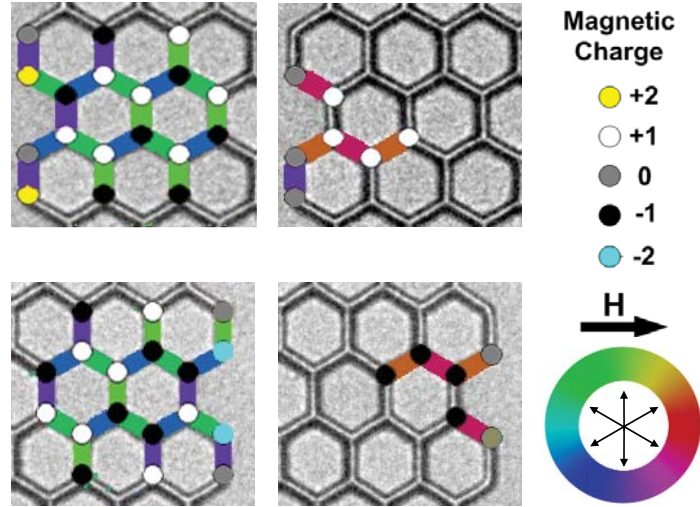


Figure 4.5: **Initiating a reversal on even edge crystals** When an even edge crystal is reversed, stable  $\pm 2q$  charges are created along the edges as can be seen here in the left column of images during a  $150^\circ$ . This means they don't have to be created to start reversal, and they can easily move into the bulk of the crystal.

and continues from these initial chains moving into the bulk.

At remanence, every node has a charge of  $\pm q$ , and the charge can change sign throughout the reversal process. The reversal process in artificial spin ices occurs through the motion of domain walls through the elements. These domain walls reverse the element's magnetization as it moves along its length, and when it gets to another node it can either stop or continue into another link. Domain walls can be thought of as  $\pm 2$  charges. A schematic of the reversal process can be seen in Fig. 4.4.

An experiment was done was to try and create metastable ice-rule violations in our crystals. We have shown that ice rule violations do not exist at remanence, but there was a possibility of seeing them with an applied field. Ice-rule violations are energetically unfavorable, but, in theory, they should be able to occur during the reversal process. Indeed, other groups do see ice rule violations in their crystals during reversal or demagnetization [4, 26, 30, 31]. To do this test, I went halfway through a

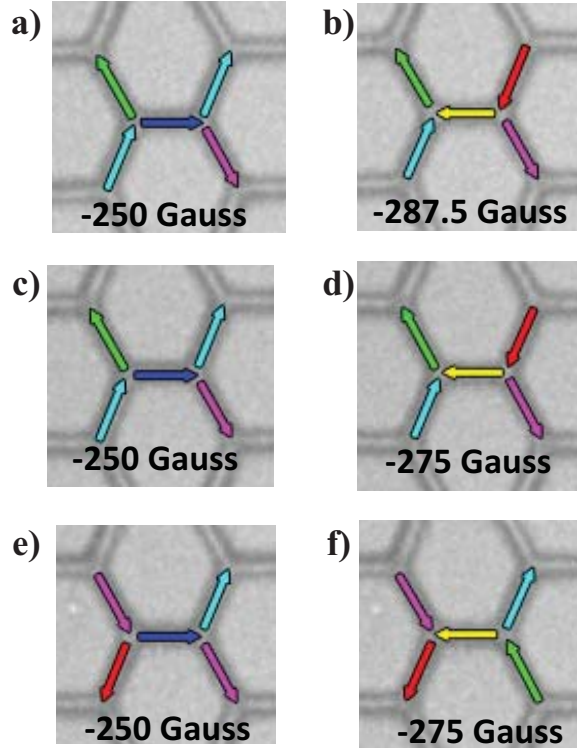


Figure 4.6: **Testing for metastable ice-rule violations** Experiments looking for metastable ice-rule violations. Images were captured with the field still applied (unlike normal image capture conditions). The left column of images is the initial condition, and if the horizontal element flips in any of these three images then a  $-3q$  monopole would be created at the right vertex. Instead, a diagonal element flips along with the horizontal element.

reversal process and looked for vertices in the crystal where ice-rule violations would be created if one element flipped. The results can be seen in Fig. 4.6. The images in the left column are the initial state of the five elements. In all three cases, if the horizontal element which is parallel to the field where to flip, a  $-3q$  monopole (ice-rule violation) would be created at the right vertex. What happens instead, is that a neighboring element (one of the diagonal elements) reverses in unison which removes the  $\pm 3q$  charge from the vertex. The chain ends after the two elements reverse. This is interesting because our crystals avoid ice rule violations even when out of equilibrium.



### 4.3 Disorder in Artificial Kagome Ice

One of the original reasons for using artificial spin ice is its relative ease of fabrication when compared to the pyrochlore systems. Additionally, the geometry of the crystal can be altered during the lithography process to change the interaction energies of the different sublattice. While all of these are a potential benefit of artificial spin ices, care needs to be paid during fabrication to ensure that the disorder among the crystals is as low as possible. A system with interesting geometry but high disorder is of little use to probe the basic science of magnetic frustration, as the disorder could overwhelm the magnetic interactions.

There are primarily two types of disorder we are concerned with in this system: static and stochastic disorder; the total amount of disorder in the system is simply

$$\sigma_{total} = \sqrt{\sigma_{static}^2 + \sigma_{stochastic}^2} \quad (4.4)$$

where  $\sigma_{static}$  and  $\sigma_{stochastic}$  are the standard deviations of the coercive fields,  $H_c/\langle H_c \rangle$ , of each reversal and each element respectively, and the  $\langle H_c \rangle$  values are the mean coercive fields of the corresponding distributions. In this way, the disorder is measured as a percentage of the average critical field for the elements. We have taken to calling this,  $\sigma$ , the “disorder parameter” for the crystal, which can in general contain information about the static lattice imperfections as well as the non-reproducible behavior of the sample during stochastic reversals.

We determine the static disorder by measuring the coercive field distribution for all similar elements. In the case of artificial kagome ice, this means performing a *single* magnetic reversal of the entire crystal of elements, or at least all elements

belonging to a given specified sublattice. Specific examples of this are given below. To measure the stochastic disorder, we analyze the reversal field distributions for all elements across *multiple* reversal runs, normalizing each element's own distribution by dividing its average coercive field,  $\langle H_c \rangle_{element}$ . The root-mean-square deviation of this normalized ensemble distribution is defined as  $\sigma_{stochastic}$ , because its value will be zero if every reversal proceeds in the same manner. One possible way to measure both  $\sigma_{static}$  and  $\sigma_{stochastic}$  at the same time is to perform several reversals at  $\theta_{reversal} = 180^\circ$ . The crystal is saturated along one of the element sublattices. Then, the crystal is then rotated  $180^\circ$ , and the reversal is started from there. An example of the resulting  $M(H)$  plot from such a reversal can be seen in Fig. 4.10.

The results of this disorder measurement can be seen in Figs. 4.7 and 4.8. Both the static and the stochastic disorder use the same data set, but they are each calculated differently. Four reversals are used here to determine the disorder parameters. For the static disorder, switching field distributions are extracted from each reversal for all three sublattices, but the average coercive field,  $\langle H_c \rangle_{reversal}^i$ , is different for each reversal and each sublattice,  $i$ . To correct for this, each element's  $H_c$  value is averaged across all four reversals and then divided by  $\langle H_c \rangle_{total}$  to create a normalized ensemble distribution. This allows us to analyze the static disorder across reversals despite the fact that  $H_c$  and  $\sigma$  may vary from reversal-to-reversal, and, crucially, it allows us to do so *without* changing the shape of the distribution. We can then calculate “new”  $\sigma$  values,  $\sigma_{static}$ , that are the standard deviation for the normalized sublattice distributions and in turn, calculate the associated disorder parameters. Then, standard deviations of the sublattices' switching field distributions

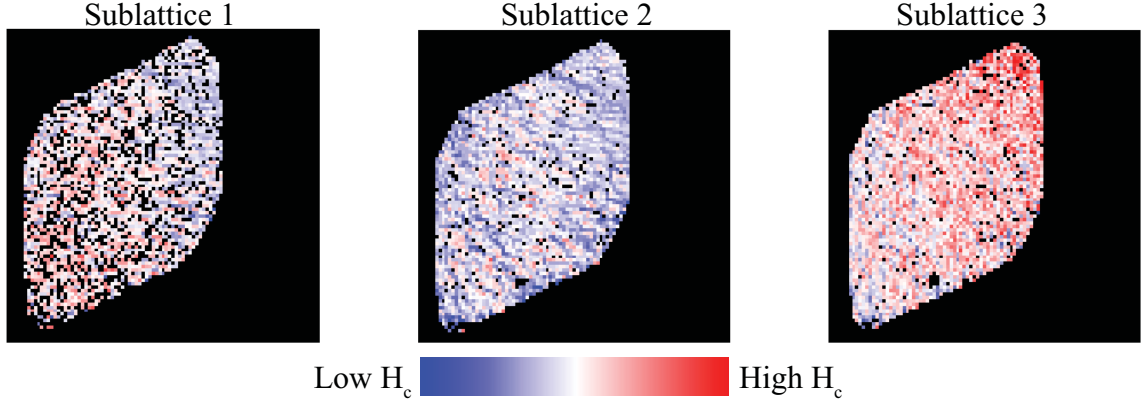


Figure 4.7: **Measuring static disorder** Magnetic reversal results to measure the static disorder in an artificial kagome ice sample. The data for all three sublattices is averaged across 4 complete reversals and shown above. There is a clear difference in the coercive fields across the sublattices. Black regions are elements that were removed because they flipped back and forth during the reversal.

can be calculated, and the average within each sublattice  $i$ ,  $\sigma_{static}^i$  can be compared across the four reversals, yielding  $\sigma_{static} = 0.0482$  for the results shown in Figs. 4.7 and 4.8.

Maps of these coercive fields are shown in Fig. 4.7. There is clear evidence of avalanche events present, for example, in the image of sublattice 2. This indicates that avalanches are not entirely stochastic, and they may still be influenced by the static disorder in the samples.

For the stochastic disorder calculation, we want to compare the spread of an element's reversal field to that of the whole crystal. Essentially, looking to see if individual elements, or even the crystal as a whole, reliably reverse around the same field across different reversals. To do this, we normalize the reversal fields of the individual elements by dividing by the average coercive field of the sublattice,  $\langle H_c \rangle_{reversal}^i$  so that we can compare all four reversals in one ensemble together. We can thus calculate the average switching field of an element in any sublattice relative to the average switch-

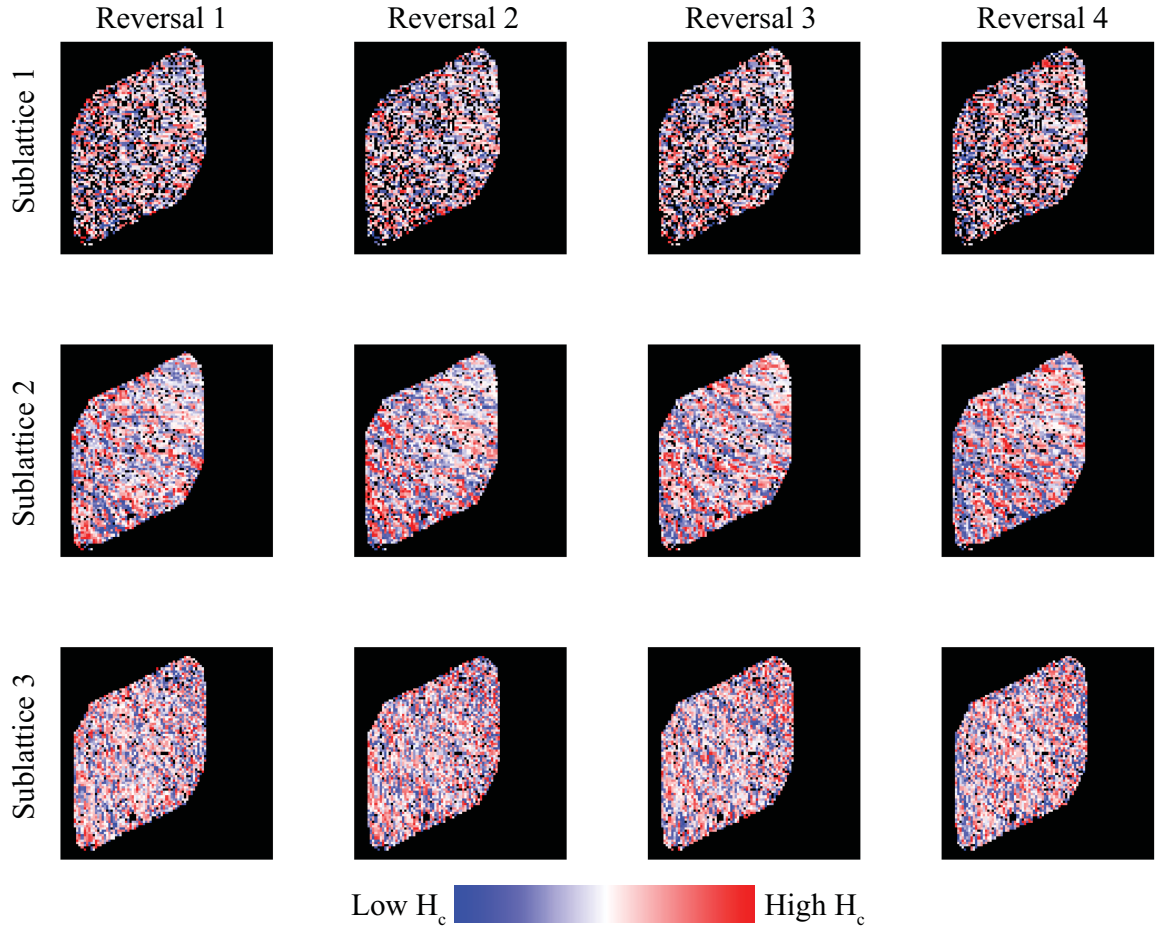


Figure 4.8: **Measuring stochastic disorder** Magnetic reversal results to measure the stochastic disorder in an artificial kagome ice sample. The distribution of each element's coercive field is normalized across all 4 reversals. Black regions are elements that were removed because they flipped back and forth during the reversal.

ing field of the crystal as a whole. This process yields a  $\sigma_{stochastic}$  of 0.0766, and the element-by-element results can be seen in Fig. 4.8. Because  $\sigma_{stochastic} > \sigma_{static}$ , the results indicate that the reversals are largely random in nature. An element's color across the different reversals is not constant, and entire regions of the crystal change from red to blue in Fig. 4.8 in different reversals.

Using the mean values from each column in Table 4.1, the resulting disorder

measurement for these 180° reversals is

$$\sigma_{total} = \sqrt{0.0482^2 + 0.0766^2} = 0.0905 \quad (4.5)$$

However, There is a complication with this method of measuring the static disorder in our samples. If we draw attention to one of the reversal events in the crystal (Fig. 4.9), it becomes clear that all three reversals are switching at the same time in large avalanches. As described previously by the theoretical work of Mellado, *et al.*, nearby reversal events will effect the local field of neighboring elements [42]. The presence of such stochastic avalanche events can contaminate measurements aimed at the static disorder. To extract the static disorder directly, it would be preferable to observe a reversal process that proceeds reproducibly without large avalanches and without any stochastic component. By measuring the static disorder at an angle where only one sublattice reverses at a time, large avalanches are suppressed, the stochastic behavior is minimized, and a detailed coercive field distribution for a single sublattice can be obtained in a way that minimizes the impact of these effects.

Static disorder can manifest in many ways, but the most common is errors from the lithography and lift-off processes. Due to the movement of the electron-beam during writing, and the potential for surface charging, elements will not always be

	$\sigma_{static}$	$\sigma_{stoch}$	$\sigma_{total}$
Sublattice 1	0.0455	0.0699	0.0834
Sublattice 2	0.0453	0.0728	0.0857
Sublattice 3	0.0537	0.0870	0.1022

Table 4.1: **Calculated static and stochastic disorder parameters** The calculated disorder parameters across a series of 4 180° reversals.

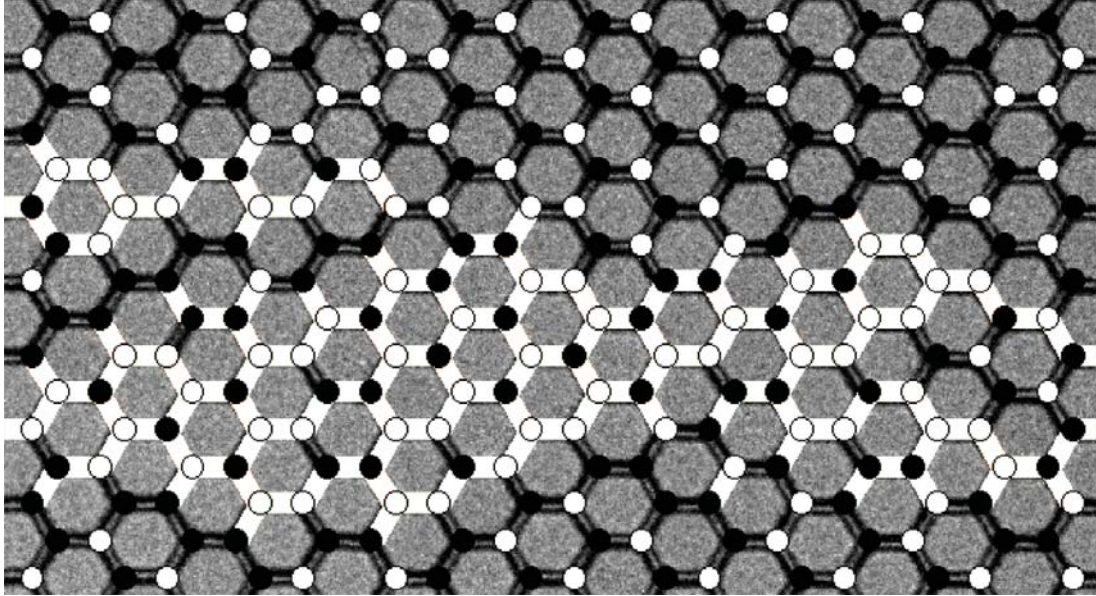


Figure 4.9: **Zoomed in avalanche at 180°** A high magnification image of an avalanche event at 180°. All three sublattices are reversing together which complicates the disorder calculation. We are measuring the disorder parameter of all three sublattices together instead of measuring the spread of critical fields in an individual sublattice.

identical. The radius of gyration of the resist polymer can provide an additional source of roughness, and in practice, the elements can have quite rough edges. Edge roughness and asymmetry of the elements can have a large impact on the magnetic properties of the individual elements, particularly their coercive field and domain wall pinning. Additional sources of disorder can be material composition, lattice geometry, and element dimensions, among others. Stochastic disorder, on the other hand, is largely controlled by the dynamics of the system. In these data, a relatively high amount of stochastic disorder will mean each reversal is completely different from all other reversals.

To accurately measure the static disorder of our crystals, we perform magnetic reversals at angles that will inhibit the creation of avalanche events. By doing so,

we can probe the reversal statistics of individual sublattices separately and obtain a probability distribution of the coercive field for the sublattice throughout the process. Samples are initially polarized, and specific angles from the polarization direction are chosen to ensure negligible overlap of the switching distributions. We decided that doubling the coercive field would be sufficient, so we initially performed reversals at  $120^\circ$ , at which angle, the field is directly along one sublattice, and has half the strength along a second sublattice. The third sublattice does not reverse at this angle. However, we did not observe twice the coercivity for the second sublattice as for the first. Based on the results of Mellado *et al.*, the average flipping field depends on the angle it makes with the external magnetic field [42] based on the relationship

$$H(\theta) = \frac{H_c}{|\cos(\theta + \alpha)|} \quad (4.6)$$

where  $\alpha = 19^\circ$  is an angle offset due to asymmetric distribution of the charge at each junction. This fits nicely to our reversals at  $120^\circ$ . The average coercive fields of the sublattices can be compared, and at  $120^\circ$  we find that the average switching field of the second sublattice is 1.3 times that of the first. This value agrees well with the theoretical prediction of  $H(\theta) = H_c/|\cos(120^\circ + 19)| = 1.3H_c$ .

Sublattices are connected with one another in our crystals, so to reverse one sublattice at a time the coercive fields from the different sublattices need to be as far from each other as possible. At  $120^\circ$  there is still slight overlap, so we ultimately settled upon  $100^\circ$  as theory predicts  $H(\theta) = H_c/|\cos(100^\circ + 19)| = 2.1H_c$ . After doing the experiment, we measured an  $H_c$  increase of 2.58; high enough for there to be zero overlap in the reversal field distributions, but 20% higher than the theoretical

value.

Reversals at  $120^\circ$  and  $100^\circ$  also allow us to calculate disorder parameters for the sublattices by fitting the resulting  $M(H)$  plots to Eq. (4.7). After collecting the reversal data, we can compare values of  $\sigma_H/\langle H_c \rangle$  in our crystals with a number of the experiments performed to date [30,31].

Low disorder is important if the conclusions from artificial spin ice are to say anything about statistical variations due to geometrical frustration. Our results indicate that a connected permalloy lattice exhibits a measurably smaller static disorder, and for the results I report here, the individual elements have a thickness  $t = 23$  nm, width  $w = 110$  nm, and length  $l = 500$  nm give optimal results. Fabrication details are described in App. B.

To determine the disorder in our crystals directly, we fit the  $M(H)$  curves to the expected cumulative distribution function, a superposition of error functions in the case when coercive fields have Gaussian statistics:

$$M_x(H) = \sum_i m_i \operatorname{erf} \left( \frac{H - \bar{H}_c^i}{\sigma_i \sqrt{2}} \right), \quad (4.7)$$

where  $M_x$  is the magnetization along the initial polarization direction,  $i$  indexes the sublattices in order of reversal,  $m_i$  is the amount of magnetic moment carried by the sublattice,  $\bar{H}_c^i$  is the average coercive field, and  $\sigma_i$  is the standard deviation. From fitting the reversal at  $\theta = 100^\circ$ , we obtain a disorder parameter,  $\sigma_1/\bar{H}_c^1 = 3.3\%$ , from the values  $\bar{H}_c^1 = 34.7$  mT and  $\sigma_1 = 1.13$  mT. The second plateau at  $\theta = 100^\circ$  gives a slightly higher disorder parameter of 4.7%, from  $\bar{H}_c^2 = 91.5$  mT and  $\sigma_2 = 4.33$  mT. We believe this is due to a rotational disorder from element-to-element



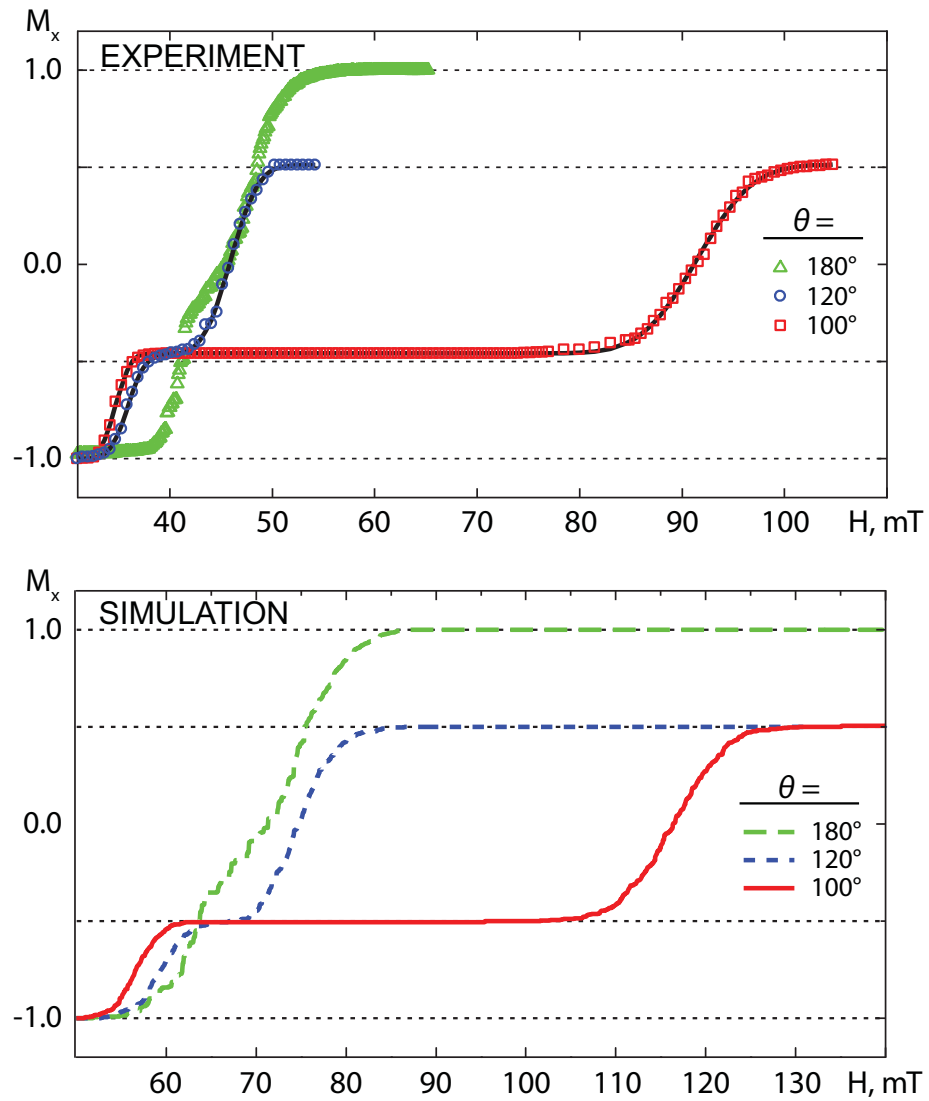


Figure 4.10: **Experimental data compared to theoretical predictions from monopole model (top) Experimental and (bottom) theoretical reversal plots for 100, 120, and 180 degrees.** Experimental data fits the simulated data well, supporting the idea that artificial spin ices can be simply modeled as mobile magnetic charges.

resulting from the asymmetric charge distribution at the vertex, as expressed by the  $\alpha$  offset parameter from Eq. 4.6. Disorder in  $\alpha$  should not be expected to contribute to  $\sigma_i$  when  $|\cos(\theta_i + \alpha)| \approx 1$ , which occurs for  $\sigma_1$  near  $\theta = 100^\circ$  in our system. When  $\theta_i \approx \pm 90^\circ$ , the coercivity diverges and even small rotational disorder would be expected to cause substantial variations. From the reversal at  $\theta = 120^\circ$  degrees, we obtain  $\sigma_1/\bar{H}_c^1 = 3.7\%$ , and  $\sigma_2/\bar{H}_c^2 = 4.6\%$ , confirming the trend of minimum disorder near the minimum  $H_c^i$ , and increasing monotonically with  $\theta$  away from that point.

Also, the reversals at  $\theta = 180^\circ$  have a different character from the others, occurring at higher fields and without a simple distribution function. The data can be fit to Eq. (4.7), but the simple model presented above doesn't match the results as all three sublattices are reversing simultaneously.

From this, we find that the static disorder is very low in our samples, 3.3%, which is a factor of 4-5 smaller than values for other systems [30, 31]. This low amount of disorder is a result of the geometry of our connected elements. Here, charged domain walls always exist at the vertices, even at remanence. For a given magnetic configuration, there is very little change in the location and angle of the charged wall throughout the sub-lattice. The same is not true for a disconnected lattice. The process of nucleating and injecting a domain wall is more sensitive to static disorder in disconnected lattices, as the  $\pm 2$  domain walls must be nucleated from the end of one of the elements instead of simply injected, and any significant edge roughness may influence the nucleation process. This leads to an increase in the width of the static disorder for a disconnected lattice.

To test the broadening of the distribution curve, micro-magnetic calculations

	$\sigma_1/H_c^1$	Composition & Structure
Experiment	0.167	Co, connected [30]
	0.130	NiFe, disconnected [31]
	0.033	NiFe, connected, this work
OOMMF Simulations	0.040	NiFe, connected
	0.089	NiFe, disconnected

Table 4.2: **Experimentally measured disorder parameters** Experimental reversal results and their associated disorder. Theoretical results are shown for comparison. Theoretical results are averaged over 10 different simulations for each lattice.

were performed using the OOMMF software package from NIST [44]. Simulations were carried out for  $180^\circ$  reversals on Y-junctions with random edge roughness, comparable to the fabricated structures, and the results from an ensemble of calculations are shown in Table 4.2 along with values from literature using different materials [30] and different geometry [31]. The simulations give values for the disorder parameter,  $\sigma/\bar{H}_c$ , of 9% for disconnected lattices and 4% for connected lattices. Thus, our simulated reversals agree with the relative relationship of our experimental reversals.

With the success of this monopole model for artificial kagome ice we now have a nanoscale magnetic system that behaves as a classical system and a predictive model to describe it in detail. Magnetic monopoles move through the system to reverse it, and they interact with each other via a Coulomb potential. Simple magnetostatic considerations determine the vertex configurations that are available to the crystal at any given point, and, if necessary, the vertex will reconfigure itself to avoid ice rule violations. There is no need to consider the complicated motion of domain walls throughout the kagome lattice during a reversal. Artificial kagome ice is a system of mobile magnetic monopoles.

## 4.4 Power-law Behavior of Chain Lengths During Reversal

The work described above characterizes the amount of static, or quenched, disorder in our artificial kagome ice samples. The static disorder does not change between successive reversals. To characterize the stochastic disorder is more tricky. This random contribution to the overall disorder calculated in Eq. (4.5) changes with every measurement as can be seen in Table 4.1. Many reversals need to be performed and analyzed before any statistically relevant statements can be made. Because of this, the following data are the result of over 200 reversals at  $180^\circ$ . In all, over 54,000 images were collected of crystals composed of 6300 elements. This amounts to about 351 million element counts. To our knowledge, this is the largest amount of data that has ever been collected on artificial spin ice in general, and because of our reliance upon Lorentz force TEM, it allows us to capture and analyze a statistically robust data set, and make predictions based upon these data.

One aspect of our reversals that is not shown in other experiments is the branching of avalanches. I briefly touched on the highly branched nature of our avalanche events during a reversal. We see a significant degree of branching, such that there are two or three very large “chains” in the reversal, with the rest of the crystal reversing in smaller chains. The size, shape, and direction of the avalanches is random and therefore different between all reversals. Six images from six different  $180^\circ$  reversals of the same crystal are shown in are shown in Fig. 4.14 to illustrate the kind of avalanches we see. Instead of the one-dimensional avalanches of [30, 31], we see significant branching of our avalanches, and our reversals therefore have different dy-

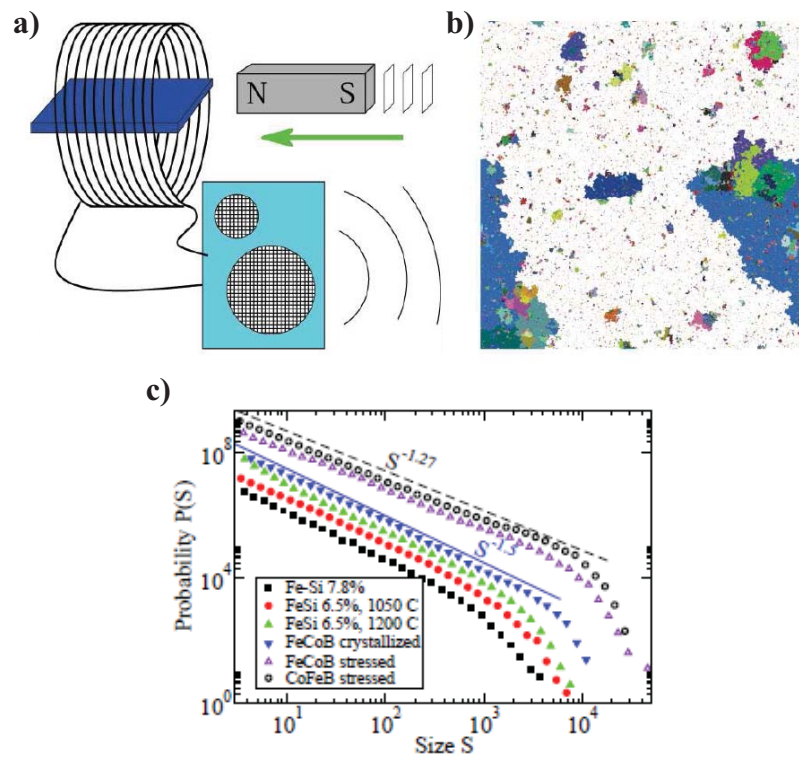


Figure 4.11: **Barkhausen experiment and the resulting power law behavior**  
 A schematic of a Barkhausen noise experiment (a) used to detect pulses associated with the reversal of regions of a magnetic sample (b). When the probability of getting a pulse of a given size is plotted as a function of its size (c) a power law emerges.

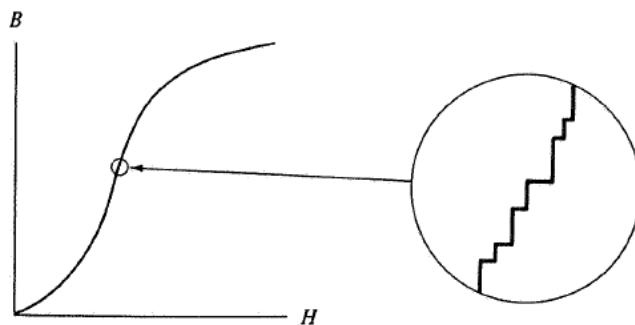


Figure 4.12: **M(H) plot showing the Barkhausen effect** This example M(H) plot looks smooth; however, jagged edges (or steps) appear upon zooming into the plot. Each step is a discrete reversal event. Each of these steps corresponds to an avalanche reversal event in the magnet during a reversal.

namics. The images are at a field of 250 Oe; right where larger reversal events begin to occur, and it is clear that the magnetic configuration is different in all six cases.

The random nature of the reversal is different than the case when we are reversing single sublattices at once where all reversals are virtually identical [6]. Reversals at angles less than  $150^\circ$  are expected to proceed similarly to each other across the reversals [6, 42, 43]. Since elements are reversing separately instead of being induced to reverse by nearest neighbors, the statistics describing the switching field distribution of a sublattice can be extracted from the reversal. This is not the case with  $180^\circ$  reversals.

The seemingly random nature of some magnetic reversal behavior has been studied before. Our particular case is similar to the significant work done on the phenomenon of Barkhausen noise [45]. The Barkhausen effect was discovered in 1919 by Heinrich Barkhausen. In Barkhausen noise experiments, a magnet is wrapped with wire, and the wire is connected to a speaker or oscilloscope; a schematic of such a setup is shown in Fig. 4.11. As the magnetic field is slowly increased by slowly

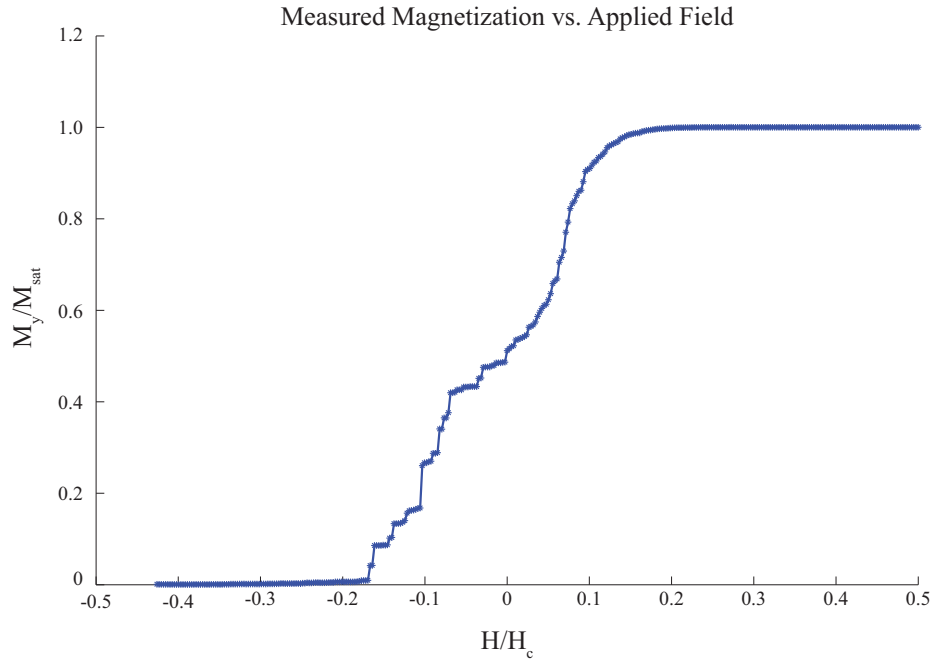


Figure 4.13: **Experimental  $M(H)$  plot showing large jumps in  $M$**  This  $M(H)$  plot of experimental data shows evidence of sharp jumps in the sample magnetization similar to that shown schematically in Fig. 4.12. This is a typical  $M(H)$  obtained during one of my experiments.

bringing a second magnet into proximity with the first, regions of the magnet will flip to align themselves with the external magnetic field; this is a simple reversal process.

However, pulses can be detected as each region of the magnet reverses. The larger the region that flips, the larger the peak detected. The effect occurs no matter how slowly the field is increased; magnets *always* reverse in discrete reversal events. An example of an  $M(H)$  plot is shown in Fig. 4.12. These jumps in magnetization are now known to be due to the motion of magnetic domain walls through the sample as it reverses. This was, in fact, the first evidence of magnetic domain walls despite their existence having been suggested many years earlier [23]. When the histogram of the pulse magnitude is plotted with respect to time, it appears to be random; there is no noticeable trend. If the probability of getting a pulse of a given size is plotted

with respect to the size, however, a power law emerges. This can be seen in Fig. 4.11.

Additionally, the most well known study of Barkhausen noise also uses a patterned sample, albeit, one with dimensions at least 4 orders of magnitude larger [46]. Williams *et al.* fabricated a single crystal of  $\text{Fe}_{96.2}\text{Si}_{3.8}$  in the shape of a hollow rectangle and wrapped wire around opposite legs of the crystal and connected one to a fluxmeter. They were able to show that the domain walls moved in discrete steps as the crystal was reversed.

If we look at an  $M(H)$  plot from one of our  $180^\circ$  reversals we also see steps of various sizes creating a jagged line instead of the smooth, gradually increasing magnetization indicated in the  $120^\circ$  and  $100^\circ$  reversals. Just as in bulk materials and the work of Williams *et al.*, these steps are due to the motion of domain walls throughout the sample.

Barkhausen noise is just one example of a larger phenomenon known as “self-organized criticality” [47]. The idea is that certain systems organize themselves to follow specific patterns when pushed into a non-equilibrium state. The pattern is fundamental to the systems behavior, and it can be thought of as a large-scale organization of the system. Completely different systems exhibit self-organized criticality as well. Earthquake magnitudes for example can be understood in this way. It is orders of magnitude more likely that a small earthquake will happen rather than a large one [48]. When paper is crumpled up, each new fold in the paper emits a sound similar to Barkhausen noise [49].

Power law behavior on its own is not sufficient to claim an understanding of the critical behavior in a system. A power law just shows that big events are less



likely than small events. A quantitative understanding of the processes leading to the power law is crucial.

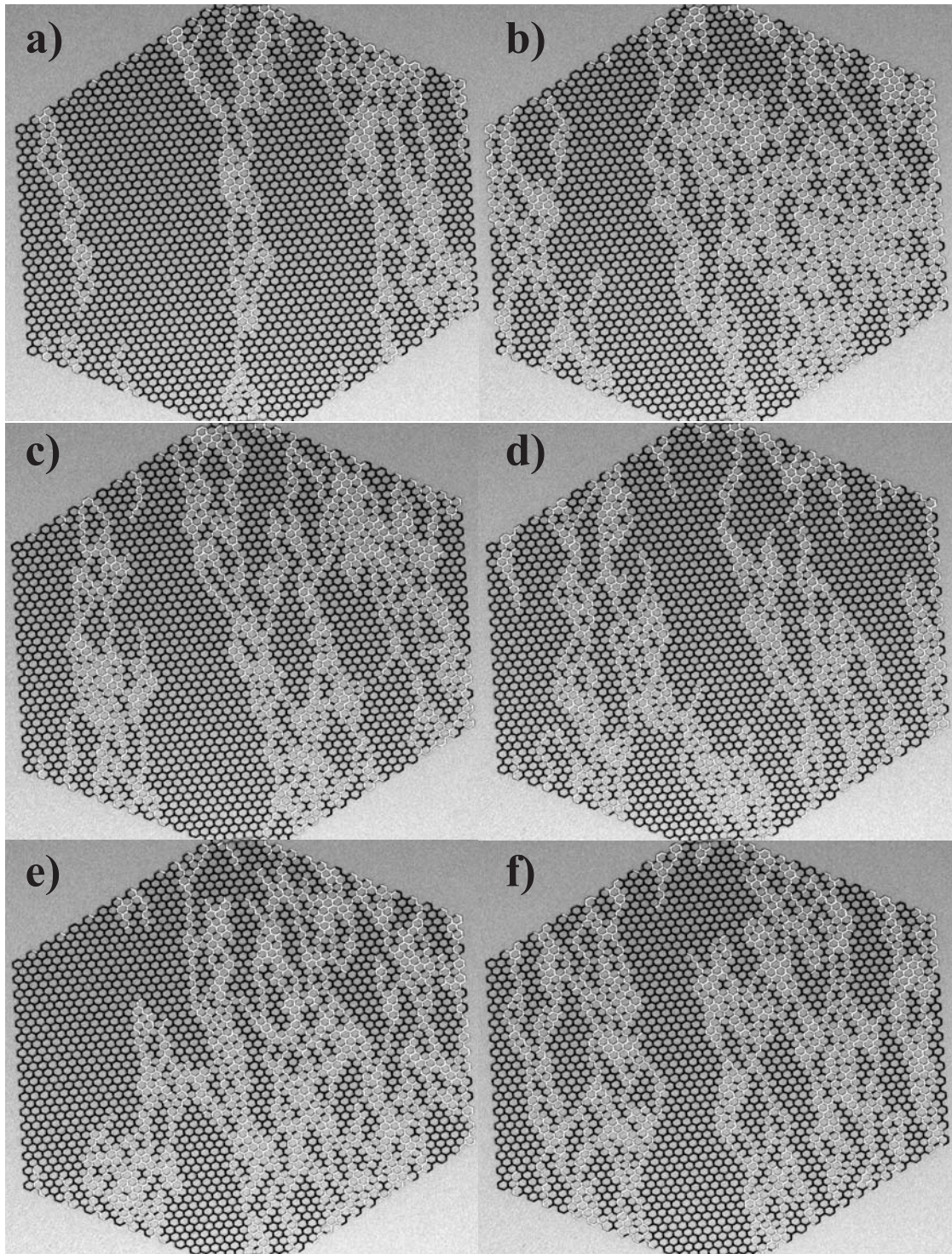


Figure 4.14: **Stochastic reversal through avalanches** Six images taken from six separate reversals. All images were captured after applying a field of 250 Oe. This field is right around when the first chains start appearing, but from the image you can see that the chains themselves are random in size, location, and direction.

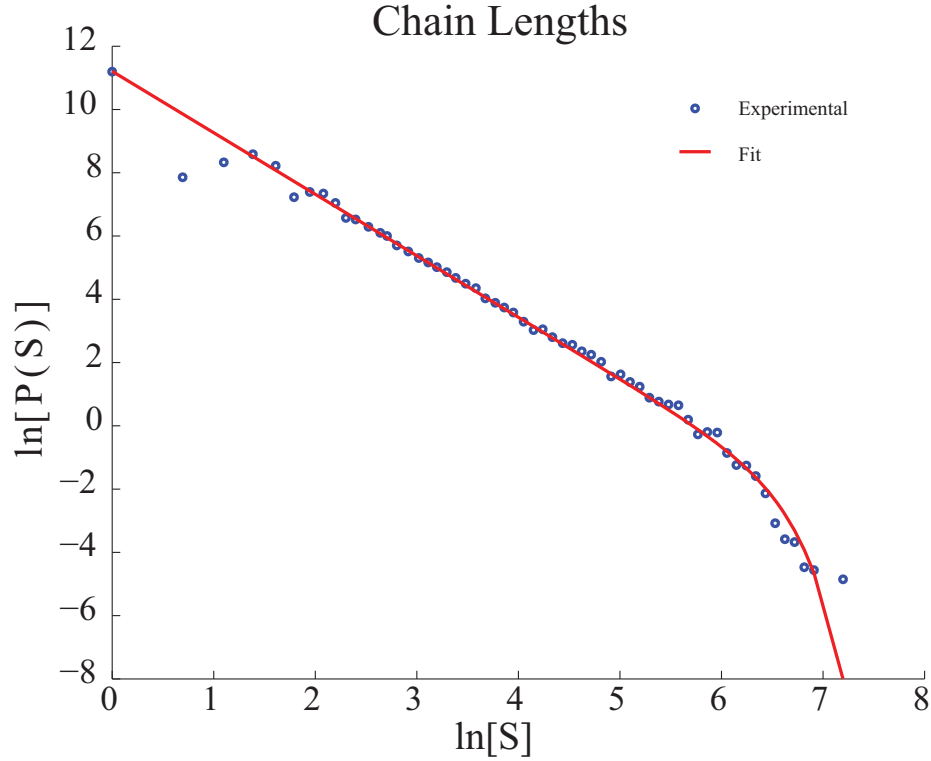


Figure 4.15: **Power law behavior of the reversal avalanches** There is a clear power law behavior of the avalanches we see in our reversals of  $\tau = 1.99$ . Data has been logarithmically binned, and fit to Eq. (4.8).

Work on self-organized criticality has shed light on why such systems behave in these ways, and it can help us understand the stochastic disorder in our system and how the underlying magnetic interactions are causing this behavior. If we make a plot of the chain lengths we see across 92 of our reversals (the ones with sufficient contrast throughout the entire reversal) we get the plot seen in Fig. 4.15.

Just as there are many systems that exhibit characteristics of self-organized criticality, so are there many different functional forms that the power law can take on [50].

Fit Parameter	Value	LI	CI
<b>A</b>	78551	55893	121917
<b><math>\tau</math></b>	1.9935	1.8683	2.1541
<b><math>S_0</math></b>	708	544	883
<b><math>\delta</math></b>	2.4577	1.529	5.6914

Table 4.3: **Power law fit parameters** By fitting the plot in Fig. 4.15 we obtain the values for the parameters of Eq. (4.8) along with the associate lower (LI) and upper (UI)  $1\sigma$  confidence intervals. These values can be used to calculate the fractal dimension of our crystal.

The function that we fit our data to is

$$P(S) = A \cdot S^{-\tau} \cdot \exp \left[ - \left( \frac{S}{S_0} \right)^\delta \right] \quad (4.8)$$

where A is a scaling factor,  $\delta$  is the power law value,  $S_0$  is the cutoff value creating the drop off of the power law, and  $\tau$  is a compression of the exponential behavior.

Another aspect of self-organized criticality is the fractal, or scale invariant, nature of the systems. The behavior of the system should not depend upon the dimensions being considered, and this can be wrapped up in the term “fractal dimension” which is a way of measuring how fast the magnitude of an avalanche increases or decreases when the spatial extent of the avalanche gets larger or smaller. Unlike the more commonly understood Cartesian dimensions, fractal dimensions need not be integers.

We can measure the fractal dimension of our artificial kagome ice samples directly from the fit to the chain length data plot. The  $S_0$  parameter (along with  $\tau$ ) defines the cutoff from the power law. The physical interpretation of  $S_0$  is that it is the largest size of the typical largest avalanche that can fit into our crystal. This is simply defined by the size of the crystal. The avalanche cannot be larger than the

crystal, and as the avalanches approach that size there are fewer of them, hence, the drop-off.

Now, for the avalanche to “feel” the size of the crystal, its length  $S$  needs to be large enough to be on the order of  $S_0$ —or the size of the crystal. The crystal size can be defined in terms of the linear extent  $L$  of the crystal. Our chains are moving along the long axis of a hexagon, or top to bottom in Fig. 3.9a. If we measure this distance in elements (instead of say, nanometers) we get  $L = 75$ , and, by definition of the fractal dimension,  $S \propto L^{d_f}$  where  $d_f$  is the fractal dimension of the crystal. In the large avalanche regime  $S = S_0 = L^{d_f}$ . This means that

$$d_f = \frac{\log S_0}{\log L} \quad (4.9)$$

which gives a fractal dimension of  $d_f = \log 731 / \log 75 = 1.52$ .

A different way to measure the fractal dimension of a system is the box-counting method [47, 51, 52]. The canonical example of this method is by measuring the fractal dimension of a country’s coastline. The measurement is performed by creating a regular grid of size  $\delta$  over the system to be measured and counting the number of boxes  $N(\delta)$  the system touches. Next, the grid is resized, and the same counting procedure is performed; the grid size  $\delta$  is smaller, so more boxes  $N$  touch the system. Finally, plotting the  $N$  as a function of  $\delta$  on a log-log plot will produce a straight line, and the slope of this line will be the fractal dimension of the coastline.

We will do the same measurement but with one minor change. We are measuring the fractal dimension of our avalanches which change over the course of many reversals. Instead of changing the size of our grid, we will just use all of our differ-

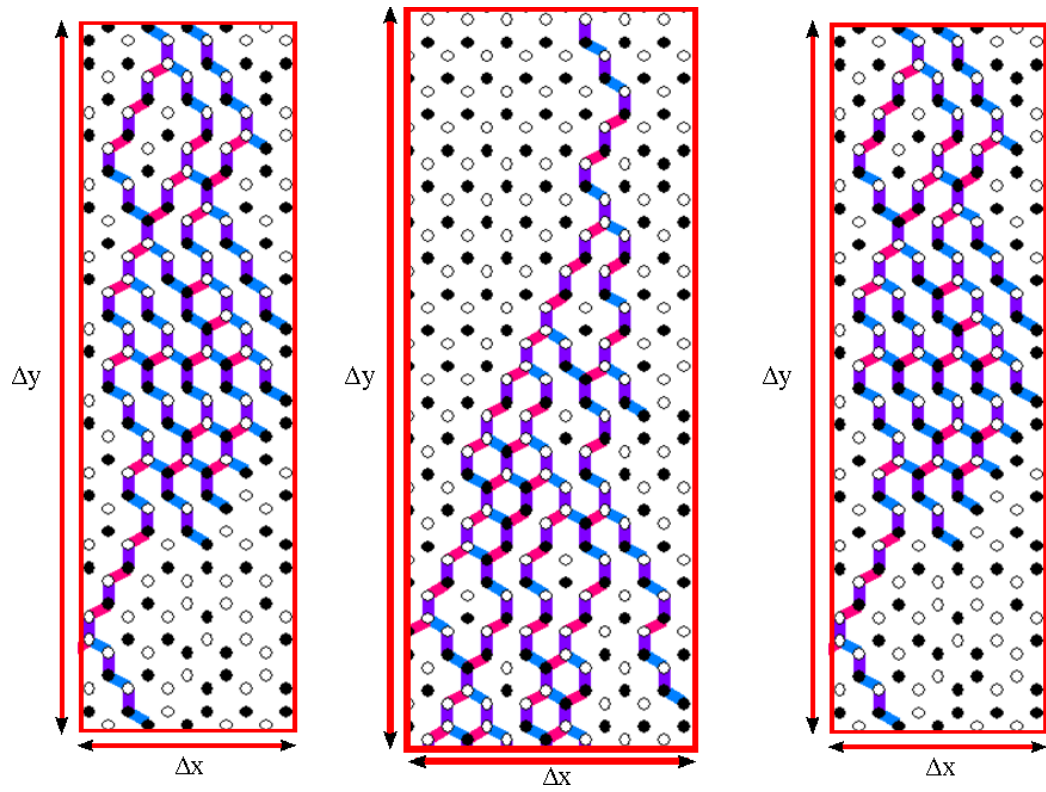


Figure 4.16: **Bounding area of reversal chains** The pervaded area of the chains can be calculated by determining the area of a box that encloses a chain. Long, thin chains have a small area, and short, broad chains have larger bounding areas. We find our chains are somewhere in the middle of these two extremes.

ently sized avalanches. We can create a bounding area around the avalanche defined as  $A_{box} = \Delta x \cdot \Delta y$  where  $\Delta x$  and  $\Delta y$  are the extents of the bounding area in  $x$  and  $y$  respectively. Just like measuring the extent of the crystal  $L$ , both  $x$  and  $y$  are measured in elements. This is helpful as a box that where  $\Delta x \cdot \Delta y = 1$  holds a single magnetic element. Three such bounding area calculations are shown in Fig. 4.16. The bounding area is different for all of our avalanches, and we are concerned with the percentage of the total area our avalanches take up. Our MATLAB script determines the number of elements  $N_{elem}$  in all 103,735 avalanche events in all 92 armchair edge reversals. The last step is to plot the data on a log-log plot which can be seen in Fig. 4.17. The plot is  $N_{elem}$  as a function of  $\sqrt{\Delta x \cdot \Delta y}$ . A best fit through the data reveals a fractal dimension of 1.55.

A fractal dimension of 1.55 is promising as it is within 1.0–2.0 as suggested from the experimental data. If our avalanches had been purely one dimensional, the fractal dimension would have been 1.0. Also, we are below 2.0, which would have been a “front” of magnetic charge moving through the sample, or all elements would flip at once in the crystal.

This is promising for the connection of the artificial spin ices to self-organized criticality. Our system is fractal with a fractal dimension of around  $d_f = 1.55$ . This measurement is corroborated by two different analyses of our data, and is right within the region predicted from experimental images.

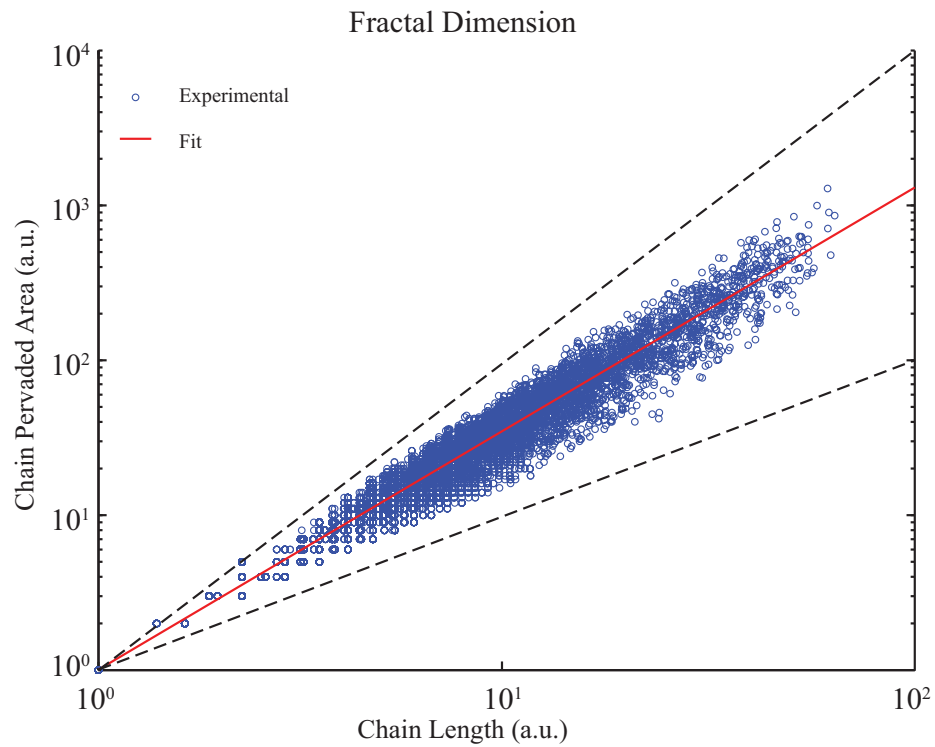


Figure 4.17: **Fractal dimension of kagome avalanches** Plot of pervaded area of a chain as a function of the chain length. We fit the slope of this plot to get a fractal dimension of 1.55. This is in agreement with the fractal dimension measured from the power law plot. In addition to the best fit line, dashed lines show slopes of 2.00 (upper) and 1.00 (lower).



## 4.5 Removing the Avalanches From Reversals

The reversals with the odd edge crystals with individual elements sticking off of the edges as in Fig. 3.9 show behavior that is completely different.

Instead of a reversal characterized by long avalanches of random size, we see the reversal take place mostly (armchair) or entirely (zigzag) within a single 1 Oe field step. The reason for this is that placing additional elements along the outside vertices removes  $\pm 2q$  charges residing along the edge of the crystal. To initiate a reversal, a sample needs to first reverse one of the outside elements; however, doing so would create an ice rule violation immediately, unless a connected diagonal element were to flip as well. This would be similar to the case where we tested for metastable ice rule violations as described in Sec. 4.2. Thus, the reversal can take place in two possible ways (1) reverse the edge elements and create ice rule violations unless a neighboring element switches as well, or (2) wait until the external field  $\mathbf{H}$  reaches the switching field of the diagonal elements.

According to Eq. (4.6), the switching field of the elements parallel to the field should be  $H(\theta) = H_c/|\cos(180^\circ + 19^\circ)| \approx H_c$ , and for two diagonal sublattices it will be  $H(\theta) = H_c/|\cos(180^\circ \pm 60^\circ)| = 2H_c$ .

When we look at the reversals (Fig. 4.18) we see that the crystals don't show ice rule violations but instead show higher coercivities. The crystal is stable until the switching field for the diagonal sublattices is reached. Once the external field reaches  $2H_c$ , it is twice the switching field of the parallel elements  $H_c$ . This means that as soon as a diagonal element switches, the vertical element it is connected to

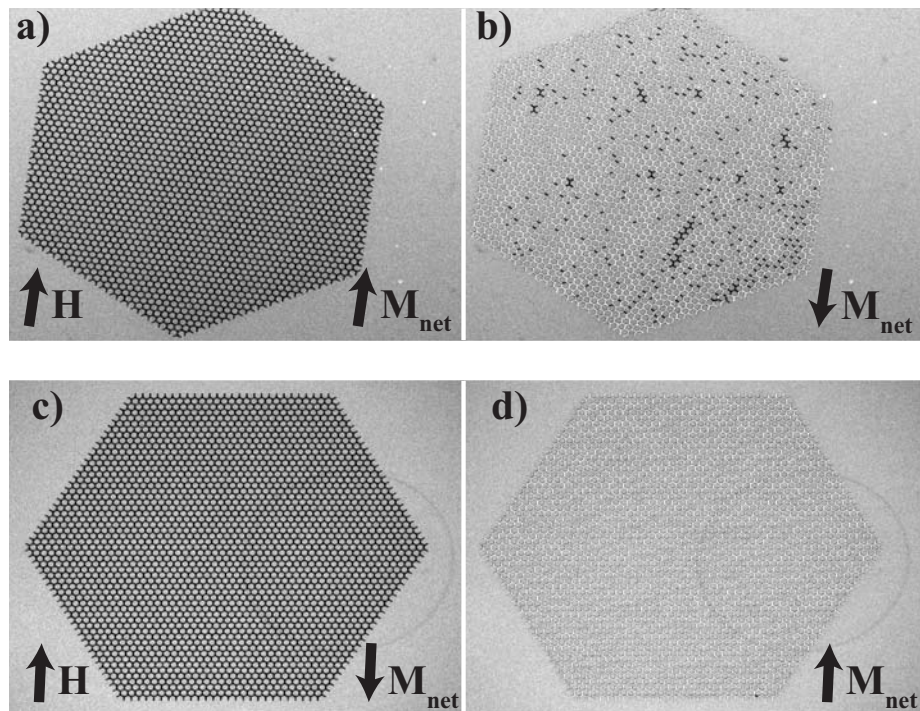


Figure 4.18: **Odd edge crystal reversals** Odd edge crystals with both the (a) armchair and (b) zigzag geometry. Both magnetic reversals show one very large reversal, and in the case of the zigzag geometry, the entire crystal reverses as a whole.

also switches. Additionally, because the fabricated samples have very low disorder, it is likely that next-nearest neighbor elements in the diagonal sublattices can also switch. In this way, the reversal event can move through the entire crystal at once instead of the punctuated motion observed in even edges.

Thus, by simply changing the edge geometry, we have completely altered the behavior of the crystals in an external magnetic field. This is an example of a material whose bulk properties are entirely determined by the structure of its surfaces, in a way that could in principle be predicted and controlled. The system changes from that of a highly stochastic system to one that has dynamics that are largely repeatable across reversals. Even more interesting is the fact that despite the fundamental dynamics of the system being different, the monopole model still describes the system very well. This seems to indicate that the monopole model is quite robust.

## Chapter 5

### Investigations of Long-Range Order

#### 5.1 Dipolar Interactions in Pyrochlore Spin Ice

As mentioned previously, the pyrochlore spin ices are frustrated as a result of their crystal structure. The strong magnetocrystalline anisotropy limits the degrees of freedom of the magnetic moments of the rare earth atoms and the system is not able to settle into a unique ground state. This degeneracy of the ground state can be seen in the spin correlations which can be probed using high-angle neutron diffraction.

In this technique, a beam of neutrons is focused on a single crystal of pyrochlore spin ice. As neutrons do not carry any charge, they can easily penetrate and interact with atomic nuclei. Importantly, neutrons can also interact with the internal magnetic fields of a sample, and, by doing so, provide information about the compound's magnetic characteristics.

In previous neutron scattering experiments, it was shown that  $\text{Ho}_2\text{Ti}_2\text{O}_7$  has a disordered spin ice state in the mK range [12, 17, 54–57]. Bramwell, *et al.* furthered the research by studying the details of the spin correlations within this disordered spin ice state in  $\text{Ho}_2\text{Ti}_2\text{O}_7$ . They were investigating how important a role the dipolar interaction among the magnetic moments plays in the correlations, and they did this by modeling their experimental data both with and without dipolar interactions [7]. Results of the experiment can be seen in Fig. 5.1. The sample's magnetic moments

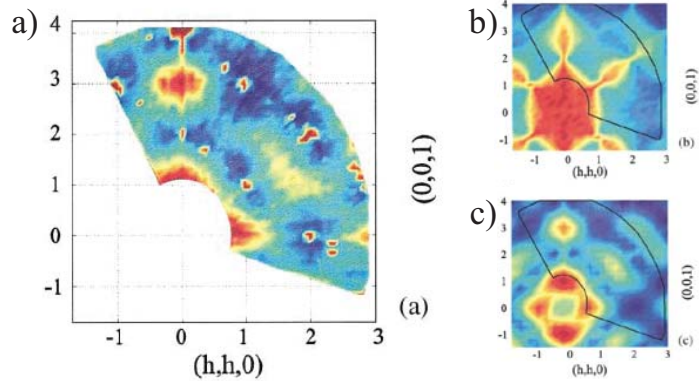


Figure 5.1: **Dipolar interactions in pyrochlore spin ices.** (a) High-angle neutron scattering intensity plot from a  $\text{Ho}_2\text{Ti}_2\text{O}_7$  experiment [7]. The data was modeled (b) without dipolar interactions and (c) with dipolar interactions. The simulated intensity plot that includes the dipolar interactions matches the experimental data much more closely. From [53].

are in a disordered state, but the scattering intensity is not entirely diffuse, as would be expected for a completely disordered system with no preferred spin orientations [7].

As can be seen in Fig. 5.1a, there are regions of relatively enhanced (and suppressed) scattering intensity that indicate that certain interactions among spin are preferred.

These narrow regions of scattering intensity, or “pinch points”, are indicative of a very specific direction for the spin correlations along one of the crystal directions.

These are understood as arising from the dipolar interactions in the system [58, 59].

Nearest-neighbor correlations (Fig. 5.1b) produce a model crystal that obeys the ice rules, but the modeled data clearly do not recreate all of the neutron scattering features on their own.

Dipolar interactions are also required to produce an accurate, simulated neutron scattering intensity map [7], including these correlation effects observed experimentally [7].

Such pinch points have been further investigated recently

in the context of the so-called kagome ice [111] plateau of dipolar spin ice [60], where

they are attributed to a smooth transition where entropy disappears gradually as a

function of external parameters.

In theory, these correlations should also be present in the artificial spin ices. The magnetic elements should still have a long-range, dipolar interaction with each other. Questions remain about how strong this effect is, and if it will result in similar scattering intensities.

To look for dipolar interactions, I used a neutron scattering technique called *off-specular neutron reflectometry*, that is better suited for the two-dimensional geometries of the artificial spin ices.

## 5.2 Off-specular Neutron Reflectometry

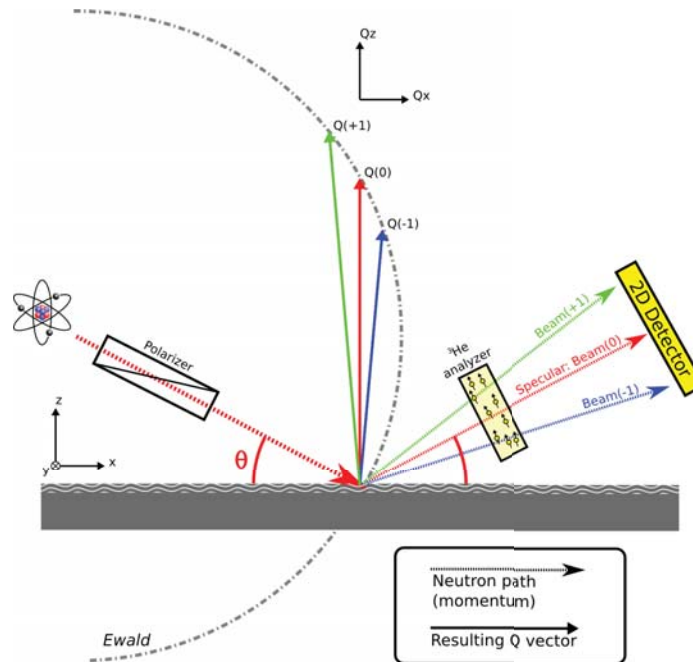


Figure 5.2: **Schematic of off-specular reflectometry geometry** The geometry of a typical off-specular neutron reflectometry setup for a thin film sample. Both the specular beam ( $Q_0$ ) and two off-specular peaks ( $Q_1$  and  $Q_{-1}$ ) are shown.

Specular reflection is the commonly understood type of reflection where the angle of reflection,  $\theta_r$ , is the same as the angle of incidence,  $\theta_i$ ; mirrors are the most common example of specular reflection. Specular reflection is a special case of reflection requiring smooth, flat surfaces off of which to reflect incident radiation.

Off-specular reflection (or diffuse reflection) occurs when something in the material causes the reflected angle to be different from the incident angle. This can happen for many reasons (surface roughness, in-plane variations of index of refraction, etc.), and off-specular reflection can provide information about the in-plane characteristics of a sample. For this reason, off-specular reflectometry is an ideal tool for investigating magnetic thin film samples such as my artificial spin ice samples.

For this reason, we performed a neutron scattering experiment to study the nature of the in-plane interactions of our array of magnetic elements to look for long-range correlations. This is essential to understanding how artificial spin ice materials behave, and it is thus important to explore their configuration-space. Using off-specular reflectometry, we probe reciprocal space for special regions which show sharp, ordered correlations in specific directions but simultaneously exhibit a broad intensity typical of disorder in other directions [58, 59]. Preliminary FFT analysis of Lorentz TEM images [61] of artificial kagome ice indicate the existence of pinch points, as shown in Fig. 5.3a, but the comparatively small field of view of Lorentz TEM create too small a sample set to allow a detailed and quantitative confirmation of this observation. Polarized neutron scattering on the same samples allows for a more statistically relevant study, possibly establishing the significance of these features in a tunable system.

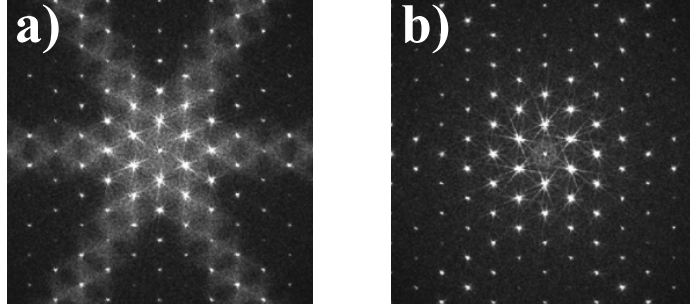


Figure 5.3: **FFT of artificial kagome ice** Fourier transforms of Lorentz images of magnetically disordered (a) and ordered (b) artificial kagome ice. (c) Simulated Fourier transforms of polarized state [61,62].

A main advantage of the neutron scattering experiment is we can look at a larger area of the sample in a single study. Two room-temperature spin configurations are compared with off-specular neutron reflectometry: First, a disordered sample where the magnetic moments of the crystal are randomly oriented, and there is no net moment in the sample. This state is achieved by performing a AC demagnetization of the sample as explained earlier [5,25]. A magnetic force microscopy image of the disordered sample can be seen in Fig. 5.4. Second, a polarized sample where an external magnetic field (using an electromagnet with max. field 0.65T) has been applied to magnetically polarize the sample. In the polarized state, every element has a positive  $M_x$  component. The difference in the scattering from these two spin configurations can show the change in length scale of the magnetic correlations. The ordered sample has sharp peaks representing the large, long-range correlations present. The disordered samples should produce a diffuse scattering pattern, similar to what is seen in a Fourier transform of TEM micrographs for a disordered sample as seen in Fig. 5.3.

When measuring the diffuse scattering as a function of in-plane angle, we expect Bragg peaks, but more interesting are the regions of diffuse scattering in which pinch



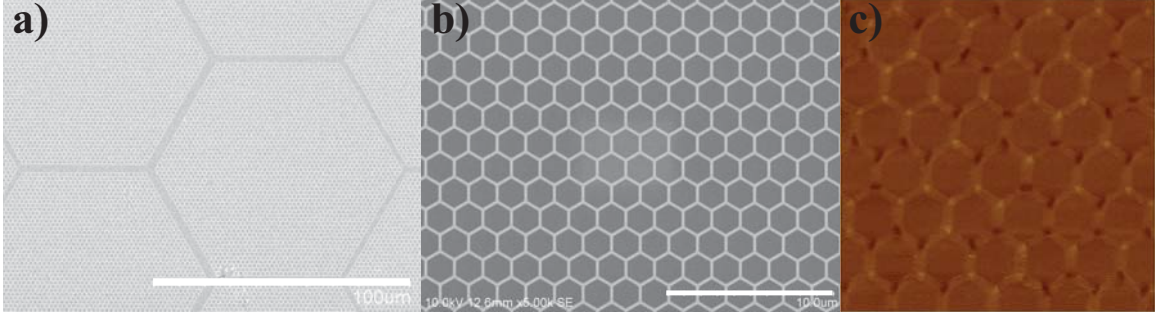


Figure 5.4: **Neutron scattering sample** (a) Low magnification and (b) high magnification images of the large-area neutron sample. Elements are 1 micron in length. They were lengthened to reduce the write time of the 3 mm x 2 mm coverage area. (c) MFM image of the neutron sample to ensure it is disordered.

points may be observed in the vicinity of a Bragg condition, as in the FFT of the TEM measurements. Models of the in-plane scattering components (both structural and magnetic, using parameters for permalloy) are shown below in Fig. 5.3.

As a third field condition for our measurement, we saturate the sample, apply a small negative field and then reduce the field to zero. As demonstrated in artificial spin ice, this field treatment is conducive to the formation of magnetic monopoles of  $\pm 3q$  in samples from other groups [30,31]. This state also has  $M_{net} \approx 0$ , but there is still order in the system. About half of the elements should be reversed in long chains. So, some regions of the crystal will have magnetization  $M_x > 0$  and the other regions will have magnetization  $M_x < 0$ , and they should cancel each other out. We expect this state to give rise to distinctive polarization-dependent features in the diffuse scattering as demonstrated in bulk [38].

We capture data from two different neutron spin states. First, the non-spin flip, is similar to a diffraction pattern one would get on a TEM. It corresponds to neutrons scattering from both the structure of the kagome lattice and the component

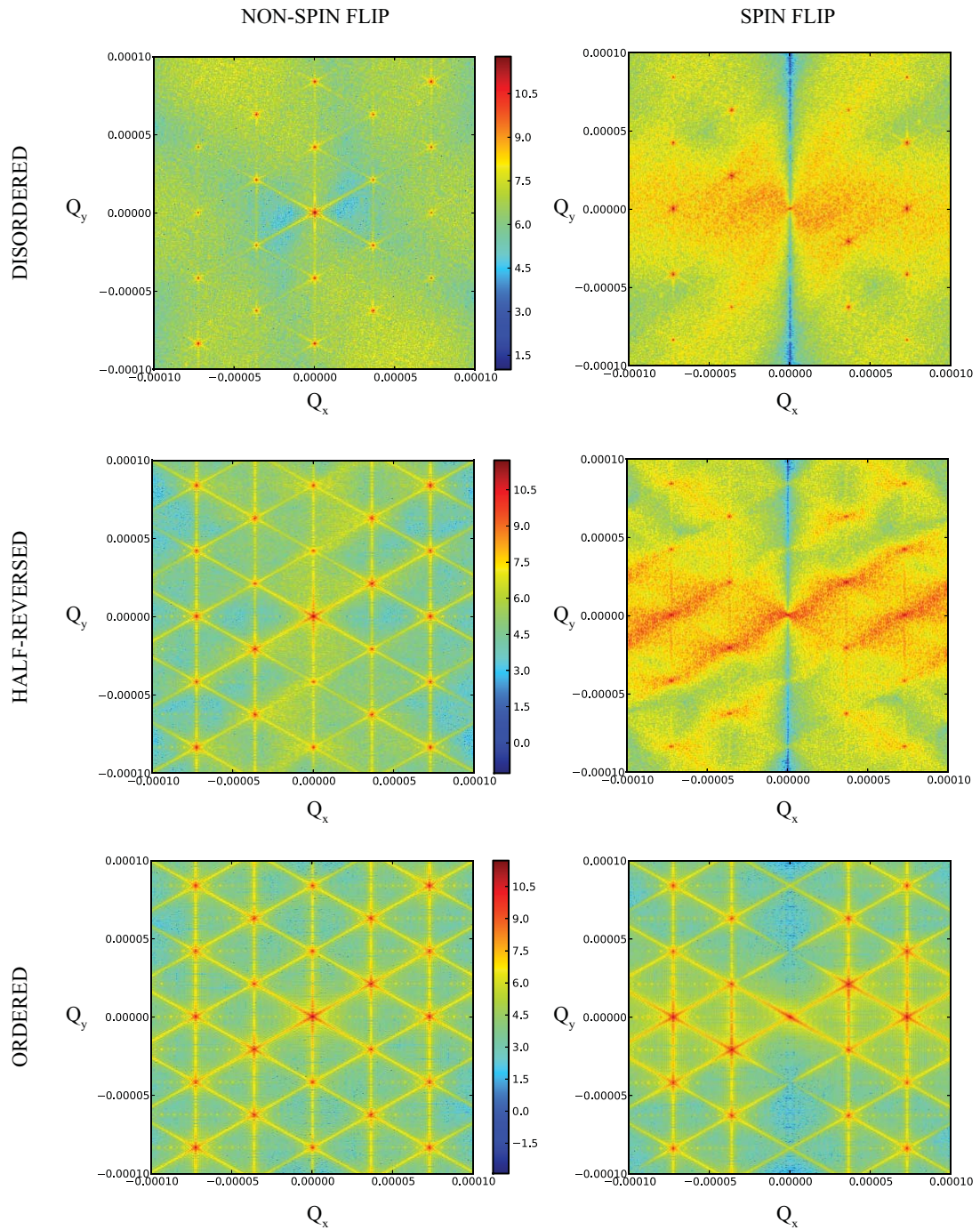


Figure 5.5: **Simulated neutron scattering intensity** These figures are simulated from code developed by Metting *et al.* and give us a chance to match simulations with our experimental data. This is especially useful as the experimental data is such low intensity.

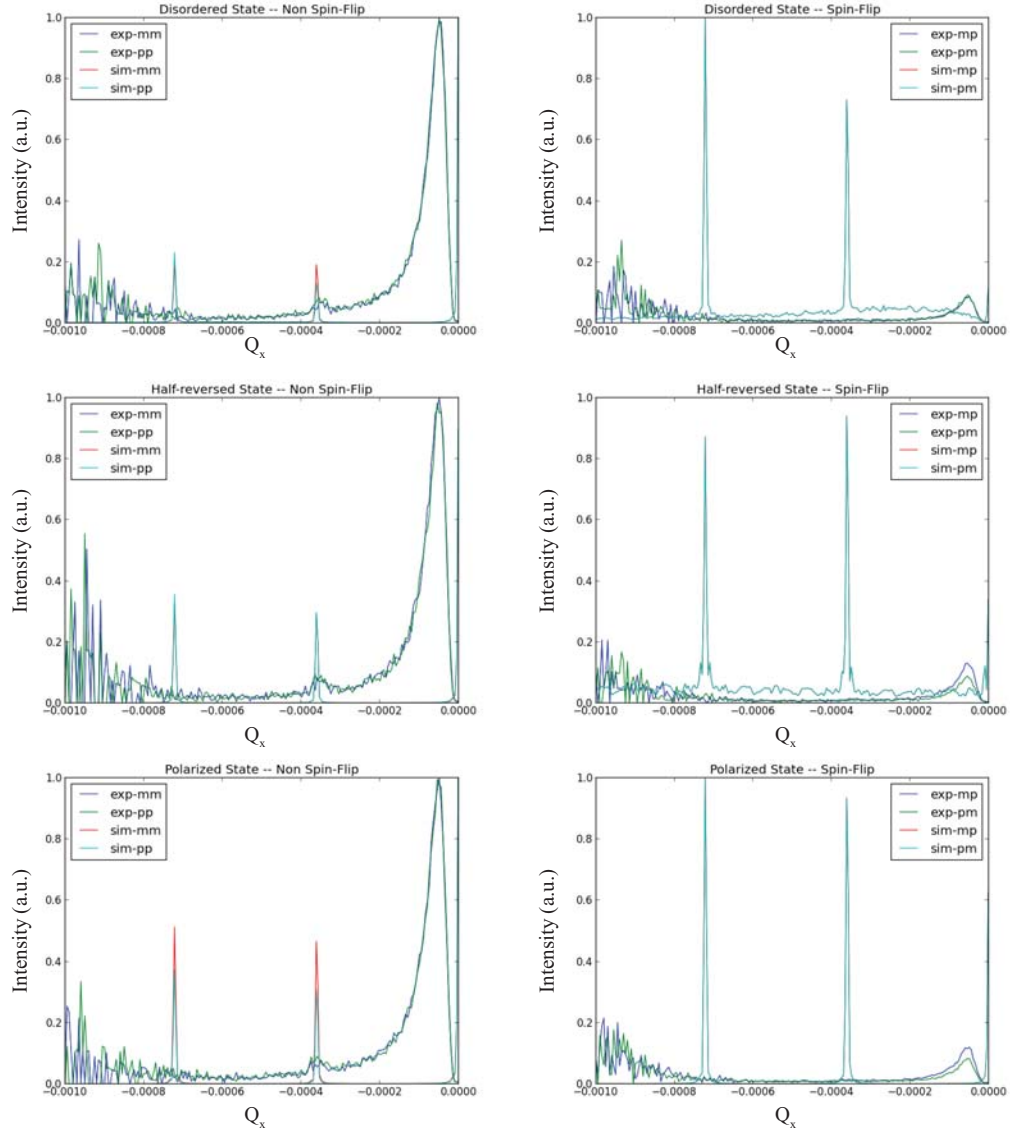


Figure 5.6: **Experimental and theoretical data** The nuclear and magnetic (non-spin flip) data is shown in the left column and the purely magnetic (spin-flip) data is shown in the right. Theoretical plots are also plotted to show that the Bragg peaks of all of our simulations match up nicely. The main issue with the experimental data is that the counts are very low in all cases.

of the in-plane magnetization parallel to the neutron's magnetic spin polarization. The structural scattering is much larger than the magnetic scattering in the non-spin-flip geometry, but we are mainly concerned with the magnetic information of the sample.

Non-spin flip data is only sensitive to magnetization parallel to the neutrons' magnetic spin axis, so for the perpendicular component we must capture spin-flip data. Crucially, the spin-flip signal is purely magnetic; it is not swamped by structural scattering as is the case for non-spin-flip scattering. Neutrons that have had their polarization flipped after interacting with the sample are counted. If there is a perpendicular component to the magnetization, the sample can flip a neutron's polarization and scatter the neutron. Since there is no structural contribution to the spin-flip scattering, the signal is much lower than in the non-spin flip case. Either the counting time needs to increase by several orders of magnitude, or a lot of magnetic material (resulting in a high magnetic scattering signal) needs to be in the beam.

This brings us to the issue with the data from our one experiment: the low number of counts. As can be seen in Fig. 5.6, we have enough counts to see the first-order structural peak in the non-spin flip data at around  $Q_x = -0.0004$ , but the instrumental background obscures other features. These preliminary results are intriguing as it shows that, despite being at the small sample size limit, we are able to see a signal from the sample. It is clear though that we will need to continue experiments to get a higher signal-to-noise ratio. Artificial kagome ice samples are stable over time, so the main issue is getting enough beam time at a user facility. Subsequent experiments at NIST have proven even more fruitful because the position-

sensitive detector more efficiently covers the angular range of interest.

There is a way for us to check our data from Los Alamos though. By looking at simulations and how they match up with our data, we can get an idea of what we expect to see in the three magnetic configurations if our count times were very high. We used the neutron scattering data to check the accuracy of simulations of the scattering intensity of artificial kagome ice crystals. Using software written by Metting *et al.* [63] and subsequently updated by B. Maranville at NIST, we are able to simulate the scattering intensity and compare these to data from  $\text{Ho}_2\text{Ti}_2\text{O}_7$ . To create the simulations, spin maps are needed, and I provided these as images taken from the spin maps from my magnetic reversals, and the disordered spin map was created in MATLAB. When read into the software, the maps provide element locations and magnetization direction, and the interactions between the elements can then be simulated.

The agreement with the experimental data is quite good. When looking at the scattering intensity maps, the results agree with what is expected. The spin-flip images are completely diffuse in the disordered state and completely ordered in the ordered state. In the half-reversed state, the order in the magnetic unit cell is starting to appear out of the diffuse background.

By summing the data along  $Q_y$ , we can create the plots seen in Fig. 5.6, and compare the simulations directly with the experimental data. Here, again, we see good agreement. The theoretically calculated first-order peak lines up with the experimentally determined value, though the features in the calculated diffuse scattering cannot be discerned above background.

This shows that it is possible to successfully model the scattering intensity of artificial kagome ices. In the limit of high counting times, there are very real differences between the different magnetic configurations. For instance, the disordered state shows very diffuse spin-flip scattering intensity, as we expect. Similarly, the ordered state is perfectly ordered. Interestingly, in the half-reversed state, the spin-flip data appears to be somewhere in between the two ordering extremes. Clear Bragg peaks are starting to appear from the diffuse background. The results from this modeling work open the door to continued experiments to look for dipolar interactions in the artificial kagome ice crystals.

## Chapter 6

### Conclusions & Future Work

#### 6.1 Conclusions

The microscopic details of geometric frustration in water ice and the pyrochlore compounds are not easy to measure or control. The interest in studying geometric frustration is growing, and the ongoing search for more geometrically frustrated materials continues. So far, artificial kagome ice allows for the greatest degree of tailoring geometric frustration to the experiment and characterization technique. Artificial spin ice experiments have been studied with magnetic force microscopy [4, 26, 27, 30], photoemission electron microscopy [31], and Lorentz force transmission electron microscopy [5, 6], and different geometries have been used [4, 5, 11]. Artificial spin ice is a system wholly defined by its geometric frustration. Made of a common magnetic elements or alloys (typically  $\text{Ni}_{80}\text{Fe}_{20}$ ), the magnetic characteristics of the samples are fundamentally different than a uniform film of the sample material. The samples remain disordered at room temperature [4, 5] and mimic the residual entropy seen in both water ice and the pyrochlore compounds.

In this dissertation, I have presented my work on the dynamics of artificial kagome ice. By performing high resolution magnetic reversals, I have been able to show that the process can be simply understood as the motion of mobile, magnetic monopoles throughout the system. While working with our collaborators to test the

model, we show that the samples I fabricate have very low disorder of 3.3% making them nearly ideal to test the behavior of geometrically frustrated materials in a system where the frustrated spins can be observed throughout a dynamic process.

By capturing many reversals, we increased the statistical meaning of our observations. Hundreds of reversals were completed in the process of completing the microscope control and analysis scripts allowing us to analyze these data. In Sec. 4.4, I show the avalanches that characterize the  $180^\circ$  reversals. These long, highly branched avalanches can be connected conceptually to a phenomenon known as Barkhausen noise which was an early attempt to understand the reversal process of bulk magnetic samples. When the avalanches are counted and plotted as a function of their size, we see a power law with an exponent of  $\tau = 1.99$  emerge. This connects artificial kagome ice to other systems that exhibit critical behavior such as earthquakes, neurons, mass extinctions, and sand-piles [47, 51, 52]. Further analysis discussed in Sec. 4.4 shows that avalanches in artificial spin ice can be characterized by a fractal dimension. By plotting the size of an avalanche as a function of the bounding area the avalanche takes up, we measure this dimension to be around 1.55.

Interestingly, this behavior can be entirely altered simply by changing the geometry along the edge of the crystal. If single elements are placed along the edges, there are no  $\pm 2q$  charges along the edge of the sample before a reversal starts. The crystal must wait until the field is high enough to reverse a diagonal element to avoid creating ice rule violations all along the edge. An interesting experiment would be to start with an odd edge crystal and gradually remove the single elements along the edge or remove elements from the central region of the crystal. This would create specific



locations where the avalanches will nucleate, and it is possible that their shape and size could be controlled. The ability to control the reversal process that otherwise proceeds via random avalanche reversal would be an interesting development, and it might possibly change the fractal dimension of the avalanches. This type of control over the system is only possible in an intentionally designed system such as artificial kagome ice.

Lastly, I present experiments using off-specular neutron reflectometry, and, at the moment, these data are mainly proof that such experiments on artificial kagome ice are possible. We were right at the low end for sample size required, and the measurements were further complicated by the “openness” of the artificial kagome ice geometry. Only about 20% of the area is actual magnetic material, and the rest is bare substrate. The reliance on electron-beam lithography is the problem here; while it has allowed us to create our crystals, the procedure is quite slow. The FMR sample and the neutron scattering sample both took about 72 hours of continuous writing to complete. Not only is this a slow process, it is also expensive. If different fabrication techniques can be used to create samples with similar geometry and disorder, then the neutron studies can continue to look for dipolar interactions. The dipolar interaction is fundamental in theories of magnetism, and experiments looking at the effect of dipolar interactions would be beneficial to the further development of these theories.

## 6.2 Future Work

This work focuses on using fields to alter the magnetic state of a material and take it through a dynamic process like a magnetic reversal. Thus far, only one study has been conducted looking at thermalized artificial square ices [26]. This study showed that sufficient thermal energy can cause the sample to approach a charge ordered state (similar to that when I polarize my samples) completely on its own by minimizing the energy at the vertices. A similar study in the artificial kagome ices would be interesting to test whether it would also approach a charge ordered state. The complication is the high thermal barrier (Eq. 3.1) preventing elements from switching.

Heating an artificial kagome ice sample would lower this thermal barrier between the two magnetic states available to each element and allow the elements to switch between the states. This would allow a sample to demagnetize itself thermally in a different process from the AC demagnetization I and others have performed on the samples. Seeing this process *in situ* would allow us a detailed view of the thermal demagnetization process, and comparisons to the AC demagnetization process could be made. The work of Morgan *et al.* was performed only on artificial square ice samples. Given the low disorder, and lack of ice rule violations in our samples it would be interesting to perform similar studies on artificial kagome ice samples to see if they will settle in to a charge ordered state as well.

Another aspect of our samples is the complicated reversal process at  $180^\circ$ . We see highly-branched chains of varying sizes. The avalanche events are scale-invariant,

so we can observe them at any length scale, and they are fractal with a fractal dimension  $d_f = 1.55$ . It has been claimed by Bramwell *et al.* that the signature of magnetic monopoles and their motion through a sample can be measured experimentally [40]. One theory that has been developed describes these magnetic monopoles as being connected by one-dimensional reversal events, or Dirac strings. A good test of the theory would be to design a neutron scattering experiment that could measure the dimensionality of the avalanche events. Our samples are also characterized by mobile magnetic monopoles, but we see clear evidence that these reversal events do not need to be one-dimensional.

One possible explanation for our highly branched chains is the low disorder in our samples. Groups making high disorder samples are only able to see one-dimensional reversal events [30, 31]. The low disorder in our samples means that the elements are nearly ideal analogues to the identical, atomic magnetic spin in the pyrochlore spin ices.

The overall idea in this work is that the geometry affects the magnetic interactions within a magnetic material. Nano-patterned magnetic films are becoming more important in the data-storage fields [8] and even logic devices [9]. The frustration in my samples stabilizes the elements' magnetization against spontaneous switching; the magnetic state is stable up to at least the superparamagnetic blocking temperature and maybe even higher. If the frustration in the artificial spin ices could be harnessed for information storage, then small elements will continue to be stable enough to store data magnetically. The highly interacting elements will help overcome the size limit of magnetic bits limiting current hard drive technologies.

## Appendix A

### Computer & Microscope Control Programs

Initially, the very large data sets required to image a crystal throughout an entire reversal process were captured manually. It became clear, however, that moving forward, the data capture process would need to be automated. This requires three computers to seamlessly communicate with each other:

1. TEM control
2. Gatan CCD control
3. LabView field control

Communication over the network was accomplished using the software package JEMToolbox developed by Hiromitsu Furukawa and collaborators at System in Frontier. This software package provides MATLAB functions that simplify the process of sending commands to other computers connected over a local network. The commands themselves are handled using Microsoft's .NET framework, which means that any programming language capable of sending and receiving .NET commands can be used. The programs were initially written using MATLAB, but there were some command timing issues that would crash the program randomly.

The next iteration used LabView. All of the MATLAB scripts that controlled the microscope were re-written in LabView. This fixed the timing issue, and also

makes creating a GUI for users to interact with much easier.

Using LabView, the JEMToolbox, and our custom electronics I was able to write a number of LabView program that will step through a reversal process and capture images throughout the reversal along with a GUI to control the whole process.

Another main benefit of the more stable LabView programs was that I was able to completely automate the process. This reduced the time it took to capture a reversal from 4 hours down to 1.5 depending on the number of images being captured. This automated process is what allows us to capture enough magnetic reversals to have statistically relevant data sets.

1. Degauss the microscope column
2. Polarize the sample along a specified angle, capture and image, and zero the external field
3. Rotate the sample to position for reversal along another specified angle (usually 180 degrees from polarization angle)
4. Step field by  $\Delta H$
5. Zero field
6. Capture image
7. Repeat steps 4-6 until reversal is complete

## A.1 Schematics of LabView Programs

Here I present schematics that show the inputs and resulting outputs for the LabView programs I have written. This should give a rough idea of how the reversal image sequence capture process works. All of these programs will be made available on a digital archive, and they can be provided upon request.

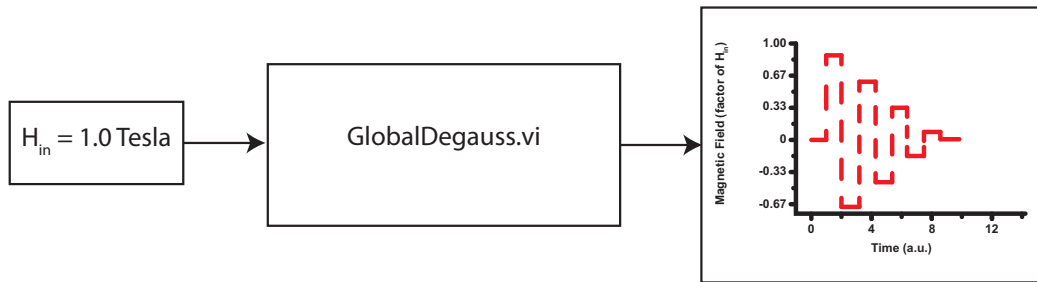


Figure A.1: **Global Degauss** (**GlobalDegauss.vi**) This program reads in the maximum field from **Globals.vi** of 1 Tesla. It then outputs a time varying voltage to the OL that will slowly degauss the TEM column around the sample.



Figure A.2: **Local Degauss** (**LocalDegauss.vi**) This program is similar to **GlobalDegauss.vi** except that instead of the starting field being 1 Tesla, it starts from the maximum field magnitude applied. This gives the ability to get the column back to zero field without altering the magnetic state of the sample.



Figure A.3: **Set Field** (**SetField.vi**) This program sets the field to whatever value is typed into the “Field” text box in the GUI.



Figure A.4: **Angle Interpolation (AngleInterp.vi)** This program wraps the  $\theta$  and  $\phi$  values typed into the GUI such that  $0^\circ \leq \phi \leq 360^\circ$ . It then interpolates the  $\phi$  and  $\theta$  values typed into the GUI from a few data points that were already calculated and determines the corresponding x-tilt and y-tilt and values.



Figure A.5: **Set Goniometer Angles (SetGonioAngles.vi)** This program reads in the calculated x-tilt and y-tilt values and issues a command over the network to the JEOL TEM control computer to set the x-tilt and y-tilt angles to the calculated values. Note: this program requires the network connection to the JEOL computer to be open.



Figure A.6: **Execute Digital Micrograph Script ExecuteGatanScript.vi** This program concatenates a Digital Micrograph script from the image index, filename base, and last field applied values to capture an image from the CCD and save it to an external hard drive. This script is sent over the network to the computer running Digital Micrograph to run immediately. Note: this program requires the network connection to the Digital Micrograph computer to be open.

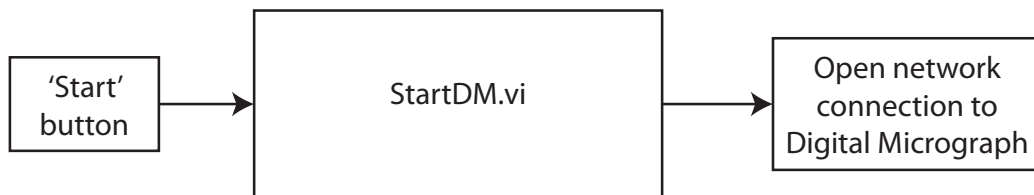


Figure A.7: **Open Digital Micrograph network connection StartDM.vi** This program opens the network connection to the Digital Micrograph computer. The connection stays open until **ExitDM.vi** is run.

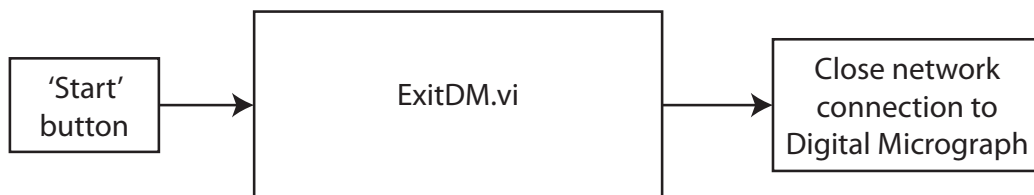


Figure A.8: **Close Digital Micrograph network connection ExitDM.vi** This program closes the network connection to the Digital Micrograph computer.



Figure A.9: **Open JEOL network connection StartJEOL.vi** This program opens the network connection to the JEOL computer. The connection stays open until **ExitJEOL.vi** is run.



Figure A.10: **Close JEOL network connection ExitJEOL.vi** This program closes the network connection to the JEOL computer.



## Appendix B

### Lithography Techniques

#### B.1 Sample Patterning

The first step in the lithography process is spinning the resist onto the SiN membranes. I used a bi-layer of poly-methyl methacrylate (PMMA) of differing molecular weights: 495,000 and 950,000 diluted in chlorobenzene. The differing molecular weights help with removal of the resist later in the patterning process by creating an “undercut”; the cross-section has a trapezoidal shape instead of a rectangular shape as can be seen in Fig. B.3. This helps during the metal lift-off process which will be described later.

In addition to a standard bilayer resist, I also include a thin layer of conductive polymer on the top of the PMMA known as Aquasave by Mitsubishi Rayon. This is a proprietary blend of polymers used to make the resist conducting. This reduces beam deflection from surface charging during the writing process, and increases the symmetry of our patterns.

The patterns are transferred to the SiN membranes via electron-beam lithography (EBL). I use the a Raith e\_Line electron-beam lithography tool for all of the patterning I have done throughout my research. EBL uses a scanning electron microscope and rasters the beam across the membrane, exposing regions of the resist defined by a pattern input into the control computer. The PMMA at the exposed

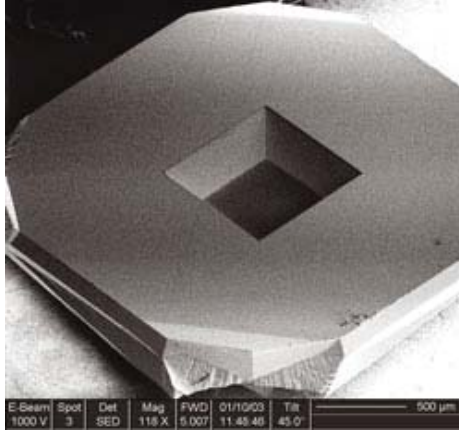


Figure B.1: **Bare silicon nitride TEM window** All samples were patterned onto SiN membranes with a nitride layer of 100nm and a window size of  $500\mu\text{m} \times 500\mu\text{m}$ . From [64].

regions is “cut,” which shortens the PMMA chains (reducing the molecular weight) and makes it more soluble in the developer, and, therefore, easier to remove.

After the resist has been patterned it needs to be developed to remove the areas of the resist that have been exposed to the electron-beam. For this step I place the sample in a sequence of baths:

1. De-ionized water
2. 3:1 Isopropyl alcohol (IPA):Methyl isobutyl ketone (MIBK)
3. Undiluted IPA

The de-ionized water bath removes the top layer of Aquasave, but leaves the resist beneath it unchanged. The MIBK bath removes the exposed regions of the resist, and the IPA halts the development process. The last step is required because, while the exposed regions develop quickly, the entire resist is reactive to the MIBK; too much of the resist can be removed if the MIBK is not washed away quickly.

The result of these patterning steps leaves the bare SiN membrane exposed on the areas that will comprise the artificial kagome crystal. The areas that I do not wish to be patterned are still coated with PMMA and will be removed in subsequent steps.

## B.2 Metal Deposition

Depositing the magnetic thin film is done through a process known as electron-beam evaporation. The sample is placed in a vacuum chamber which is pumped down to  $10^{-5} - 10^{-6}$  Torr. Inside the chamber is a crucible containing the material for the thin film.

By illuminating the material with an electron-beam of sufficient intensity, the material will heat, eventually becoming molten. When enough energy is pumped into the material it heats to the point of developing a substantial vapor pressure and atoms are ejected from the crucible. Material is ejected all over the inside of the vacuum chamber including onto the SiN membrane. To ensure that the material is deposited in a uniaxial direction to ensure good lift-off of the remaining PMMA, the sample needs to be a distance from the crucible determined by the geometry of the evaporation tool. In the case of the Denton E-beam evaporator I used with crucible diameters of 3 cm, the sample is located 50 cm from the crucible.

The most common film I deposited was 23 nm of NiFe with 5 nm of Al to prevent oxidation of the magnetic material all in one deposition session. This thickness provides good Lorentz contrast in the microscope, and ensures the elements are one,

uniform magnetic domain.

Next, metal lift-off is done to remove all of the remaining PMMA. For this, I used PRX-127 (Rohm & Haas), another proprietary chemical made for EBL processes. Acetone is commonly used for metal lift-off, but I required a more aggressive lift-off chemical because I cannot sonicate the SiN membranes without shattering them. Samples are left in PRX-127 for 60 minutes, then sprayed with a stream of PRX-127 to remove the PMMA that had already been successfully released by the PRX-127, and finally placed back into the PRX-127 for another 30 minutes.

The last step is to deposit a uniform film of Al over the entire SiN membrane. This last thin film makes the entire membrane conducting which prevents a surface charge building up from the electron beam in the TEM. This allows me to capture high-quality images with minimal image drift.

Metal lift-off is also the step that largely determines the yield of the lithography process. About 30% of all samples would not be useful because of lift-off failure. The central hexagon, which should be bare SiN membrane after a successful fabrication process, would occasionally not be completely removed and remain on the sample. An image of this can be seen in Fig. B.2. Samples with these errors can not be used in experiments because they wash out the Lorentz contrast, and the leftover resist has magnetic material on top which affects the magnetic configurations of the elements below.

The whole process can be seen in this step-by-step figure starting with spinning the bilayer resist and ending in a patterned film.

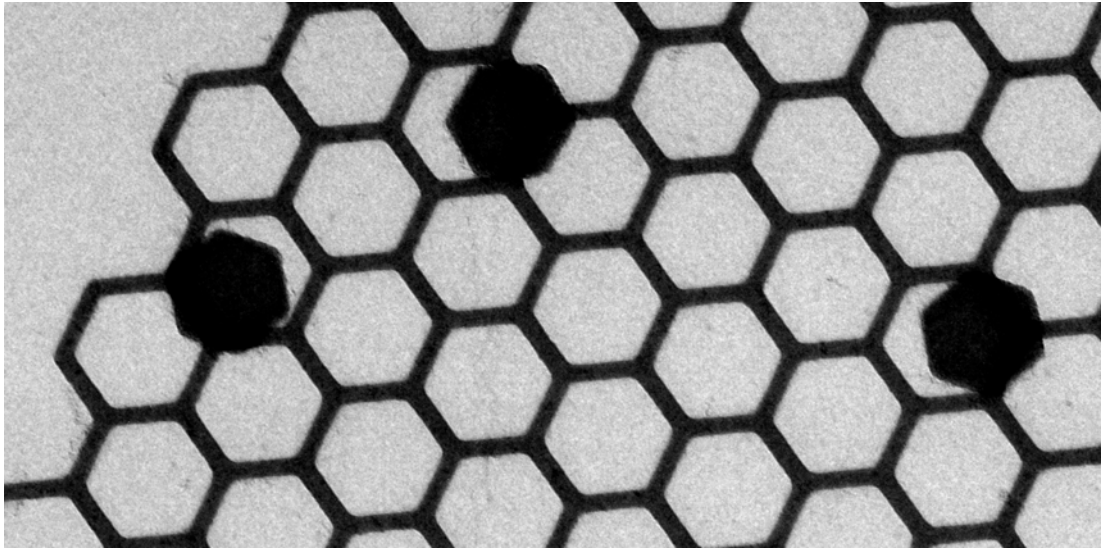


Figure B.2: **Metal lift-off failure** Occasionally, the resist from the central regions of the hexagons would not be removed making certain crystals unusable.

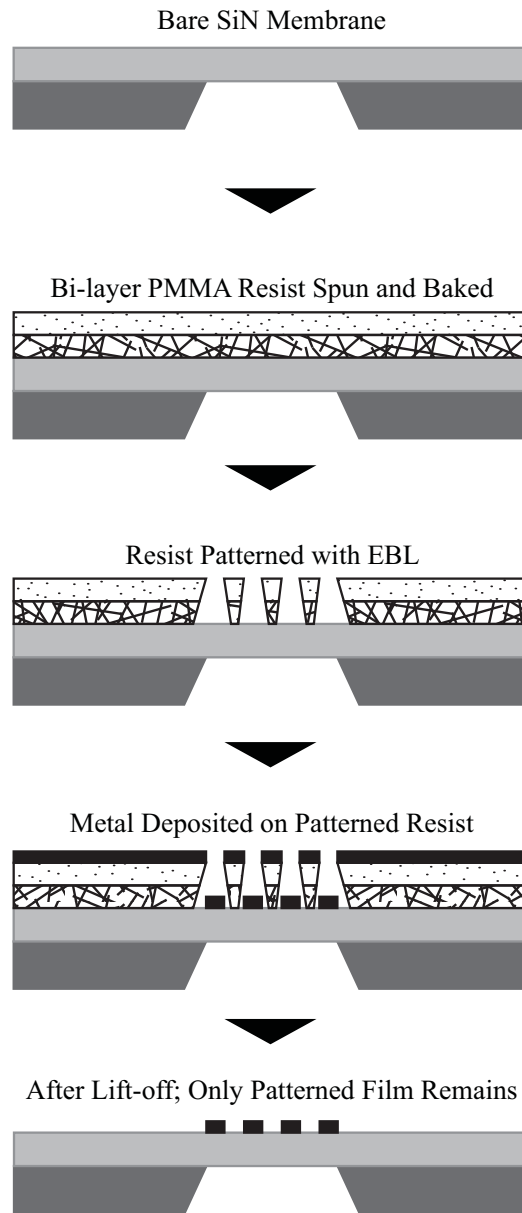


Figure B.3: Sample fabrication process

## Bibliography

- [1] W. F. Giauque and M. F. Ashley, “Molecular rotation in ice at 10k. free energy of formation and entropy of water,” *Phys. Rev.*, vol. 43, pp. 81–82, Jan 1933.
- [2] J. Bernal and R. Fowler, “A theory of water and ionic solution, with particular reference to hydrogen and hydroxyl ions,” *J. Chem. Phys.*, vol. 1, no. 515, 1933.
- [3] L. Pauling, “The structure and entropy of ice and other crystals with some randomness of atomic arrangement,” *J. Am. Chem. Soc.*, vol. 57, no. 2680, 1935.
- [4] R. Wang, C. Nisoli, R. Freitas, J. Li, W. McConville, B. Cooley, M. Lund, N. Samarth, C. Leighton, V. Crespi, and P. Schiffer, “Artificial ‘spin ice’ in a geometrically frustrated lattice of nanoscale ferromagnetic islands,” *Nature*, vol. 439, pp. 303–306, JAN 19 2006.
- [5] Y. Qi, T. Brintlinger, and J. Cumings, “Direct observation of the ice rule in an artificial kagome spin ice,” *Phys. Rev. B*, vol. 77, MAR 2008.
- [6] S. A. Daunheimer, O. Petrova, O. Tchernyshyov, and J. Cumings, “Reducing disorder in artificial kagome ice,” *Phys. Rev. Lett.*, vol. 107, p. 167201, 2011.
- [7] S. T. Bramwell, M. J. Harris, B. C. den Hertog, M. J. P. Gingras, J. S. Gardner, D. F. McMorrow, A. R. Wildes, A. L. Cornelius, J. D. M. Champion, R. G. Melko, and T. Fennell, “Spin correlations in  $\text{Ho}_2\text{Ti}_2\text{O}_7$ : A dipolar spin ice system,” *Phys. Rev. Lett.*, vol. 87, p. 047205, Jul 2001.
- [8] H. J. Richter, A. Y. Dobin, O. Heinonen, K. Z. Gao, R. J. Veerdonk, R. T. Lynch, J. Xue, D. Weller, P. Asselin, M. F. Erden, and R. M. Brockie, “Recording on bit-patterned media at densities of 1 tb/in<sup>2</sup> and beyond,” *IEEE Trans. Magn.*, vol. 42, no. 10, pp. 2255–2260, 2006.
- [9] D. A. Allwood, G. Xiong, C. C. Faulkner, D. Atkinson, D. Petit, and R. P. Cowburn, “Magnetic domain-wall logic,” *Science*, vol. 309, no. 5741, pp. 1688–1692, 2005.
- [10] G. Toulouse, “Theory of frustration effect in spin-glasses .1.,” *Commun. Phys.*, vol. 2, no. 4, pp. 115–119, 1977.
- [11] D. Shi, A. Stein, S. Morley, J. Morgan, P. Olmsted, G. Burnell, and C. Marrows, “An artificial magnetic quasicrystal.” 12th Joint MMM-Intermag Conference, 2013.
- [12] A. Ramirez, A. Hayashi, R. Cava, R. Siddharthan, and B. Shastry, “Zero-point entropy in spin ice,” *Nature*, vol. 6734, no. 399, 1999.
- [13] H. Diep, *Frustrated Spin Systems*. World Scientific Publishing Co. Pte. Ltd., 2004.

- [14] T. Yoshioka, A. Koga, and N. Kawakami, “Frustrated ising model on the garnet lattice,” *eprint arXiv:cond-mat/0402604*, 2008.
- [15] W. F. Giauque and J. W. Stout, “The entropy of water and the third law of thermodynamics. the heat capacity of ice from 15 to 273k.,” *Journal of the American Chemical Society*, vol. 58, no. 7, pp. 1144–1150, 1936.
- [16] J. Nagle, “Lattice statistics of hydrogen bonded crystals. i. the residual entropy of ice,” *J. Math. Phys.*, vol. 7, no. 1484, 1966.
- [17] M. J. Harris, S. T. Bramwell, D. F. McMorrow, T. Zeiske, and K. W. Godfrey, “Geometrical frustration in the ferromagnetic pyrochlore  $\text{Ho}_2\text{Ti}_2\text{O}_7$ ,” *Phys. Rev. Lett.*, vol. 79, pp. 2554–2557, Sep 1997.
- [18] S. T. Bramwell and M. J. Harris, “Frustration in ising-type spin models on the pyrochlore lattice,” *Journal of Physics: Condensed Matter*, vol. 10, no. 14, p. L215, 1998.
- [19] M. Harris, S. Bramwell, T. Zeiske, D. McMorrow, and P. King, “Magnetic structures of highly frustrated pyrochlores,” *J. Magn. Magn. Mater.*, vol. 177, no. 757, 1998.
- [20] C. A. Ross, “Patterned magnetic recording media,” *Annu. Rev. Mater. Res.*, vol. 31, pp. 203–235, 2001.
- [21] T. R. Albrecht, O. Hellwing, R. Ruiz, M. E. Schabes, B. D. Terris, and X. Z. Wu, *Bit-Patterned Magnetic Recording: Nanoscale Magnetic Islands for Data Storage*. Springer US, 2009.
- [22] J. G. Zhu, Y. Zheng, and G. A. Prinz, “Ultrahigh density vertical magnetoresistive random access memory,” *J. App. Phys.*, vol. 87, no. 6668, 2000.
- [23] B. Cullity, *Introduction to Magnetic Materials*. Addison-Wesley Publishing Co., 1972.
- [24] J. Osborn, “Demagnetizing factors of the general ellipsoid,” *Phys. Rev.*, vol. 67, pp. 351–357, 1945.
- [25] R. Wang, J. Li, W. McConville, C. Nisoli, X. Ke, J. Freeland, V. Rose, M. Grimsditch, P. Lammert, V. Crespi, and P. Schiffer, “Demagnetization protocols for frustrated interacting nanomagnet arrays,” *J. Appl. Phys.*, vol. 101, no. 9, p. 09J104, 2007.
- [26] J. P. Morgan, A. Stein, S. Langridge, and C. H. Marrows, “Thermal ground-state ordering and elementary excitations in artificial magnetic square ice,” *Nature Phys.*, vol. 7, no. 75, 2010.



- [27] Z. Budrikis, J. P. Morgan, J. Akerman, A. Stein, P. Politi, S. Langridge, C. H. Marrows, and R. L. Stamps, “Disorder strength and field-driven ground state domain formation in artificial spin ice: Experiment, simulation, and theory,” *Phys. Rev. Lett.*, vol. 109, no. 037203, 2012.
- [28] M. Tanaka, E. Saitoh, H. Miyajima, T. Yamaoka, and Y. Iye, “Magnetic interactions in a ferromagnetic honeycomb nanoscale network,” *Phys. Rev. B*, vol. 73, p. 052411, Feb 2006.
- [29] A. S. Wills, R. Ballou, and C. Lacroix, “Model of localized highly frustrated ferromagnetism: The kagomé spin ice,” *Phys. Rev. B*, vol. 66, p. 144407, Oct 2002.
- [30] S. Ladak, D. E. Read, G. K. Perkins, L. F. Cohen, and W. R. Branford, “Direct observation of magnetic monopole defects in an artificial spin-ice system,” *Nature Phys.*, vol. 6, pp. 359–363, MAY 2010.
- [31] E. Mengotti, L. J. Heyderman, A. F. Rodriguez, F. Nolting, R. V. Hugli, and H.-B. Braun, “Real-space observation of emergent magnetic monopoles and associated dirac strings in artificial kagome spin ice,” *Nature Phys.*, vol. 7, no. 1, pp. 68–74, 2011.
- [32] “Transmission electron microscopy (t.e.m.)” <http://www2.warwick.ac.uk/fac/sci/physics/current/postgraduate/regs/mpags/ex5/techniques/structural/tem/>. Accessed: Dec. 7, 2011.
- [33] K. Baloch, *Thermal Imaging of Mutliwalled Carbon Nanotubes*. PhD thesis, University of Maryland, 2010.
- [34] E. C. Stoner and E. P. Wohlfarth, “A mechanism of magnetic hysteresis in heterogeneous alloys,” *Phil. Trans. Roy. Soc.*, vol. A-240, no. 826, pp. 599–642, 1948.
- [35] G. Bertotti and I. Mayergoyz, *The Science of Hysteresis, Vol I*, vol. 1. Elsevier, Inc., 2006.
- [36] C. Castelnovo, R. Moessner, and S. L. Sondhi, “Magnetic monopoles in spin ice,” *Nature*, vol. 451, pp. 42–45, JAN 3 2008.
- [37] L. D. C. Jaubert and P. C. W. Holdsworth, “Signature of magnetic monopole and dirac string dynamics in spin ice,” *Nature Phys.*, vol. 5, pp. 258–261, APR 2009.
- [38] D. J. P. Morris, D. A. Tennant, S. A. Grigera, B. Klemke, C. Castelnovo, R. Moessner, C. Czternasty, M. Meissner, K. C. Rule, J. U. Hoffmann, K. Kiefer, S. Gerischer, D. Slobinsky, and R. S. Perry, “Dirac strings and magnetic monopoles in the spin ice  $\text{Dy}_2\text{Ti}_2\text{O}_7$ ,” *Science*, vol. 326, pp. 411–414, OCT 16 2009.

- [39] T. Fennell, P. P. Deen, A. R. Wildes, K. Schmalzl, D. Prabhakaran, A. T. Boothroyd, R. J. Aldus, D. F. McMorrow, and S. T. Bramwell, “Magnetic coulomb phase in the spin ice  $\text{Ho}_2\text{Ti}_2\text{O}_7$ ,” *Science*, vol. 326, pp. 415–417, OCT 16 2009.
- [40] S. T. Bramwell, S. R. Giblin, S. Calder, R. Aldus, D. Prabhakaran, and T. Fennell, “Measurement of the charge and current of magnetic monopoles in spin ice,” *Nature*, vol. 461, pp. 956–U211, OCT 15 2009.
- [41] P. Dirac, “Quantised singularities in the electromagnetic field,” *Proc. R. Soc. A*, vol. 133, pp. 60–72, 1931.
- [42] P. Mellado, O. Petrova, Y. Shen, and O. Tchernyshyov, “Dynamics of magnetic charges in artificial spin ice,” *Phys. Rev. Lett.*, vol. 105, p. 187206, Oct 2010.
- [43] O. Shen, O. Petrova, P. Mellado, S. Daunheimer, J. Cumings, and O. Tchernyshyov, “Dynamics of artificial spin ice: a continuous honeycomb network,” *New J. Phys.*, vol. 14, no. 035022, 2012.
- [44] M. J. Donahue and D. G. Porter, “Oommf user’s guide, version 1.0,” Tech. Rep. NISTIR 6376, National Institute of Standards and Technology, Gaithersburg, MD, 1999. <http://math.nist.gov/oommf>.
- [45] O. Perković, K. Dahmen, and J. P. Sethna, “Avalanches, barkhausen noise, and plain old criticality,” *Phys. Rev. Lett.*, vol. 75, pp. 4528–4531, 1995.
- [46] H. J. Williams and W. Shockley, “A simple domain structure in an iron crystal showing a direct correlation with the magnetization,” *Phys. Rev.*, vol. 75, pp. 178–183, Jan 1949.
- [47] P. Bak, C. Tang, and K. Wiesenfeld, “Self-organized criticality: An explanation of the  $1/f$  noise,” *Phys. Rev. Lett.*, vol. 59, pp. 381–384, Jul 1987.
- [48] J. P. Sethna, K. A. Dahmen, and C. R. Myers, “Crackling noise,” *Nature*, vol. 410, pp. 242–250, 2001.
- [49] P. A. Houle and J. P. Sethna, “Acoustic emission from crumpling paper,” *Phys. Rev. E*, vol. 54, pp. 278–283, 1996.
- [50] D. L. Turcotte, “Self-organized criticality,” *Rep. Prog. Phys.*, vol. 62, p. 1377, 1999.
- [51] P. Bak, C. Tang, and K. Wiesenfeld, “Self-organized criticality,” *Phys. Rev. A*, vol. 39, no. 1, pp. 364–374, 1988.
- [52] P. Bak, *How Nature Works*. Springer-Verlag New York, Inc., 1996.
- [53] “Magik off-specular reflectometer.” <http://www.ncnr.nist.gov/instruments/magik/>. Accessed: Mar. 27, 2013.

- [54] J. Snyder, J. Slusky, R. Cava, and P. Schiffer, “How ‘spin ice’ freezes,” *Nature*, vol. 413, no. 6851, pp. 48–51, 2001.
- [55] K. Matsuhira, Z. Hiroi, S. Tayama, and T. Sakakibara, “A new macroscopically degenerate ground state in the spin ice compound  $\text{Dy}_2\text{Ti}_2\text{O}_7$  under a magnetic field,” *J. Phys.: Condens. Matter*, vol. 14, no. L559, 2002.
- [56] T. Sakakibara, T. Tayama, Z. Hiroi, K. Matsuhira, and S. Takagi, “Observation of a liquid-gas-type transition in the pyrochlore spin ice compound  $\text{Dy}_2\text{Ti}_2\text{O}_7$  in a magnetic field,” *Phys. Rev. Lett.*, vol. 90, no. 207205, 2003.
- [57] R. Higashinaka and Y. Maeno, “Field-induced transition on a triangular plane in the spin-ice compound  $\text{Dy}_2\text{Ti}_2\text{O}_7$ ,” *Phys. Rev. Lett.*, vol. 95, no. 237208, 2005.
- [58] M. P. Zinkin, M. J. Harris, and T. Zeiske, “Short-range magnetic order in the frustrated pyrochlore antiferromagnet  $\text{CsNiCrF}_6$ ,” *Phys. Rev. B*, vol. 56, pp. 11786–11790, Nov 1997.
- [59] S. V. Isakov, K. Gregor, R. Moessner, and S. L. Sondhi, “Dipolar spin correlations in classical pyrochlore magnets,” *Phys. Rev. Lett.*, vol. 93, p. 167204, Oct 2004.
- [60] T. Fennell, S. T. Bramwell, D. F. McMorrow, P. Manuel, and A. R. Wildes, “Pinch points and kasteleyn transitions in kagome ice,” *Nature Phys.*, vol. 3, no. 566, 2007.
- [61] Y. Qi, *Artificial Kagome Spin Ice*. PhD thesis, University of Maryland, 2008.
- [62] B. Maranville, S. Daunheimer, J. Cumings, and J. Borchers, “Diffuse scattering from nanostructured artificial spin ice (kagome lattice).” From a proposal for a neutron reflectometry experiment at Los Alamos National Lab.
- [63] C. Metting, *Characterization and Modeling of Off-Specular Neutron Scattering for Analysis of Two Dimensionally Ordered Structures*. PhD thesis, University of Maryland, 2011.
- [64] “Silicon nitride membrane windows for tem.” [http://www.silson.com/sn\\_tem.html](http://www.silson.com/sn_tem.html). Access: April, 24 2013.